Advances in Materials Science and Engineering

Booming for Backfill Materials

Lead Guest Editor: Qiusong Chen
Guest Editors: Ferdi Cihangir, Qi Jia, and Chongchong Qi

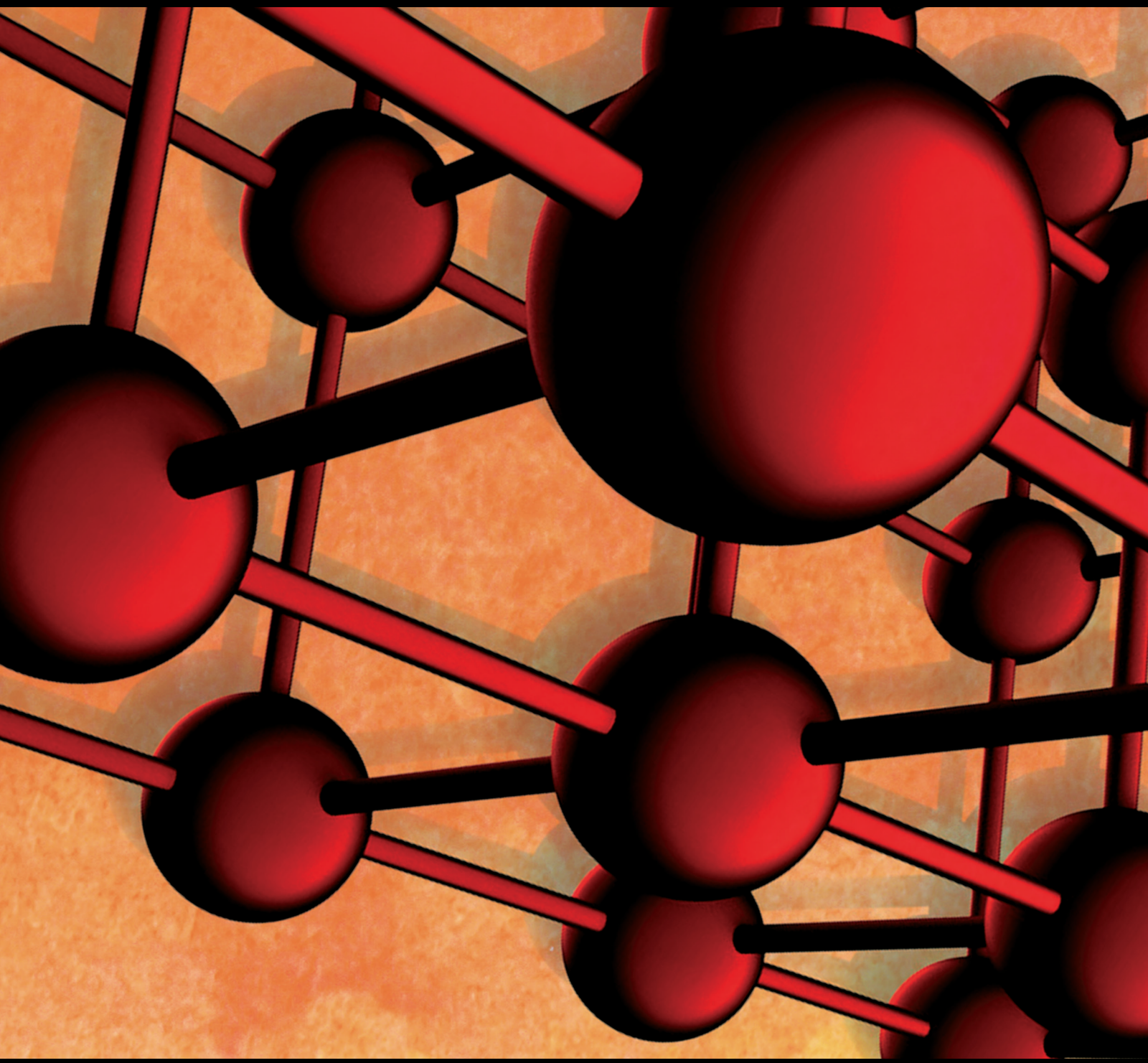

Booming for Backfill Materials

Advances in Materials Science and Engineering

Booming for Backfill Materials

Lead Guest Editor: Qiusong Chen
Guest Editors: Ferdi Cihangir, Qi Jia, and Chongchong Qi

Contents

Hindawi
Advances in Materials Science and Engineering
Volume 2020, Article ID 4536257, 11 pages
https://doi.org/10.1155/2020/4536257

Research Article

Effect of Desliming of Tailings on the Fresh and Hardened Properties of Paste Backfill Made from Alkali-Activated Slag

Ferdi Cihangir and Yunus Akyol

Department of Mining Engineering, Karadeniz Technical University, Trabzon 61080, Turkey

Correspondence should be addressed to Ferdi Cihangir; cihangir@ktu.edu.tr

Received 20 December 2019; Accepted 16 May 2020; Published 8 June 2020

Academic Editor: Marco Cannas

Cemented paste backfill (CPB) allows environmental friendly management of potentially hazardous tailings generated from milling of nonferrous metal sulphide ores by placing such tailings into the underground mined-out openings. The components of CPB are tailings, water, and binders. These components significantly affect the physicomechanical, workability, and geotechnical properties of CPB. Ordinary Portland cement (OPC) is the commonly used binder for CPB operations. The effects of the tailings characteristics and OPC are extensively studied in the study area. The beneficial effect of the use of alkali-activated slags (AASs) on the mechanical and durability properties of CPB of sulphide-rich tailings has been recently reported. Therefore, this study especially focused on the effect of desliming of the tailings on the workability properties of sulphide-rich tailings CPB containing AAS besides hardened properties. In this scope, the water-retention capacities of full (FT) and deslimed tailings (DT) and the workability characteristics of CPB mixtures were studied. DT was found to decrease the water-retention capacity, leading to denser CPB mixtures. In addition, DT-AASs usage produced no adverse effect on the workability of fresh CPB materials. LSS-S (slag activated with liquid sodium silicate) improved the flowability of CPB mixtures owing to its dispersant effect. Desliming also modified the tailing properties by removing fine particles and improved the main geotechnical parameters of CPB.

1. Introduction

Cemented paste backfill (CPB) allows the placement of potentially hazardous materials into the mined-out underground openings. CPB is one of the most effective and environmentally friendly methods for the management of mineral processing tailings. In addition, CPB provides numerous operational, economic, and environmental advantages [1–7]. CPB consists of the entire gradation processing tailings (full tailings, FT), binders, and water in general. Each component significantly affects the quality and performance of CPB from the mixing stage to the end of service life underground [8–15].

CPB requires more than 15 wt.% fine particles (<20 μm) for water retention in its matrix to prevent segregation [16, 17] and to provide favorable consistency. Higher fines content is reported to increase the viscosity of CPB mixtures and the resistance against flow in a pipeline for a given water content [18]. Full tailings (FT) with high fines content retain more water and increase the porosity in the CPB matrix. CPB is produced from FT which may consist of high amount of sulphide minerals depending on the ore composition. In such a case, a high porosity (i.e., 30–50%) promotes air and/or water diffusion, leading to the formation of acid and sulphate through the oxidation of sulphide minerals (pyrite, in particular) in CPB [19]. In this case, CPB becomes susceptible to both internal and external acid and sulphate attacks [19–21]. Acid leads to the destruction/decalcification of hydration products such as C–S–H (crystalline calcium (CaO) silicate (SiO_2) hydrate (H_2O)) formed with the hydration of the binder, such as ordinary Portland cement (OPC), while sulphate precipitates in the form of gypsum and/or ettringite as a result of chemical reactions with portlandite (C–H: $Ca(OH)_2$: a hydration product) [22–24]. These reaction products (secondary gypsum, ettringite, and so on) cause durability problems [25, 26]. Mineral and

chemical additives [27–31], alkali-activated slags (AASs) [32, 33], and the use of deslimed tailings (DT) have been suggested to improve the strength and stability of CPB in the short and long term [8, 19, 21, 34].

CPB contains a large amount of water to provide the required consistency for material transportability [35]. The excess water can easily drain when DT is used. Therefore, the rate of strength gain of CPB when DT is used is reported to be faster than that of FT, since the former allows a denser cementitious matrix and microstructure (i.e., decrease in the void ratio, porosity, etc.) [19, 21]. DT is also reported to reduce binder consumption for the desired strength level [19] which is among the most important features of CPB applications.

The effect of desliming on the strength and durability performance of CPB has been extensively investigated [8, 9, 19, 21, 22, 34, 36–38]. However, Ercikdi et al. [19] noted that desliming might affect unit operations such as transportation of CPB into underground voids. Therefore, in addition to mechanical and geotechnical properties, workability of CPB is of great importance when using DT. On the other hand, AAS has been reported to cause some workability losses on fresh concrete/mortar samples [39, 40] although this problem can be overcome by pozzolanic ultrafine mineral additions [41] or retarders [42–44].

Workability is frequently used to characterize some properties such as flowability, pumpability, and consistency of the materials containing hydraulic binders (e.g., fresh concrete) for mixing, transportation, and placement without allowing for any segregation. There are many factors that can influence workability such as type and shape of aggregate, solid content, binder type and dosage, water-to-cement ratio, activator type, concentration, and modulus ratio [45]. Slump test, compaction test, and flow test are usually used for the assessment of workability [46]. Slump test which is a simple, easy to perform and evaluate, cheap, and widely known method is extensively used by mine operators on-site to estimate material consistency as a good indication of flowability in terms of transportability of fresh CPB mixtures [18, 47–50]. Any change in the initial consistency of CPB material during transportation may require high pump pressures and can cause excessive friction and thus wear problems in pipes which result in high costs [51]. Therefore, workability is of great significance in practice for CPB applications [13, 52–55].

Although the use of AAS is reported in some underground mining applications in South Africa and Canada [56], there is lack of knowledge about the conditions of usage and performance (i.e., durability and workability) properties of the materials containing AAS. On the other hand, while FT is extensively used for backfilling of the mined-out underground voids, use of DT was reported in South African mines in order to prepare high quality CPB material [57]. However, there are relatively few studies dealing with the performance properties of CPB made from AAS [14, 58] and DT.

In [22], the authors studied the mechanical, durability, hydraulic, and microstructural properties of deslimed sulphide-rich tailings CPB in detail. They indicated that DT and AAS enhanced the strength gain, improved the microstructure, and decreased the effects of acid and sulphate attacks. However, they did not study the workability of fresh CPB mixtures and main geotechnical properties of fresh and hardened CPB materials made from of DT and AASs which are the focus of the current study. Since the workability of CPB materials is determined by the interaction between the solid (tailings, cement, slag) and liquid components (water, activators), the water-retention capacity of the tailings was firstly determined in this study. Afterwards, effect of desliming on the geotechnical properties of fresh CPB mixtures prepared from FT and DT using OPC and AASs combinations was studied. Some geotechnical parameters, i.e., water content and porosity levels of hardened CPBs over the curing period, were also studied.

2. Experimental Studies

2.1. Tailings and Binders. Full (FT) and deslimed tailings (DT) were utilized to investigate the coupled effect of using DT and alkali-activated slag (AAS) on the workability and some main geotechnical properties of CPB materials. FT was collected from the disc filter outlet of the paste backfill circuit while DT (coarse sized) was obtained simultaneously from the underflow after separation and removal of fine particles by hydrocyclone.

Ordinary Portland cement (OPC) and alkali-activated blast furnace slag (AAS) were used in order to investigate the effect of desliming on the workability of the fresh CPB mixtures and main hardened properties of CPB specimens. Liquid sodium silicate (LSS) and sodium hydroxide (SH) were used as activators. For the characterization of the materials used in the study, chemical (ACME laboratories in Canada using X-ray fluorescence and wet chemical analyses), mineralogical (TCMA (Turkish Cement Manufacturers' Association) labs in Turkey using X-ray diffractometer analysis), and physical properties of the binders were determined (Tables 1–2). Detailed characterization of the materials can be found elsewhere [22].

2.2. Water-Retention Tests on Tailings Materials. CPB is required to contain sufficient amount of water to achieve the desired consistency for its transportability from the paste plant to the underground openings. Tailings must have at least 15 wt.% material finer than 20 μm to retain enough water to form paste with the desired flow properties for its transportation through a borehole or pipeline [16]. In order to study the water-retention characteristics, each tailing and some amount of water were firstly mixed and prepared in duplicate (without binder addition) at slump consistencies of 8.0 ± 0.1 inch which were verified using the slump test in accordance with ASTM C143/C143M-12 [59]. After that, the procedure described by Ercikdi et al. [19] was followed to determine the water-retention capacities of the tailings where mean values of duplicate tests were presented in the results.

2.3. Mixing Procedure and Workability Tests of Fresh CPB Materials. In this study, FT and DT, binders, and tap water were prepared in six different recipes using a Univex

Table 1: Physical, chemical, and mineralogical properties of tailings.

Chemical composition	Full tailings (wt.%)	Deslimed tailings (wt.%)	Physical properties	Full tailings	Deslimed tailings
SiO_2	13.16	10.43	Specific gravity (G_s)	4.09	4.32
Al_2O_3	4.81	2.46	Specific surface area (cm^2/g)	3662	1956
Fe_2O_3	48.41	53.93	D_{10} (μm)	2.14	14.98
MgO	1.13	0.91	D_{30} (μm)	7.65	29.62
CaO	1.83	1.28	D_{50} (μm)	19.21	45.24
Na_2O	0.19	0.18	D_{60} (μm)	28.52	54.23
K_2O	0.64	0.23	D_{90} (μm)	77.43	117.39
TiO_2	0.08	0.07	Coefficient of curvature (C_c)	0.96	1.08
P_2O_5	0.02	0.02	Coefficient of uniformity (C_u)	13.33	3.62
MnO	0.06	0.05			
Cr_2O_3	0.01	<0.01			
$BaSO_4$	2.54	2.02			
Loss on ignition	26.9	28.2			
Sulphide (S^{-2})	37.4	42.23			
Total S	38.52	42.76			
Pyrite content (FeS_2)	70.13	79.19			

Table 2: Chemical, physical, and mineralogical properties of binders.

Chemical composition	OPC (wt.%)	Slag (wt.%)	Physical properties	OPC	Slag
SiO_2	21.88	39.75	Specific gravity	3.07	2.89
Al_2O_3	4.74	10.91	Specific surface area (cm^2/g)	4120	4600
Fe_2O_3	2.90	0.80	Retained on 45 μm sieve (%)	2.17	4.15
CaO	65.0	38.02	Retained on 32 μm sieve (%)	7.48	9.60
MgO	1.40	5.92	Mineralogical composition (%)		
TiO_2	0.19	0.51	C_3S	50.42	–
Cr_2O_3	0.01	0.01	C_2S	27.76	–
Na_2O	0.39	0.32	C_3A	7.66	–
K_2O	0.75	1.19	C_4AF	8.83	–
MnO	0.12	1.54	Basicity index		
P_2O_5	0.06	<0.01		–	1.03
Free lime	1.04	–			
Loss on ignition	2.5	0.20			
SO_3	2.67	1.62			
Reactive SiO_2	–	39.10			

SRMF20 Stand model blender. CPB mixtures were prepared at 7 wt.% binder dosage on total dry solids basis. For AAS samples, the solid contents of the activators, i.e., SiO_2 and Na_2O, were considered for determination of binder content. Na_2O concentration of the activators was fixed at 8 wt.% by weight of the slag. The modulus ratio (SiO_2/Na_2O) of LSS was set to 1.0 with SH where optimal mechanical results were reached for CPB of sulphide-rich tailings [22]. Since the ideal slump of CPB material is between ~6.5 and 10.0 inches in most CPB applications [60, 61], the initial consistency of CPB mixtures was set to 8.0 ± 0.1 inches for this study. Based on the design and consistency conditions, the workability and the geotechnical properties of fresh CPB mixtures were obtained.

Workability tests were performed during 2 hours according to ASTM C143/C143M-12 [59]. These tests allowed the assessment of the flowability behavior of fresh CPB materials prepared with OPC, LSS-S, and SH-S. Duplicate simple slump tests with a standard cone were performed on the fresh mixtures at the predetermined time intervals (0, 30, 60, 90, 120 min). During the slump tests, the remaining CPB material in the bucket was mixed thoroughly to prevent the settling of the tailings particles and the stiffening of the mixture. The mean slump values at the corresponding time intervals were used in the presentation of the results.

2.4. Determination of Main Geotechnical Parameters of Hardened CPBs. For the assessment of the effect of desliming and AAS interaction on the geotechnical properties (i.e., total porosity and gravimetric water (wt.%) content) of hardened CPB specimens (CPBs), 72 samples were prepared in duplicate for each recipe at 14, 28, 56, 112, 224, and 360 days of curing. Thereafter, CPB specimens were sealed in plastic bags and subjected to curing in the curing room at $20 \pm 1^{\circ}C$ and $85 \pm 1\%$ humidity. For the determination of the final gravimetric water content, some CPB specimens were collected and oven-dried for 36 h at $50^{\circ}C$. The mercury intrusion porosimetry (MIP) tests were carried out on the representative samples of fractured CPB specimens at 14, 56, and 360 days in order to evaluate the effect of desliming on the total porosities of CPBs. MIP tests were performed according to ASTM D4404-10 [62] under pressure ranging from 0 to 414 MPa.

3. Results and Discussion

3.1. Effect of Desliming on the Physical and Chemical Characteristics of the Tailings. FT and DT were seen to include the required amount of fine particles (greater than 15 wt.%) for CPB mixtures in order to provide the desired consistency according to the fineness contents (−20 μm) (51 wt.% for FT and 16 wt.% for DT). Due to the removal of fine particles and clay minerals by desliming, SiO_2+Al_2O_3 content and the specific surface area (cm^2/g) of the tailings were observed to decrease by 28.27% and 46.59%, respectively. Additionally, as an indication of the concentrated coarser particles and denser minerals, i.e., pyrite, during desliming process, the amount of sulphidic minerals was seen to increase, thereby increasing the specific gravity (G_s) of the tailings (Table 1).

Pyrite was observed to be the predominant mineral in FT and DT based on the mineralogical compositions of the tailings from XRD analysis where quartz, albite, barite, dolomite, calcite, ferroactinolite, kaolinite, and illite were also detected in the tailings (Figure 1). Among these components, kaolinite and illite are nonswelling clay minerals. Kaolinite is composed of model sheet units of silica tetrahedra and alumina octahedra, called a 1 : 1 layer mineral, while illite is a 2 : 1 layer mineral consisting of two silica tetrahedra units enclosing one octahedral alumina unit. Al–OH linkages located at the surface of such clays are reported to play an important role in the water adsorption process [63].

3.2. Effect of Desliming on the Water-Retention Characteristics of the Tailings and the Properties of Fresh CPB Mixtures. Water-retention characteristics of a cemented paste backfill material (CPB) are unique due to the colloidal properties of the fine particles where colloidal electric charge forms bonds with water molecules. Therefore, water-retention properties significantly affect the rheology/workability of CPB [64]. Figure 2 illustrates that desliming reduces the water-retention capacity of the tailings. Water-retention capacity of DT was 11.66 times less than FT. This substantial reduction in water retention was concomitant with the removal of fine alumina-silicate minerals (i.e., kaolinite and illite) by desliming as indicated by the lower $SiO_2 + Al_2O_3$ content of DT (Table 1). Water absorption capacity of a mixture of kaolinite and illite (Figure 1) is reported to be in the range of 70 to 100% by weight of dry clay [65]. Illite is also reported to take up more water than kaolinite owing to its structure in 2 : 1 sheet of units made up of silica and alumina [63, 66].

Water-retention capacity is significantly affected by the particle size distribution and mineral composition in terms of fine particles and clay minerals as mentioned above, respectively. Therefore, the greater water-retention capacity of FT was ascribed to the higher amount of finer particles having also higher specific surface area. This means that more water is required to wet the surface of the fine particles for a desired consistency [21, 66]. Desliming was determined to reduce the specific surface area of the tailings with a resultant decrease in water-retention capacity. Water-retention tests also indicated higher drainage of excess water from the coarse tailings, as expected. In [67], it was reported that a faster rate of removal of excess water from a stope through adjacent walls or barricade improved the stability of the backfilled material. It can be concluded that the reduced amount of finer particles by desliming leads to higher settling capacity which improves the properties of paste backfill material. In this way, it also decreases the potential pore water pressures on barricades in practice [68].

Owing to the lower water-retention capacity and the higher sulphide mineral content after desliming, DT was seen to increase the solid contents of CPB mixtures by 5–7 wt.% and hence the pulp density (g/cm^3). This suggests that DT enables the transfer of higher amount of sulphide minerals into the underground voids. Furthermore, desliming of the total tailings was also observed to lower the water content by 22.98 wt.%, 17.69 wt.%, and 19.55 wt.% and reduce the water-to-cement ratios by 28.28%, 21.76%, and 24.19% for OPC, LSS-S, and SH-S samples, respectively (Figure 3). The details of the data for Figure 3 can be found elsewhere [22].

The above parameters affected by the characteristics of the tailings directly influence the rheology/workability of CPB [69]. Additionally, these findings simply show that the percentage of water retention/adsorption by finer tailings particles is a function of particle size distribution and specific surface area. In other words, these results suggest a considerable potential for refinement on geotechnical properties (i.e., denser CPB material with lower porosity), and more compact structure corresponding to a decreased porosity by approximately 15–20% [70]. On the other hand, higher water-retention capacity was reported to give greater total porosity and higher void ratio [8, 19, 21].

3.3. Effect of Desliming on the Workability Properties of CPB. The change in slump levels during two-hour period of fresh paste backfill mixtures of FT and DT is shown in Figure 4. Slump levels of fresh CPB mixtures were observed to increase compared to the initial levels owing to the generation of hydration gel products for all binders as a result of the advance of hydration. DT mixtures resulted in a bit lower slump levels than those of FT mixtures, which can be attributed to the reduction in interparticle distance [58]. In other words, particle interaction increases as the solids concentration increases, which makes DT mixtures more viscous due to the granuloviscous effects. On the other hand, higher slump levels for FT mixtures can be ascribed to the higher fines contents as a consequence of the increase of hydrodynamic and electroviscous effects. The authors of [71] reported that the design parameters had an influential effect on the rheology of CPB. In [69], the authors found that flowability decreases as the hydration progresses, which is not beneficial for transportation of CPB materials. In [72], it was reported that higher solids content resulted in lower CPB material consistency concordant with the findings of this study. In [73], it was found that increasing the content of finer tailings decreased the flowability (transportability) at a given water-to-cement ratio, while Clark et al. [18] noted that fresh CPB mixtures of FT are easier to transport at a given slump.

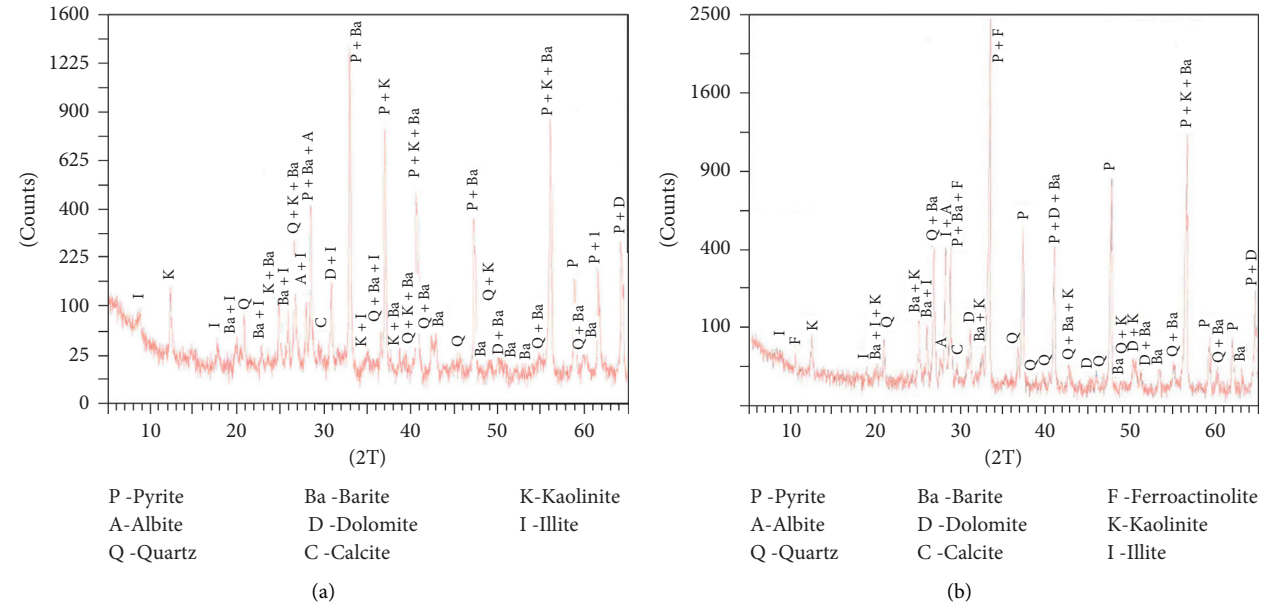

Figure 1: Mineralogical compositions of FT (a) and DT (b).

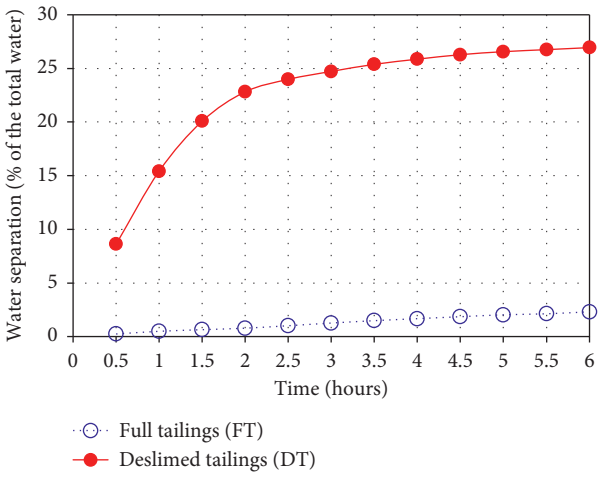

Figure 2: Water-retention characteristics of the tailings.

Slight reduction in workability (about 2%) was observed for OPC/DT and SH-S/DT mixtures after the first hour, where the workability levels were still higher than the initial values. This can be ascribed to the different hydration kinetics and mechanism, and properties of C–S–H products of AAS and OPC. SH-S is a depolymerization process from one to seven days and a polymerization process from 7 to 28 days, while LSS-S hydration can be regarded as a polymerization process. In addition, at a constant Na_2O content, SH-activated slag was reported to yield the shortest induction period and the highest accelerated hydration peak since pH of SH solution is higher than other Na-containing compounds. Besides, heat evolution curve during the hydration of SH-S was observed to be similar to that of OPC [46].

LSS was observed to have a fluidizing effect leading to the highest slump levels and it produced the highest workability for both tailings types (Figures 4 and 5). This can be attributed to the dispersion capability of silicate anions since it prevents the mineral pulp from agglomeration and settling out [74]. Jiang et al. [58] found and reported that the addition of alkali activator (sodium silicate + sodium hydroxide) reduces the Zeta potential of slag particles with the tailings yielding higher workability. Therefore, better workability levels for CPB of AAS in this study can be ascribed to the interaction between the AAS binders and the tailings on the basis of the difference in the surface chemistry of the solid materials of CPB. Earlier studies [75, 76] also reported a beneficial effect of LSS for reducing the viscosity of clay slurries by the adsorption of silicate anions on the positive edges of clays, which generates repulsion between particles. Slightly greater workability levels of FT mixtures compared to those of DT can be attributed to the higher amount of fine particles (i.e., clay minerals: kaolinite and illite) in addition to having lower solids content at a given slump.

It is evident from these findings that AASs (i.e., LSS-S and SH-S) not only enhance the geotechnical properties of fresh CPB mixtures but also improve the workability characteristics of the materials especially in the case of LSS. Therefore, the transportation and placement of CPB mixtures of AASs are likely to be easier than those of OPC considering the transportation time which varies between 6 and 15 minutes from paste backfill plant to underground voids to be filled for most of the CPB applications [77]. Besides, DT-AAS combination was seen to produce no adverse effect on the workability of fresh CPB materials taking into account the initial values. However, it should be noted here that CPB materials can have different yield stress in terms of flowability characteristics for a given slump value. Besides, a small change in pulp density/solids concentration can cause a significant change in yield stress for a

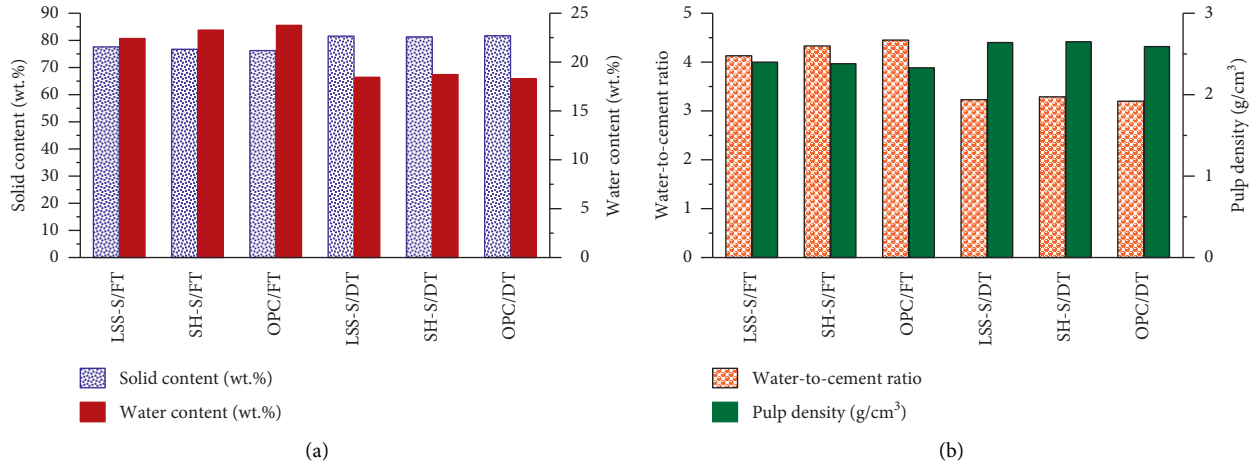

Figure 3: Effect of desliming of the tailings on the properties of fresh CPB mixtures.

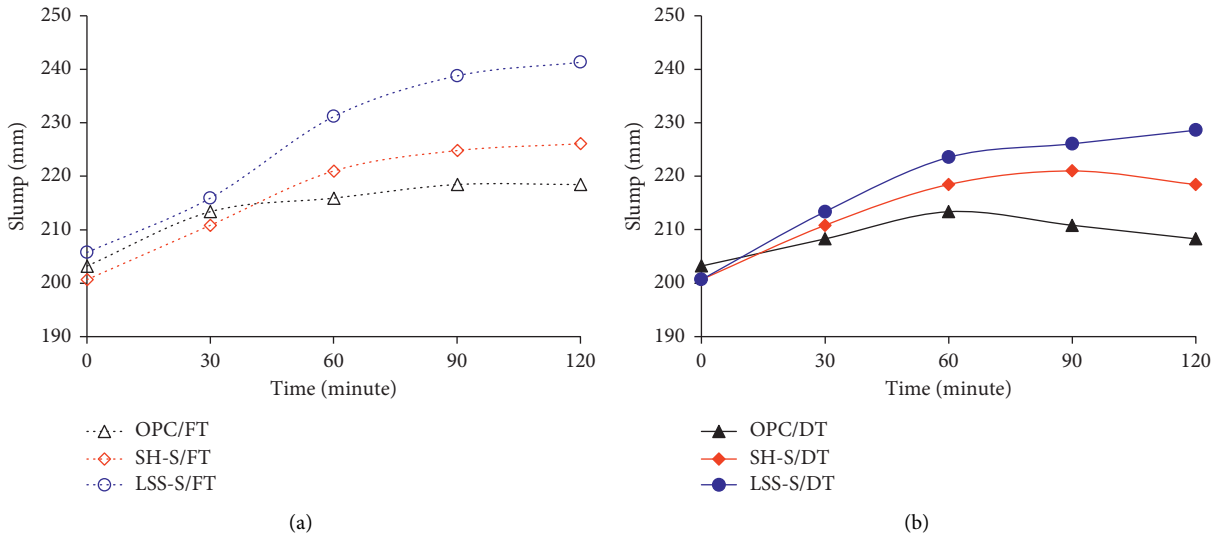

Figure 4: Workability characteristics of CPB mixtures for FT and DT.

Figure 5: Slump levels of LSS-S/DT mixtures: (a) initial (7.9 inches) and (b) after 2 hours (9 inches).

given mine tailing. Therefore, flow response of CPB mixtures should be tested in terms of flow rate, flow resistance, pipeline blockage, unwanted settling of coarse tailings particles, pressure loss, power consumption, etc. using a suitable surface loop test set.

In this study, contradictory results in terms of workability properties were obtained from CPB mixtures of AASs compared to those of fresh concrete/mortar mixtures [39, 40]. In these studies, significant workability losses were observed within the first hour. This behavior can be explained by (i) higher water-to-cement ratio of CPB (≈3.0–6.5-fold) compared to those of concrete/mortar mixtures (≈0.4–0.6-fold in general), (ii) greater water-retention capacity of the tailings particles (as aggregate) during and after the hydration process, and (iii) AASs which display different hardening characteristics in such mixture medium (i.e., CPB mixture) [46, 77]. Therefore, the workability characteristics of CPB materials were seen to be different from those of concrete/mortar systems as in hardening process which was discussed in detail by Benzaazoua et al. [8].

3.4. Effect of Desliming on the Hardened Properties of CPB. Figure 6 presents the water content (wt.%) for hardened CPBs over the curing period. Water content decreases for all CPBs with curing time due to the hydration products and the formation of secondary expansive minerals (i.e., gypsum ($CaSO_4{\cdot}2H_2O$) and ettringite ($3CaO{\cdot}Al_2O_3{\cdot}3CaSO_4{\cdot}32H_2O$ in OPC samples)) [22]. Since FT had more amounts of finer tailings, thereby higher specific surface area, the water content of FT resulted in higher values over the curing period. However, DT displayed lower water contents since tailings composed of coarser particles have lower specific surface area requiring less water to wet the entire surface of tailings particles. This can also be ascribed to the decrease in the amount of fine silicate minerals ($SiO_2 + Al_2O_3$) due to desliming. As a consequence, DT samples had resultant lower water contents by 22.71–27.63%, %18.74–24.25%, and 19.57–25.98% for OPC, LSS-S, and SH-S, respectively, as the curing time elapsed. OPC samples were seen to keep more water during the curing which can be attributed to the inherent properties of tailings and the interaction between the tailings and the binders as was seen in fresh CPB mixtures.

Figure 7 shows the porosity levels of FT and DT samples. Higher water-retention capacity of fine tailings led to higher total porosities. Therefore, lower porosities in DT were assumed to stem from the lower water-retention capacity of the coarse tailings as well as higher solid contents [4] compared to FT. The decrease in porosities after 14 days can be attributed to the continuous hydration products of the binders and the formation of secondary mineral phases. Details of the technical parameters of 56 day porosities in Figure 7 can be found elsewhere [22].

DT was observed to reduce the porosity by 19.4, 16.9%, and 15.3% in average for OPC, LSS-S, and SH-S samples, respectively, depending on the curing time. This can be ascribed to the higher self-consolidation characteristics of

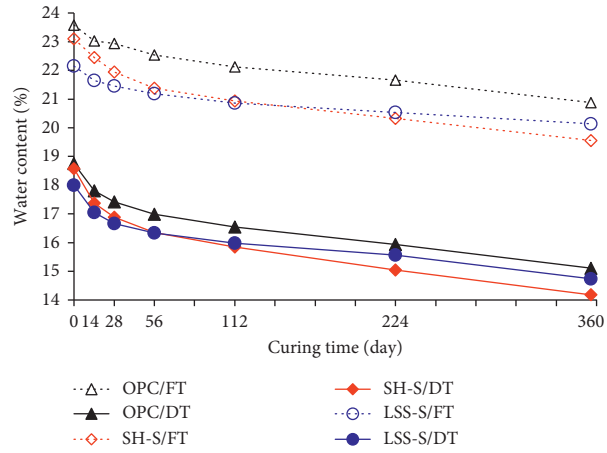

Figure 6: Effect of AAS and DT on the water content levels of CPBs over curing time.

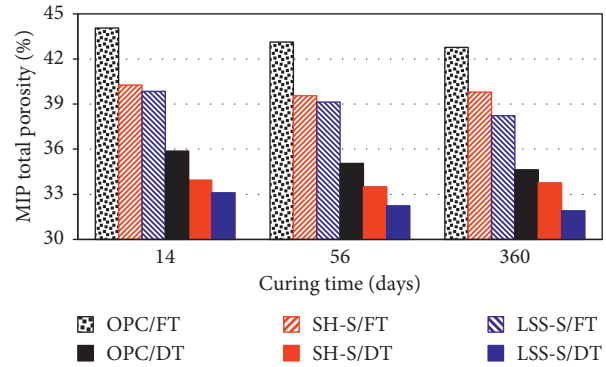

Figure 7: Effect of AAS and DT on the total porosity levels of CPBs.

DT leading to drainage of excess water [19, 78]. As observed in Figures 6 and 7, reduced water content and porosity suggest the refinement of microstructure [79, 80] in case of DT, which is in good agreement with Ercikdi et al. [19].

Additionally, Guo et al. [81] used sodium silicate as additive to Portland cement for CPB preparation and found that the cement containing sodium silicate significantly decreased the porosity and refined the pore structure of CPB. Similarly, as can be seen from Figure 7, LSS-S provided the lowest porosities for both tailings. Therefore, these results can be related to the better bonding and dense packing capacity of sodium silicate promoting more condensed binding gel structure leading to refinement of porosity [82].

The porosity of materials was reported to decrease while higher solid content was obtained in the case of lower water-to-cement ratios [78, 83]. In [84], the authors also reported that the lower the water-to-cement ratio, the higher the amount of cement bonds resulting in higher strength gain of CPB. These are well consistent with the findings of [22]. They observed that DT and AASs had profound effects on the mechanical, hydraulic, and microstructural properties, enabling a good durability and the refined geotechnical characteristics of hardened CPB for the corresponding

materials used in the current paper too. Use of DT and AAS combinations provided ~4–10-fold strengths compared to the CPBs made from FT-OPC. DT-AAS was also found to decrease the acid and sulphate effects owing to the high degree of cementation and dense microstructure with reduced permeability. More details can be found elsewhere [22].

One can infer from these results that since the porosity and the water retention of materials are responsible for the generation of acid and sulphate in the case of sulphide-rich tailings, desliming significantly contributes to the strength gain and the durability performance of CPBs [22]. These findings may be attributed to the faster rate of water drainage in case of deslimed tailings and the faster settling of the coarser particles. Both scenarios favor the cementation degree and a dense packing matrix alleviating the oxidation of pyrite grains in CPB materials [3, 8, 19, 21, 70, 85]. Given the considerations above, not only does DT provide significant practical advantages in some aspects such as reducing water content (Figure 3) but it may also decrease the pore water pressure on barricades during mining activities, therefore reducing the potential risks of liquefaction due to the blasting activities [67, 68, 86].

4. Conclusions

This study has demonstrated the influence of desliming and AAS as binder on the workability and geotechnical properties of CPBs. Owing to the removal of fine particles/clay minerals, desliming decreased the specific surface area and increased the specific gravity of the tailings. On the one hand, desliming led to a significant reduction in water-retention capacity of the tailings. On the other hand, it allowed improvement of the geotechnical properties of hardened CPB, which is a result of dense CPB mixture with higher solids content, lower water-to-cement ratio, and higher settling ability of fresh CPB. Therefore, DT displayed lower water contents and porosities with increase in the curing time by 18–26% and 15–20% in average, respectively. The refinement of such geotechnical properties is of great importance in respect of increasing the mechanical performance of CPB in practice.

Workability characteristics of CPB mixtures containing AAS binders appear to be different from those of concrete/mortar systems. The increase in solid content due to desliming was observed to result in little lower consistency. However, DT and AAS produced no adverse effect on the workability of fresh CPB materials. In fact, LSS-S appears to improve the workability properties of CPB presumably due to its dispersant effect on fine particles. However, flow response of CPB mixtures in case of any important change in solids concentration should be tested by a suitable surface loop test set.

Data Availability

The data supporting the findings of this study are included in the article. Additionally, raw data generated during the study are available from the corresponding author on request.

Conflicts of Interest

The authors declare that they have no conflicts of interest.

Acknowledgments

The authors would like to express their sincere thanks to the Research Foundation of Karadeniz Technical University (Project no. ARGEBD–8629) and to Ercument KOC, Cayeli Bakir Isletmeleri A.S., Karcimsa A.S., Trabzon Cement A.S., and finally, Ege Chemicals Ltd. for material support.

References

[1] M. Fall and M. Benzaazoua, "Modeling the effect of sulphate on strength development of paste backfill and binder mixture optimization," *Cement and Concrete Research*, vol. 35, no. 2, pp. 301–314, 2005.

[2] W. Sui, D. Zhang, Z. C. Cui, Z. Wu, and Q. Zhao, "Environmental implications of mitigating overburden failure and subsidences using paste-like backfill mining: a case study," *International Journal of Mining, Reclamation and Environment*, vol. 29, no. 6, pp. 521–543, 2015.

[3] A. Tariq and E. K. Yanful, "A review of binders used in cemented paste tailings for underground and surface disposal practices," *Journal of Environmental Management*, vol. 131, pp. 138–149, 2013.

[4] X. Chen, X. Shi, J. Zhou, X. Du, Q. Chen, and X. Qiu, "Effect of overflow tailings properties on cemented paste backfill," *Journal of Environmental Management*, vol. 235, pp. 133–144, 2019.

[5] C. Qi, L. Liu, J. He, Q. Chen, L. J. Yu, and P. Liu, "Understanding cement hydration of cemented paste backfill: DFT study of water adsorption on tricalcium silicate (111) surface," *Minerals*, vol. 9, pp. 10–12, 2019.

[6] Y.-y. Tan, X. Yu, D. Elmo et al., "Experimental study on dynamic mechanical property of cemented tailings backfill under SHPB impact loading," *International Journal of Minerals, Metallurgy, and Materials*, vol. 26, no. 4, pp. 404–416, 2019.

[7] J. Zheng, X. Sun, L. Guo, S. Zhang, and J. Chen, "Strength and hydration products of cemented paste backfill from sulphide-rich tailings using reactive MgO-activated slag as a binder," *Construction and Building Materials*, vol. 203, pp. 111–119, 2019.

[8] M. Benzaazoua, M. Fall, and T. Belem, "A contribution to understanding the hardening process of cemented pastefill," *Minerals Engineering*, vol. 17, no. 2, pp. 141–152, 2004.

[9] M. Benzaazoua, T. Belem, and B. Bussière, "Chemical factors that influence the performance of mine sulphidic paste backfill," *Cement and Concrete Research*, vol. 32, no. 7, pp. 1133–1144, 2002.

[10] J. C. H. Célestin and M. Fall, "Thermal conductivity of cemented paste backfill material and factors affecting it," *International Journal of Mining, Reclamation and Environment*, vol. 23, no. 4, pp. 274–290, 2009.

[11] E. Yilmaz, T. Belem, M. Benzaazoua, A. Kesimal, B. Ercikdi, and F. Cihangir, "Use of high-density paste backfill for safe disposal of copper/zinc mine tailings," *Gospodarka Surowcami Mineralnymi - Mineral Resources Management*, vol. 27, pp. 81–94, 2011.

[12] A. Wu, Y. Wang, H. Wang, S. Yin, and X. Miao, "Coupled effects of cement type and water quality on the properties of

cemented paste backfill," *International Journal of Mineral Processing*, vol. 143, pp. 65–71, 2015.

[13] H. Jiang, M. Fall, and L. Cui, "Yield stress of cemented paste backfill in sub-zero environments: experimental results," *Minerals Engineering*, vol. 92, pp. 141–150, 2016.

[14] S. Cao, E. Yilmaz, W. Song, and G. Xue, "Assessment of acoustic emission and triaxial mechanical properties of rock-cemented tailings matrix composites," *Advances in Materials Science and Engineering*, vol. 2019, pp. 1–12, 2019.

[15] C. Min, X. Li, S. He et al., "Effect of mixing time on the properties of phosphogypsum-based cemented backfill," *Construction and Building Materials*, vol. 210, pp. 564–573, 2019.

[16] F. W. Brackebusch, "Basics of paste backfill systems," *Mining Engineering*, vol. 46, pp. 1175–1178, 1994.

[17] D. Simon and M. Grabinsky, "Apparent yield stress measurement in cemented paste backfill," *International Journal of Mining, Reclamation and Environment*, vol. 27, no. 4, pp. 231–256, 2013.

[18] C. C. Clark, J. D. Vickery, and R. R. Backer, *Transport of Total Tailings Paste Backfill : Results of Full-Scale Pipe Test Loop*, Bibliogov, Long Island, NJ, USA, 1995.

[19] B. Ercikdi, H. Baki, and M. İzki, "Effect of desliming of sulphide-rich mill tailings on the long-term strength of cemented paste backfill," *Journal of Environmental Management*, vol. 115, pp. 5–13, 2013.

[20] M. Benzaazoua, P. Marion, I. Picquet, and B. Bussière, "The use of pastefill as a solidification and stabilization process for the control of acid mine drainage," *Minerals Engineering*, vol. 17, no. 2, pp. 233–243, 2004b.

[21] M. Fall, M. Benzaazoua, and S. Ouellet, "Experimental characterization of the influence of tailings fineness and density on the quality of cemented paste backfill," *Minerals Engineering*, vol. 18, no. 1, pp. 41–44, 2005.

[22] F. Cihangir and Y. Akyol, "Mechanical, hydrological and microstructural assessment of the durability of cemented paste backfill containing alkali-activated slag," *International Journal of Mining, Reclamation and Environment*, vol. 32, no. 2, pp. 123–143, 2018.

[23] M. Pokharel and M. Fall, "Combined influence of sulphate and temperature on the saturated hydraulic conductivity of hardened cemented paste backfill," *Cement and Concrete Composites*, vol. 38, pp. 21–28, 2013.

[24] J. Zheng, L. Guo, X. Sun, W. Li, and Q. Jia, "Study on the strength development of cemented backfill body from lead-zinc mine tailings with sulphide," *Advances in Materials Science and Engineering*, vol. 2018, Article ID 7278014, 8 pages, 2018.

[25] F. Cihangir, B. Ercikdi, A. Kesimal, S. Ocak, and Y. Akyol, "Effect of sodium-silicate activated slag at different silicate modulus on the strength and microstructural properties of full and coarse sulphidic tailings paste backfill," *Construction and Building Materials*, vol. 185, pp. 555–566, 2018.

[26] B. Ercikdi, F. Cihangir, A. Kesimal, H. Deveci, and İ. Alp, "Utilization of industrial waste products as pozzolanic material in cemented paste backfill of high sulphide mill tailings," *Journal of Hazardous Materials*, vol. 168, no. 2-3, pp. 848–856, 2009.

[27] B. Ercikdi, A. Kesimal, F. Cihangir, H. Deveci, and İ. Alp, "Cemented paste backfill of sulphide-rich tailings: importance of binder type and dosage," *Cement and Concrete Composites*, vol. 31, no. 4, pp. 268–274, 2009.

[28] B. Ercikdi, F. Cihangir, A. Kesimal, H. Deveci, and İ. Alp, "Effect of natural pozzolans as mineral admixture on the performance of cemented-paste backfill of sulphide-rich tailings," *Waste Management & Research*, vol. 28, no. 5, pp. 430–435, 2010.

[29] B. Ercikdi, F. Cihangir, A. Kesimal, H. Deveci, and İ. Alp, "Utilization of water-reducing admixtures in cemented paste backfill of sulphide-rich mill tailings," *Journal of Hazardous Materials*, vol. 179, no. 1–3, pp. 940–946, 2010b.

[30] O. Peyronnard and M. Benzaazoua, "Estimation of the cementitious properties of various industrial by-products for applications requiring low mechanical strength," *Resources, Conservation and Recycling*, vol. 56, no. 1, pp. 22–33, 2011.

[31] A. Tariq and M. Nehdi, "Developing durable paste backfill from sulphidic tailings," *Proceedings of the Institution of Civil Engineers - Waste and Resource Management*, vol. 160, no. 4, pp. 155–166, 2007.

[32] F. Cihangir, B. Ercikdi, A. Kesimal, H. Deveci, and F. Erdemir, "Paste backfill of high-sulphide mill tailings using alkali-activated blast furnace slag: effect of activator nature, concentration and slag properties," *Minerals Engineering*, vol. 83, pp. 117–127, 2015a.

[33] F. Cihangir, B. Ercikdi, A. Kesimal, A. Turan, and H. Deveci, "Utilisation of alkali-activated blast furnace slag in paste backfill of high-sulphide mill tailings: effect of binder type and dosage," *Minerals Engineering*, vol. 30, pp. 33–43, 2012.

[34] A. Kesimal, B. Ercikdi, and E. Yilmaz, "The effect of desliming by sedimentation on paste backfill performance," *Minerals Engineering*, vol. 16, no. 10, pp. 1009–1011, 2003.

[35] B. Koohestani, A. Koubaa, T. Belem, B. Bussière, and H. Bouzahzah, "Experimental investigation of mechanical and microstructural properties of cemented paste backfill containing maple-wood filler," *Construction and Building Materials*, vol. 121, pp. 222–228, 2016.

[36] B. Ercikdi, T. Yılmaz, and G. Külekci, "Strength and ultrasonic properties of cemented paste backfill," *Ultrasonics*, vol. 54, no. 1, pp. 195–204, 2014.

[37] A. Kesimal, H. Deveci, B. Ercikdi, and F. Cihangir, *Evaluation of Paste Backfill Performance of Different Mill Tailings in Kure Copper Mine*, Karadeniz Technical University, Trabzon, Turkey, 2012.

[38] A. Kesimal, F. Cihangir, B. Ercikdi, H. Deveci, and I. Alp, *Optimization of Paste Backfill Performance for Different Ore Types in Cayeli Copper Mine*, Karadeniz Technical University, Trabzon, Turkey, 2010.

[39] F. G. Collins and J. G. Sanjayan, "Workability and mechanical properties of alkali activated slag concrete," *Cement and Concrete Research*, vol. 29, no. 3, pp. 455–458, 1999a.

[40] C. Duran Atis, C. Bilim, O. Celik, and O. Karahan, "Influence of activator on the strength and drying shrinkage of alkali-activated slag mortar," *Construction and Building Materials*, vol. 23, pp. 548–555, 2009.

[41] F. Collins and J. G. Sanjayan, "Effects of ultra-fine materials on workability and strength of concrete containing alkali-activated slag as the binder," *Cement and Concrete Research*, vol. 29, no. 3, pp. 459–462, 1999b.

[42] A. R. Brough, M. Holloway, J. Sykes, and A. Atkinson, "Sodium silicate-based alkali-activated slag mortars," *Cement and Concrete Research*, vol. 30, no. 9, pp. 1375–1379, 2000.

[43] F. Collins and J. G. Sanjayan, "Early age strength and workability of slag pastes activated by NaOH and Na2CO3," *Cement and Concrete Research*, vol. 28, no. 5, pp. 655–664, 1998.

[44] F. A. Memon, M. F. Nuruddin, and N. Shafiq, "Effect of silica fume on the fresh and hardened properties of fly ash-based self-compacting geopolymer concrete," *International Journal*

of Minerals, Metallurgy, and Materials, vol. 20, no. 2, pp. 205–213, 2013.

[45] S. Cao, E. Yilmaz, and W. Song, "Evaluation of viscosity, strength and microstructural properties of cemented tailings backfill," *Minerals*, vol. 8, no. 8, pp. 352–419, 2018.

[46] C. Shi, P. V. Krivenko, and D. Roy, *Alkali-activated Cements and Concretes*, Taylor & Francis, London, UK, 2006.

[47] S. Clayton, T. G. Grice, and D. V. Boger, "Analysis of the slump test for on-site yield stress measurement of mineral suspensions," *International Journal of Mineral Processing*, vol. 70, no. 1–4, pp. 3–21, 2003.

[48] S. J. Mahlaba and P. C. Pretorius, "Exploring paste technology as a co-disposal option for fly ash and brines," in *Paste 2006*, R. J. Jewell, S. Lawson, and P. Newman, Eds., pp. 181–189, Australian Centre for Geomechanics, Perth, Australia, 2006.

[49] A. Saebimoghaddam, "Rheological yield stress measurement of mine paste fill material," Master thesis, p. 113, McGill University, Montreal, Canada, 2005.

[50] Q. Chen, Q. Zhang, X. Wang, C. Xiao, and Q. Hu, "A hydraulic gradient model of paste-like crude tailings backfill slurry transported by a pipeline system," *Environmental Earth Sciences*, vol. 75, pp. 1–9, 2016.

[51] D. Hewitt, S. Allard, and P. Radziszewski, "Pipe lining abrasion testing for paste backfill operations," *Minerals Engineering*, vol. 22, no. 12, pp. 1088–1090, 2009.

[52] X. J. Deng, B. Klein, J. X. Zhang, D. Hallbom, and B. de Wit, "Time-dependent rheological behaviour of cemented backfill mixture," *International Journal of Mining, Reclamation and Environment*, vol. 32, no. 3, pp. 145–162, 2016, In press.

[53] B. Ercikdi, F. Cihangir, A. Kesimal, and H. Deveci, "Practical importance of tailings for cemented paste backfill," in *Paste Tailings Management*, E. Yilmaz and M. Fall, Eds., pp. 7–32, Springer, Berlin, Germany, 2017.

[54] B. Koohestani, T. Belem, A. Koubaa, and B. Bussière, "Experimental investigation into the compressive strength development of cemented paste backfill containing Nano-silica," *Cement and Concrete Composites*, vol. 72, pp. 180–189, 2016.

[55] L. Lang, K.-I. Song, D. Lao, and T.-H. Kwon, "Rheological properties of cemented tailing backfill and the construction of a prediction model," *Materials*, vol. 8, no. 5, pp. 2076–2092, 2015.

[56] H. M. Khater, "Studying the effect of thermal and acid exposure on alkali-activated slag geopolymer," *Advances in Cement Research*, vol. 26, no. 1, pp. 1–9, 2014.

[57] J. J. Cilliers and A. L. Hinde, "An improved hydrocyclone model for backfill preparation," *Minerals Engineering*, vol. 4, no. 7–11, pp. 683–693, 1991.

[58] H. Jiang, Z. Qi, E. Yilmaz, J. Han, J. Qiu, and C. Dong, "Effectiveness of alkali-activated slag as alternative binder on workability and early age compressive strength of cemented paste backfills," *Construction and Building Materials*, vol. 218, pp. 689–700, 2019.

[59] ASTM C143/C143M-12, *Standard Test Method for Slump of Hydraulic-Cement Concrete*, ASTM International, West Conshohocken, PA, USA, 2012.

[60] D. A. Landriault, R. Verburg, W. Cincilla, and D. Welch, *Paste Technology for Underground Backfill and Surface Tailings Disposal Applications*, p. 121p, Short Course Notes-Technical Workshop, Vancouver, BC, Canada, 1997.

[61] E. Yilmaz, T. Belem, B. Bussière, M. Mbonimpa, and M. Benzaazoua, "Curing time effect on consolidation behaviour of cemented paste backfill containing different cement types and contents," *Construction and Building Materials*, vol. 75, pp. 99–111, 2015.

[62] ASTM D4404-10, *Standard Test Method for Determination of Pore Volume and Pore Volume Distribution of Soil and Rock by Mercury Intrusion Porosimetry*, ASTM International, West Conshohocken, PA, USA, 2014.

[63] J. L. Bantignies, C. C. D. Moulin, and H. Dexpert, "Wettability contrasts in kaolinite and illite clays: characterization by infrared and x-ray absorption spectroscopies," *Journal de Physique IV*, vol. 7, pp. 867–869, 1997.

[64] S. I. Sveinson, "Characterization of tailings for paste backfill system design," MSc thesis, p. 223, University of British Columbia, Vancouver, BC, Canada, 1999.

[65] W. A. White and E. Pichler, "Water-sorption characteristics of clay minerals," p. 20, Illinois State Geological Survey Circular, IL, USA, 1959.

[66] J. D. Schuttlefield, D. Cox, and V. H. Grassian, "An investigation of water uptake on clays minerals using ATR-FTIR spectroscopy coupled with quartz crystal microbalance measurements," *Journal of Geophysical Research: Atmospheres*, vol. 112, pp. 1–14, 2007.

[67] N. Sivakugan, R. M. Rankine, K. J. Rankine, and K. S. Rankine, "Geotechnical considerations in mine backfilling in Australia," *Journal of Cleaner Production*, vol. 14, no. 12-13, pp. 1168–1175, 2006.

[68] M. Yumlu and M. Guresci, "Paste backfill bulkhead monitoring: a case study from Inmet's Cayeli Mine, Turkey," in *Proceedings of the 9th International Symposium in Mining with Backfill*, pp. 146–155, Montreal, Quebec, Canada, April–May 2007.

[69] D. Wu, S.-j. Cai, and G. Huang, "Coupled effect of cement hydration and temperature on rheological properties of fresh cemented tailings backfill slurry," *Transactions of Nonferrous Metals Society of China*, vol. 24, no. 9, pp. 2954–2963, 2014.

[70] F. Cihangir, A. Kesimal, H. Deveci, B. Ercikdi, and Y. Akyol, *Investigation of the Microstructural and Performance Properties of Paste Backfill Containing Alkali-Activated Slag*, Karadeniz Technical University, Trabzon, Turkey, 2015b.

[71] D. Wu, M. Fall, and S. J. Cai, "Coupling temperature, cement hydration and rheological behaviour of fresh cemented paste backfill," *Minerals Engineering*, vol. 42, pp. 76–87, 2013.

[72] S. Yin, A. Wu, K. Hu, Y. Wang, and Y. Zhang, "The effect of solid components on the rheological and mechanical properties of cemented paste backfill," *Minerals Engineering*, vol. 35, pp. 61–66, 2012.

[73] X. Ke, H. Hou, M. Zhou, Y. Wang, and X. Zhou, "Effect of particle gradation on properties of fresh and hardened cemented paste backfill," *Construction and Building Materials*, vol. 96, pp. 378–382, 2015.

[74] A. Kashani, J. L. Provis, G. G. Qiao, and J. S. J. Van Deventer, "The interrelationship between surface chemistry and rheology in alkali activated slag paste," *Construction and Building Materials*, vol. 65, pp. 583–591, 2014.

[75] A. J. Ayadi, J. Soro, A. Kamoun, and S. Baklouti, "Study of clay's mineralogy effect on rheological behavior of ceramic suspensions using an experimental design," *International Journal of Research and Review in Applied Sciences*, vol. 14, pp. 374–384, 2013.

[76] B. Ersoy, A. Evcin, T. Uygunoglu, Z. B. Akdemir, W. Brostow, and J. Wahrmund, "Zeta potential-viscosity relationship in kaolinite slurry in the presence of dispersants," *Arabian Journal for Science and Engineering*, vol. 39, no. 7, pp. 5451–5457, 2014.

[77] F. Cihangir, *Investigation of utilization of alkali-activated blast furnace slag as binder in paste backfill*, PhD thesis, Karadeniz Technical University, p. 187, Trabzon, Turkey, 2011.

[78] T. Yilmaz, B. Ercikdi, K. Karaman, and G. Kulekci, "Assessment of strength properties of cemented paste backfill by ultrasonic pulse velocity test," *Ultrasonics*, vol. 54, no. 5, pp. 1386–1394, 2014.

[79] A. Ghirian and M. Fall, "Coupled thermo-hydro-mechanical-chemical behaviour of cemented paste backfill in column experiments," *Engineering Geology*, vol. 170, pp. 11–23, 2014.

[80] T. Yilmaz and B. Ercikdi, "Predicting the uniaxial compressive strength of cemented paste backfill from ultrasonic pulse velocity test," *Nondestructive Testing and Evaluation*, vol. 31, pp. 247–266, 2016.

[81] L. Guo, W. Li, X. Yang, and W. Xu, "Sodium silicate gel effect on cemented tailing backfill that contains lead-zinc smelting slag at early ages," *Advances in Materials Science and Engineering*, vol. 2018, Article ID 8502057, 6 pages, 2018.

[82] F. Pacheco-Torgal, J. A. Labrincha, C. Leonelli, A. Palomo, and P. Chindaprasirt, *Handbook of Alkali-Activated Cements, Mortars and Concretes, Handbook of Alkali-Activated Cements, Mortars and Concretes*, Elsevier, Cambridge, UK, 2015.

[83] G. Ye, P. Lura, K. Van Breugel, and A. L. A. Fraaij, "Study on the development of the microstructure in cement-based materials by means of numerical simulation and ultrasonic pulse velocity measurement," *Cement and Concrete Composites*, vol. 26, no. 5, pp. 491–497, 2004.

[84] A. M. Galaa, B. D. Thompson, M. W. Grabinsky, and W. F. Bawden, "Characterizing stiffness development in hydrating mine backfill using ultrasonic wave measurements," *Canadian Geotechnical Journal*, vol. 48, 2011.

[85] M. Fall and M. Pokharel, "Coupled effects of sulphate and temperature on the strength development of cemented tailings backfills: Portland cement-paste backfill," *Cement and Concrete Composites*, vol. 32, no. 10, pp. 819–828, 2010.

[86] T. Belem, B. Bussière, and M. Benzaazoua, "The effect of microstructural evolution on the physical properties of paste backfill," in *Proceedings of Tailings and Mine Waste*, pp. 5809–5818, Fort Collins, CO, USA, January 2001.

Hindawi
Advances in Materials Science and Engineering
Volume 2020, Article ID 6345206, 7 pages
https://doi.org/10.1155/2020/6345206

Research Article

Preparation and Mechanical Properties of Cemented Uranium Tailing Backfill Based on Alkali-Activated Slag

Fulin Wang, Guoliang Chen, Lu Ji, and Zhengping Yuan

School of Resource & Environment and Safety Engineering, University of South China, Hengyang 421001, China

Correspondence should be addressed to Fulin Wang; 2513625891@qq.com

Received 25 December 2019; Revised 28 February 2020; Accepted 20 March 2020; Published 25 April 2020

Guest Editor: Qiusong Chen

Backfilling disposal based on cement solidification is one of the ways to solve the environmental and safe problems of uranium tailing surface stacking. Alkali-activated slag, especially sodium silicate activated geopolymer, has become the preferred cementing material for the uranium tailing backfilling system because of its advantages of corrosion resistance and high strength. In this paper, uranium tailings and slag are taken as research objects, and the unconfined compressive strength (UCS) is taken as the main quality index. The preparation method of the cemented uranium tailing backfill based on alkali-activated slag was studied, hereinafter referred to as CUTB. The effects of additive amount, activator amount and activator modulus on the strength of CUTB were investigated. The results show that alkali-activated slag is an effective cementing material for the backfilling system of uranium tailing aggregate. The maximum UCS of 28 d age in the test groups is 16.45 MPa. Quicklime is an important additive for preparing CUTB. When the amount of quicklime is 0%, the early and late strengths of the filling body cannot be measured or at a very low level. At the age of 7 d, the order of each factor is additive amount > activator modulus > activator amount, but at the age of 28 d, the order of each factor is additive amount > activator amount > activator modulus. The test results can provide a basis for choosing cementitious materials for backfilling disposal of uranium tailings.

1. Introduction

Surface stacking is one of the most important disposal methods of uranium tailings, in which radioactive and nonradioactive materials migrate and disperse under the action of weathering leaching, causing pollution to soil, water, and air. However, as a kind of long-lived, large-volume and low (or extremely low) level radioactive solid waste, uranium tailings cannot be completely treated in the way of high (or medium) level radioactive solid waste disposal [1–5]. In the field of filling mining, paste filling has the characteristics of "no precipitation, no bleeding, and no segregation" and can effectively control the diffusion of harmful components in filling materials in groundwater, which is consistent with the principle of cement solidification method in radioactive solid waste [6–9]. Therefore, relevant experts put forward a method of backfilling disposal of uranium tailings based on cement solidification, which can effectively avoid the environmental and safe problems of surface stacking of uranium tailings. In order to avoid the secondary pollution of groundwater caused by uranium tailings filling underground, it requires that the filling body has better mechanical strength, chemical stability, and leaching resistance [10–13].

For the filling body formed by uranium tailings aggregate and cement cementitious material, the leaching resistance is closely related to the structural stability of the filling body, and the mechanical strength is the macroscopic performance of the stability. The structural stability of filling body is also related to the hydration and hardening products of cementitious materials. The hydration process of cementitious materials is affected by many factors, such as the physical and chemical properties of filling materials. Uranium tailings are generally characterized by containing radionuclides, sulfuric acid and heavy metals, multiple types of tailings formation and wide distribution of particle size, etc., which inevitably affect the hydration reaction and strength formation of cementing materials, thus affecting the

mechanical strength, chemical stability and leaching resistance of filling body.

Slag-based cementitious materials generally have the advantages of corrosion resistance and high post-strength and can also solve the problems of expansion, strength reduction, and even disintegration of high-sulfur tailing aggregate filling body [14–21]. Geopolymer cementitious materials have a "crystal-like" structure consisting of circular molecular chains, which can segment metal ions and other toxic substances into cavities and which is one of the effective methods for toxic and nuclear waste treatment [22–26]. Based on this, alkali-activated slag or slag polymer, as a substitute for traditional cementitious materials, can theoretically improve the structural stability of filling body and then improve its leaching resistance. However, there are few studies on the strength formation mechanism of cemented uranium tailing backfill based on alkali-activated slag in China and throughout the world, so it is necessary to carry out experimental research on this.

In this paper, uranium tailings were used as filling aggregate and alkali activated water-quenched slag powder as cementitious material. The corresponding filling slurry was prepared according to a certain cement-sand ratio and water-solid ratio. The rheological properties of the filling slurry were measured by the yield stress and the average viscosity. The mechanical strength of filling body was measured by UCS. The mechanical properties of the CUTB system and the influence of activator parameters on it were explored.

2. Materials and Methods

2.1. Test Materials. The test materials mainly include uranium tailings, water-quenched slag powder, quicklime powder, liquid sodium silicate, sodium hydroxide, and water (as shown in Figure 1).

Uranium tailings are taken from a uranium tailings reservoir in China, with water content of 10.91%, density of 2.55 t/m^3, and volume density of 1.375 t/m^3. The main chemical composition of experimental materials is shown in Table 1 (by XRF of PANalytical Axios), and the pH of uranium tailings was 5.29 by referring to "Soil quality-determination of pH" [27]. The particle size composition of tailings obtained by the screening method is shown in Figure 2. The particle size ranged from 45 to 425 microns, and the median particle size was 208 microns. The average particle size was close to the median particle size. The results show that the coefficient of uniformity is 2.31, the coefficient of curvature is 0.93, the grain size distribution of tailings is discontinuous, the grain size distribution is not uniform, and the gradation is not good.

The slag powder was taken from a building material company in Hunan Province, China. It is white powder with a specific surface area of 445 m^2/kg, and the main chemical composition is shown in Table 1. According to "Granulated blast furnace slag used for cement production" and the works on slag eco-cement [28–30], the chemical modulus K should not be less than 1.2 and the calculated $K = 1.81 > 1.2$, so the slag is qualified. Because the alkali modulus of slag $M_0 = 0.85 < 1$ and the active coefficient $M_a = 0.48 > 0.30$, the slag is acid slag but belongs to high-activity slag. Quicklime purchased from the market is white powder with a specific surface area of 400 m^2/kg, and the content of CaO is 94.78%. Sodium silicate was purchased from the market with a modulus of 2.80, Na_2O content of 10.27%, and SiO_2 content of 27.79%. Sodium hydroxide is commercially available as a 99% pure industrial flake NaOH for adjusting the sodium silicate modulus. Water was directly supplied by urban tap water.

2.2. Test Scheme. In order to explore the effects of three factors, namely, the addition of quicklime (additive), Na_2O alkali equivalent (activator addition), and activator modulus, on the rheological properties of filling slurry and strength formation of CUTB, the fixed water-solid ratio was 0.25, the cement-sand ratio was 1 : 4, the mass ratio of quicklime to cementing material was 0%, 4%, 6%, and 8%, the mass ratio of Na_2O alkali equivalent to cementing material was 0%, 4%, 6%, and 8%, and the activator modulus was 0.8, 1.0, 1.2, and 1.4, as shown in Table 2.

Test methods: as the particle size composition of uranium tailings is similar to that of construction sand, the preparation of filling slurry, the filling and curing of test mold, and the test of compressive strength shall refer to "Standard for test method of performance on building mortar" and the corresponding test method of tailing cemented backfill [31–34]. When the filling slurry preparation was completed, the yield stress and average viscosity of the slurry were obtained by testing the rheological parameters with MCR52 Modular Intelligent Advanced Rheometer. And, the prepared slurry was poured into right-prism molds of dimensions 70.7 mm × 70.7 mm×70.7 mm. The demoulded filling specimens were stored under laboratory conditions (20 ± 1°C, humidity ≥95%) for curing. The specimens of the 11th group of CUTB after 14 d curing are shown in Figure 3. Three parallel specimens were prepared for each group, and the UCS tests were carried out on RMT-150B tester at 7 d, 28 d, and 56 d, respectively. The test equipments are shown in Figure 4.

3. Results and Discussion

The rheological parameters of filling slurry under different excitation conditions and its UCS at different ages after filling body formation are shown in Table 3.

3.1. Stress-Strain Characteristics of CUTB. In order to study the general variation law of strength and deformation of CUTB during compression, the maximum compressive strength test data of 28 d age in group 9–16 are extracted and the stress-strain curve is plotted in Figure 5. It can be seen from Figure 5 that the CUTB shows a good bearing capacity after being compressed to a certain extent. The stress-strain curve can be divided into four stages: pore-crack compaction stage, elastic deformation to microelastic crack stable development stage, yield stage, and postfracture stage, which are basically similar to the characteristics of concrete.

(a) (b) (c) (d) (e)

Figure 1: Main test materials. (a) Uranium tailings, (b) water-quenched slag powder, (c) quicklime powder, (d) liquid sodium silicate, and (e) sodium hydroxide.

Table 1: Main chemical composition of test materials (%).

	SiO_2	Al_2O_3	SO_3	K_2O	Fe_2O_3	Na_2O	CaO	TiO_2	P_2O_5	MnO	MgO	U
Uranium tailings	86.057	6.038	2.426	2.365	1.544	0.500	0.377	0.207	0.133	—	0.100	0.037
Slag powder	32.861	15.651	2.262	0.561	0.567	0.499	40.444	0.998	0.030	0.722	5.024	—
Quicklime powder	1.24	0.540	—	0.070	0.411	0.351	94.78	0.036	0.009	0.006	2.31	—

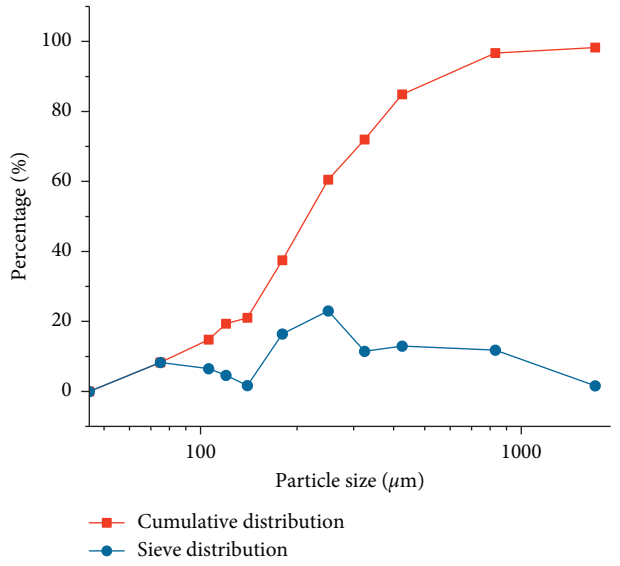

Figure 2: Particle size accumulation curve of uranium tailings.

3.1.1. Pore-Crack Compaction Stage. Because of discontinuous gradation of filling aggregate uranium tailings, uneven vibration during the pouring test, the structure of solid-adsorbed water-air in filling body is unavoidable to be adjusted at the initial stage of loading. Pores, microfissures, and bubbles in the filling body are closing gradually, and the specimen shows significant axial compression and transverse deformation. This is quite different from that of hard and compact rock specimens. When the filling body is compressed to a certain extent, the load-bearing capacity of the specimen is improved and even sudden changes occur.

3.1.2. Elastic Deformation Stage. After the load-bearing capacity of the specimens is obviously increased, the stress increases linearly with the strain as the load increases, and the specimens are in the stage of elastic deformation to stable development of microelastic crack.

Table 2: Orthogonal experimental table of slurry ratio.

Serial number	Quicklime (%)	Alkali equivalent (%)	Modulus
1	0	0	0.8
2	0	4	1.0
3	0	6	1.2
4	0	8	1.4
5	4	0	1.0
6	4	4	0.8
7	4	6	1.4
8	4	8	1.2
9	8	0	1.2
10	8	4	1.4
11	8	6	0.8
12	8	8	1.0
13	12	0	1.4
14	12	4	1.2
15	12	6	1.0
16	12	8	0.8

Figure 3: The 11th group of CUTB after 14 d curing.

3.1.3. Yield Stage. With the further increase of load, the microcracks in filling specimen gradually expand and change from elastic state to plastic state. The stress-strain curves of the specimens are concave and peak strength appears.

3.1.4. Failure Stage. After the specimen reaches its peak strength, the crack develops rapidly to form the

(a) (b)

Figure 4: The test equipments. (a) RMT-150B. (b) MCR52.

Table 3: Test results of mechanical properties.

Serial number	UCS (MPa)			Rheological parameter	
	R7	R28	R56	Yield stress (Pa)	Average viscosity (Pa·s)
1	—	—	—	167.19	6.52
2	—	0.06	—	288.98	8.62
3	—	0.12	—	343.33	11.48
4	0.20	0.23	—	264.75	8.17
5	1.70	5.98	9.22	198.97	6.68
6	4.90	8.76	10.66	297.85	12.17
7	—	12.71	10.05	316.14	9.55
8	0.72	16.45	6.05	494.81	14.28
9	0.20	5.67	10.34	186.40	8.24
10	3.90	6.23	9.86	413.88	12.08
11	6.43	9.28	9.25	331.11	11.07
12	7.55	11.08	11.47	221.60	5.96
13	2.07	6.95	10.32	155.85	4.54
14	5.15	8.05	7.87	302.32	8.57
15	6.57	10.68	7.51	339.49	9.38
16	5.20	9.77	10.27	250.97	6.87

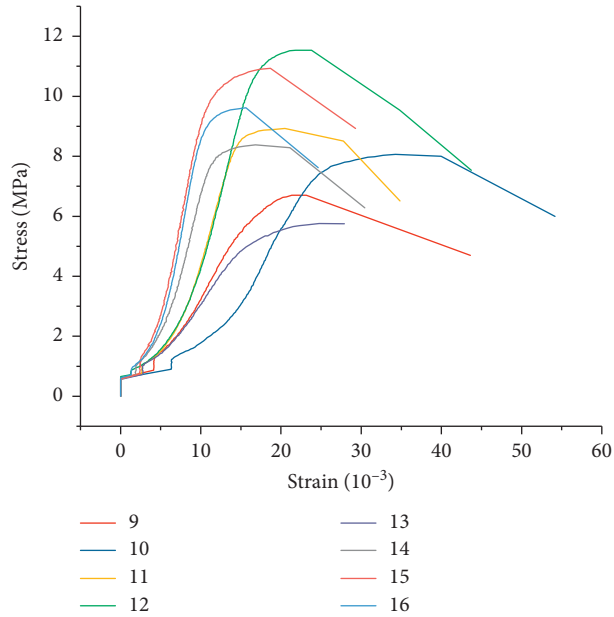

Figure 5: Stress-strain curve of CUTB.

macroscopic fracture surface, resulting in irreversible plastic deformation, and the bearing capacity of the specimen decreases significantly. However, unlike hard and compact rock mass, the stress-strain curve of filling body after fracture is relatively smooth, which indicates that filling body still has better bearing capacity and residual strength.

3.2. Orthogonal Analysis of Strength Characteristics of CUTB. In order to study the influence of quicklime addition, Na_2O alkali equivalent, and activator modulus on the strength formation of CUTB at fixed water-solid ratio and cement-sand ratio, the UCS of 16 groups of tests is analyzed by range analysis (as shown in Table 4 and Figure 6). The results show that the sensitivity of the influence on the strength of filling body is quicklime > activator modulus > alkali equivalent at 7 d age, and the optimal combination is A4B2C1. At 28 d age, the sensitivity of the influence on the strength of filling body is quicklime > alkali equivalent > activator modulus, and the optimal combination is A2B4C3.

For the cemented backfill of uranium tailing aggregate, the sulfur content and weak acid properties are unfavorable factors for the preparation of CUTB. As the most commonly used neutralizing treatment materials of uranium tailings, quicklime can not only neutralize the acid uranium tailings but also have good coagulation promotion as air-hardening binding material. From the experimental results of 7 d age and 28 d age, it can be seen that quicklime has obvious effect on the strength of filling body. When quicklime is not added, the strength of filling body cannot be formed or it is very low. In this case, the optimal test was group 4 and the strength of 28 d age was only 0.23 MPa. This is similar to the conclusion of papers [17, 19].

Table 4: Range analysis of UCS.

Age	Factor	Average UCS (MPa)				Range	Optimal scheme
		Level 1	Level 2	Level 3	Level 4		
7 d	A	0.050	1.830	4.520	4.748	4.698	A4
	B	0.992	3.488	3.250	3.417	2.496	B2
	C	4.133	3.955	1.518	1.542	2.615	C1
28 d	A	0.103	10.975	8.065	8.863	10.872	A2
	B	4.650	5.775	8.197	9.383	4.733	B4
	C	6.952	6.950	7.573	6.530	1.043	C3

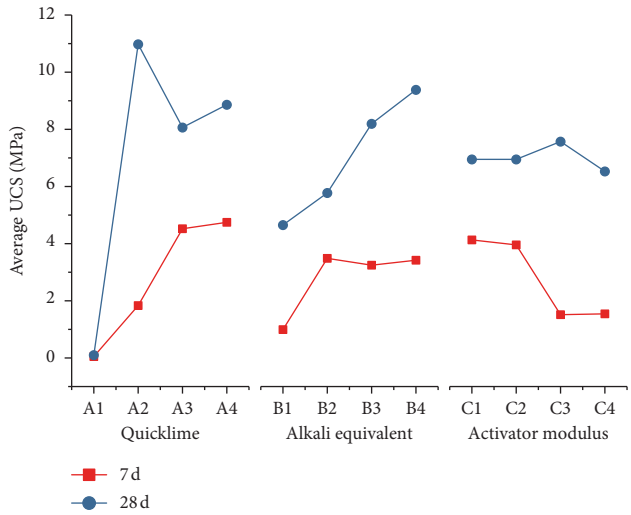

Figure 6: Trend chart of the average UCS VS factor level.

Table 5: Range analysis of rheological properties.

Age	Factor	Average value				Range	Optimal scheme
		Level 1	Level 2	Level 3	Level 4		
Yield stress	A	266.063	326.942	290.748	262.157	64.785	A4
	B	179.602	325.757	332.518	308.032	152.916	B1
	C	261.780	262.260	334.215	287.655	72.435	C1
Average viscosity	A	8.697	10.670	9.338	7.340	3.330	A4
	B	6.495	10.360	10.370	8.820	3.875	B1
	C	9.157	7.660	10.643	8.585	2.983	C2

When the activator modulus is low, the filling slurry is prone to rapid coagulation. Deb et al. [1] show that the strength of the backfill can reach 70%–80% of the final strength at 4 h. In 16 groups of tests, the strength of 28 d age specimens is generally 1.15–3.52 times of that of 7 d age specimens, and only the 8th and 9th groups of specimens are more than 22 times, but the 28 d age strength of the 9th group of specimens was only 5.67 MPa, which was due to the fact that only quicklime was used as cementitious material, but no cementitious material was added, and the content of quicklime in group 8 was less and the activation modulus was relatively high, which was the reason for the low strength at 7 d age.

3.3. Orthogonal Analysis of Rheological Properties of Filling Slurry. In order to study the rheological properties of filling slurry under fixed water-solid ratio and cement-sand ratio, the yield stress and average viscosity of 16 groups of tests were analyzed by range analysis (as shown in Table 5 and Figure 7). The results show that the sensitivity to the yield stress of slurry is alkali equivalent > activator modulus > quicklime, and the optimal combination is A4B1C1 with the minimum yield stress. The sensitivity to the average viscosity of slurry is alkali equivalent > quicklime > activator modulus, and the optimum combination is A4B1C2 with the minimum average viscosity index.

Only from the point of view of rheological properties, yield stress and average viscosity increase first and then decrease with the addition of quicklime, Na_2O alkali equivalent, and modulus of activator. The results can provide an optimum reference for industrial application of cemented uranium tailings backfill based on the alkali-activated slag system.

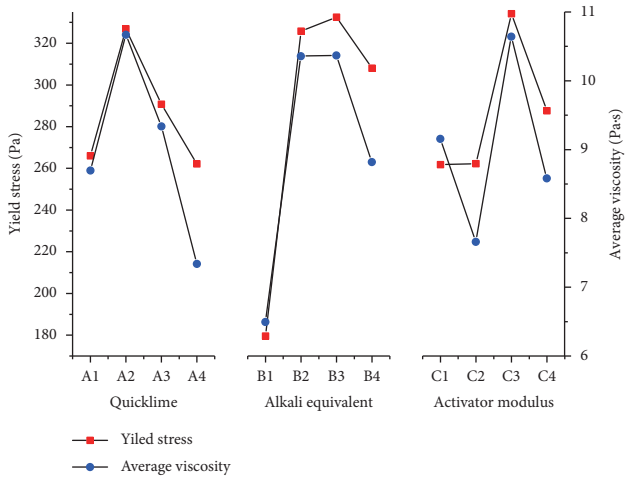

Figure 7: Trend chart of average yield stress and viscosity VS factor level.

4. Conclusions

Taking uranium tailings and slag as research objects, the preparation method of CUTB was studied by using the UCS quality index. The effects of additive amount, activator amount, and activator modulus on the strength of CUTB were investigated. The main conclusions are as follows:

(1) Alkali-activated slag is an effective cementing material for the uranium tailing aggregate filling system. The maximum UCS of 28 d age in the test groups is 16.45 MPa.

(2) Quicklime is an important additive for the preparation of CUTB. When the content of quicklime is 0%, the early and late strengths of filling body cannot be measured or can be done at a very low level.

(3) The activator modulus has a significant effect on the early strength of filling body, while the dosage of the activator has a significant effect on the later strength. At 7 d age, the order of each factor is the dosage of additive > the activator modulus> the dosage of activator. At 28 d age, the order of each factor is the dosage of additive > the dosage of activator > the activator modulus.

The cemented uranium tailing backfill based on alkali-activated slag is a new research content. This paper preliminarily verifies the feasibility of preparation of CUTB from the perspective of mechanical properties, but there are still several problems to be further explored in the future research:

(1) Under the influence of complex physical and chemical properties of uranium tailings, the hydration mechanism of alkali-activated slag cementitious material needs to be explored.

(2) The important goal of exploring CUTB is to solidify the uranium in uranium tailings, and its solidifying mechanism needs to be further explored.

(3) In order to give full play to the structural advantages of the geopolymer cementitious material solidified uranium, it is necessary to further explore the compounding test of the cementitious material admixture based on the concept of geopolymer.

Data Availability

All data are available within the article and can be obtained from the corresponding author upon request.

Conflicts of Interest

The authors declare that there are no conflicts of interest regarding the publication of this article.

Acknowledgments

This research was funded by the National Natural Science Foundation of China (51904154) and the research fund of Henan Key Laboratory for Green and Efficient Mining and Comprehensive Utilization of Mineral Resources (S201611). The authors gratefully acknowledge these generous supports.

References

[1] D. Deb, T. Sreenivas, G. K. Dey, and S. Panchal, "Paste backfill technology: essential characteristics and assessment of its application for mill rejects of uranium ores," *Transactions of the Indian Institute of Metals*, vol. 70, no. 2, pp. 487–495, 2017.

[2] H. A. Abdel Ghany, I. E. El Aassy, E. M. Ibrahim, and S. H. Gamil, "White sand potentially suppresses radon emission from uranium tailings," *Radiation Physics and Chemistry*, vol. 144, no. 3, pp. 100–105, 2018.

[3] S. Panchal, D. Deb, and T. Sreenivas, "Mill tailings based composites as paste backfill in mines of U-bearing dolomitic limestone ore," *Journal of Rock Mechanics and Geotechnical Engineering*, vol. 10, no. 2, pp. 310–322, 2018.

[4] A. Al-Hashimi, "Uranium tailings disposal: review of current technology," *International Journal of Environmental Studies*, vol. 42, no. 1, pp. 53–62, 1992.

[5] P. Waggitt, *A Review of Worldwide Practices for Disposal of Uranium Mill Tailings*, Australian Public Service, Australia, 1994.

[6] E. Yilmaz and M. Fall, *Paste Tailings Management*, Springer, Cham, Switzerland, 2017.

[7] A. X. Wu and H. J. Wang, *Theory and Technology of Paste Filling in Metal Mines*, Science Press, China, 2015.

[8] A. A. V. Cerbo, F. Ballesteros, T. C. Chen, and M.-C. Lu, "Solidification/stabilization of fly ash from city refuse incinerator facility and heavy metal sludge with cement additives," *Environmental Science and Pollution Research*, vol. 24, no. 2, pp. 1748–1756, 2017.

[9] D. L. Wang, Q. L. Zhang, Q. S. Chen, C. C. Qi, Y. Feng, and C. C. Xia, "Temperature variation characteristics in flocculation settlement of tailings and its mechanism," *International Journal of Minerals, Metallurgy and Materials*, vol. 28, no. 3, 2020.

[10] J. Kot'átková, J. Zatloukal, P. Reiterman, and K. Kolar, "Concrete and cement composites used for radioactive waste deposition," *Journal of Environmental Radioactivity*, vol. 178-179, pp. 147–155, 2017.

[11] Z. Z. Wang, "The practice and knowledge of uranium tailings disposal," *Uranium Mining and Metallurgy*, vol. 28, no. 1, pp. 22–25, 2009.

[12] G. Clausen and J. F. Archibald, "Uranium mill tailings as backfill in underground uranium mines," *Mining Science and Technology*, vol. 1, no. 1, pp. 69–75, 1983.

[13] B. M. Thomson, P. A. Longmire, and D. G. Brookins, "Geochemical constraints on underground disposal of uranium mill tailings," *Applied Geochemistry*, vol. 1, no. 3, pp. 335–343, 1986.

[14] M. Criado, S. A. Bernal, P. Garcia-Triñanes, and J. L. Provis, "Influence of slag composition on the stability of steel in alkali-activated cementitious materials," *Journal of Materials Science*, vol. 53, no. 7, pp. 5016–5035, 2018.

[15] Y. Feng, J. Kero, Q. X. Yang et al., "Mechanical activation of granulated copper slag and its influence on hydration heat and compressive strength of blended cement," *Materials*, vol. 12, no. 5, Article ID 12050772, 772 pages, 2019.

[16] A. Rustandi, F. W. Nawawi, Y. Pratesa, and A. Cahyadi, "Evaluation of the suitability of tin slag in cementitious materials: mechanical properties and Leaching behaviour," *Materials Science and Engineering*, vol. 299, no. 1 Article ID 012046, 2018.

[17] Y. Feng, Q. S. Chen, Y. L. Zhou et al., "Modification of glass structure via CaO addition in granulated copper slag to enhance its pozzolanic activity," *Construction and Building Materials*, vol. 240, Article ID 117970, 2020.

[18] F. Saly, L. P. Guo, R. Ma, and W. Sun, "Properties of steel slag and stainless steel slag as cement replacement materials: a comparative study," *Journal of Wuhan University of Technology (Materials Science)*, vol. 33, no. 6, pp. 156–163, 2018.

[19] H. Z. Jiao, S. F. Wang, A. X. Wu, H. M. Shen, and J. D. Wang, "Cementitious property of $NaAlO_2$-activated Ge slag as cement supplement," *International Journal of Minerals, Metallurgy and Materials*, vol. 26, no. 12, pp. 1594–1603, 2019.

[20] Y. He, Q. S. Chen, C. C. Qi, Q. L. Zhang, and C. C. Xiao, "Lithium slag and fly ash-based binder for cemented fine tailings backfill," *Journal of Environmental Management*, vol. 248, Article ID 109282, 2019.

[21] Y. Feng, Q. X. Yang, Q. S. Chen, and J. Kero, "Characterization and evaluation of the pozzolanic activity of granulated copper slag modified with CaO," *Journal of Cleaner Production*, vol. 232, pp. 1112–1120, 2019.

[22] A. Hajimohammadi and J. S. J. van Deventer, "Characterisation of one-part geopolymer binders made from fly ash," *Waste and Biomass Valorization*, vol. 8, no. 1, pp. 225–233, 2017.

[23] K. C. Onyelowe, D. Bui Van, and M. Nguyen Van, "Swelling potential, shrinkage and durability of cemented and uncemented lateritic soils treated with CWC base geopolymer," *International Journal of Geotechnical Engineering*, vol. 9, pp. 1–16, 2018.

[24] A. Nikolov, I. Rostovsky, and H. Nugteren, "Geopolymer materials based on natural zeolite," *Case Studies in Construction Materials*, vol. 6, pp. 198–205, 2017.

[25] A. Mehta and R. Siddique, "Strength, permeability and microstructural characteristics of low-calcium fly ash based geopolymers," *Construction and Building Materials*, vol. 141, pp. 325–334, 2017.

[26] A. Bhutta, M. Farooq, C. Zanotti, and N. Banthia, "Pull-out behavior of different fibers in geopolymer mortars: effects of alkaline solution concentration and curing," *Materials & Structures*, vol. 50, no. 1, p. 80, 2017.

[27] ISO, *Soil Quality-Determination of pH, ISO10390: 2005*, International Organization for Standardization, Geneva, Switzerland, 2005.

[28] Standardization Administration of China, *Granulated Blast Furnace Slag Used for Cement Production, GB/T 203-2008*, Standardization Administration of China, Beijing, China, 2008.

[29] H. S. Shi, *Eco-cement and Waste Recycling Technology*, Chemical Industry Press, Shanghai, China, 2005.

[30] Z. S. Lin, *Slag Base Serise Eco-Cement*, China Building Materials Press, Beijing, China, 2018.

[31] Chinese Construction Industry Standard, *Standard for Test Method of Performance on Building Mortar, JGJ/T70-2009*, Chinese Construction Industry Standard, Beijing, China, 2009.

[32] H. Z. Jiao, S. F. Wang, Y. X. Yang, and X. M. Chen, "Water recovery improvement by shearing of gravity-thickened tailings for cemented paste backfill," *Journal of Cleaner Production*, vol. 245, Article ID 118882, 2020.

[33] Z. Su, Q. S. Chen, Q. L. Zhang, and D. M. Zhang, "Recycling lead–zinc tailings for cemented paste backfill and stabilisation of excessive metal," *Minerals*, vol. 9, no. 11, Article ID 9110710. 710 pages, 2019.

[34] Q. S. Chen, Q. L. Zhang, C. C. Qi, A. Fourie, and C. C. Xiao, "Recycling phosphogypsum and construction demolition waste for cemented paste backfill and its environmental impact," *Journal of Cleaner Production*, vol. 186, pp. 418–429, 2018.

Hindawi
Advances in Materials Science and Engineering
Volume 2020, Article ID 3642356, 11 pages
https://doi.org/10.1155/2020/3642356

Research Article

Study on Damage Model and Damage Evolution Characteristics of Backfill with Prefabricated Fracture under Seepage-Stress Coupling

Jifeng Hou,[1,2] **Zhongping Guo**,[1] **Weizhen Liu**,[1] **Hengze Yang**,[1] **and WenWu Xie**[1]

[1]*College of Mining and Safety Engineering, Shandong University of Science and Technology, Shandong Qingdao 266590, China*
[2]*College of Coal Engineering, Shanxi Datong University, Shanxi Datong 037003, China*

Correspondence should be addressed to Zhongping Guo; gzp57046@sdust.edu.cn

Received 27 September 2019; Revised 25 December 2019; Accepted 27 January 2020; Published 9 March 2020

Guest Editor: Ferdi Cihangir

Aiming at the backfill with prefabricated fracture under seepage-stress coupling, the concepts of fracture macrodamage, loaded mesodamage, seepage mesodamage, and total damage of backfill were proposed. Based on the macroscopic statistical damage model, the coupling effect of seepage, stress, and initial fracture was considered comprehensively and the damage model of backfill with prefabricated fracture under seepage-stress coupling was established. The mechanical properties of backfill with prefabricated fracture under different seepage water pressures and confining pressures were tested and the rationality of the model was verified. The research shows that the mechanical properties of backfill with prefabricated fracture under the seepage-stress coupling are determined by the seepage water pressure, the load, the initial fracture, and the coupling effect. Fracture and seepage have significant effects on the damage of the backfill. When the seepage water pressure is low, the fracture damage dominates; however, when the seepage water pressure is high, the seepage damage dominates; the total damage under the coupling action is more serious than the single factor. The development laws of the total damage evolution curves under different seepage water pressures and confining pressures are basically the same, and they show the S-shaped distribution law with the increase of the axial strain. With the increase of confining pressure, the damage effect of fracture and seepage on the backfill is weakened, indicating that the confining pressure has a certain inhibitory effect on the damage evolution of the backfill. The research results can provide a theoretical basis for the study of the stability of backfill with geological defects such as joints and fractures in deep high-stress and high-seepage water pressure coal mines.

1. Introduction

Backfill coal mining technology is an effective method to improve the utilization of coal resources and control surface subsidence. It has been widely used in China and has become one of the main means of green coal mining [1–8]. The stability of the backfill is an important factor to prevent the instability of the goaf and the subsidence of the ground surface [9, 10]. Cemented coal gangue backfill is a common backfill method in coal mines [11–14]. However, in actual engineering, the influence of coal mining disturbance, blasting impact, and poor backfill effect can lead to a large number of fractures inside the backfill, which can easily reduce the strength of the backfill, and then it will cause the overall instability of the backfill working surface and the sinking of the surface [15]. For the intact backfill, the initial damage is considered to be zero and the initial mechanical properties of the backfill with prefabricated fracture are largely different from the nondestructive state. In addition, with the deep development of underground mining, high geostress and high seepage water pressure have become another important factor, affecting the stability of the backfill, and the two factors together affect the stability of the backfill [16–18]. Therefore, it is necessary to study the damage mechanical properties of backfill with prefabricated fracture under the coupling action of seepage and stress.

At present, many scholars at home and abroad have studied the fracture initiation, propagation law, and strength

degradation characteristics of rock with fractures and the influence of seepage on the permeability of rock materials. Hadi et al. [19, 20] found that there are two main types of fractures in fractured pozzolanic Portland cement samples: wing fractures and secondary fractures; as the number of fractures increases, the ultimate breaking load of the specimens decreases. Heek et al. [21] found that there are two kinds of mechanical mechanisms for fracture propagation in fractured rock: one is tensile stress alone, and the other is tensile stress and shear stress through experimental research. Liu et al. [22] studied the nonlinear flow characteristics of fluids at the intersection of rock mass fractures by means of the indoor permeable test and the charge-coupled body (CCD) camera visualization technology. Liu et al. [23] established an analytical model of nonlinear seepage parameters (permeability coefficient k and nonlinear coefficient b) of fractured rock mass based on Forchheimer equation for the nonlinear characteristics of flow-pressure curve of high-water pressure test. Wang et al. [24] carried out permeability tests of limestone fractures with different roughness, analyzed the influence of coupling effect of stress and seepage erosion on the surface morphology of rough fractures, and studied the evolution law of seepage characteristics.

The above literatures mainly were focused on the fracture initiation, propagation, and permeability characteristics of fracture-bearing rocks. However, there are few studies on the damage evolution characteristics of backfill with prefabricated fracture under seepage-stress coupling. In view of this, based on the macroscopic statistical damage model, comprehensively considering the coupling effect of seepage, stress, and initial fracture, the damage evolution model of backfill with prefabricated fracture under seepage-stress coupling was established and the damage evolution characteristics of backfill with prefabricated fracture under the seepage-stress coupling were studied and verified by laboratory test results. The research results can provide a theoretical basis for the study of the stability of backfill with geological defects such as joints and fractures in deep high-stress and high-seepage water pressure mines.

2. Damage Model of Backfill with Prefabricated Fracture under Seepage-Stress Coupling

2.1. Seepage Mesodamage of Backfill. Backfill is a kind of multiphase composite material with coal gangue, fly ash, and cement as cementitious materials, which has a lot of pores and fractures. Under the action of the seepage water pressure, the pores and fractures are expanded and connected, and the macroscopic performance is the deterioration of the mechanical properties of the backfill. The damage evolution law of microscopic and mesoscopic defects of the backfill under seepage conditions is very complicated. Since the damage degree of the backfill can be reflected by its external macroscopic mechanical properties, the macroscopic phenomenological damage mechanics method can be used to study the mesoscopic damage of the backfill under seepage conditions. According to the theory of damage mechanics, the seepage damage of the backfill is characterized by the change of mechanical parameters such as elastic modulus, and the damage variable of the seepage is defined as follows:

$$D_p = 1 - \frac{E_p}{E_0}, \tag{1}$$

where E_0 is elastic modulus of intact backfill; E_p is elastic modulus of intact backfill considering seepage.

2.2. Loaded Mesodamage of Backfill. The backfill is composed of a large number of microunits and the distribution of the mechanical properties of each microunit is random. The damage degree of the backfill is related to the defects contained in each microunit, and these defects directly affect the strength of the microunit. Therefore, there is the following relationship between the loaded damage variable D_s and the statistical distribution density function $\varphi(\varepsilon)$ of the microunit damage:

$$\varphi(\varepsilon) = \frac{\mathrm{d}D_s}{\mathrm{d}\varepsilon}, \tag{2}$$

where $\varphi(\varepsilon)$ is the measurement of the microunit damage rate of backfill during the loading process and the damage accumulation of microunit leads to the deterioration of the macroscopic performance of backfill. Assume that the microunit strength of backfill obeys the Weibull statistical distribution, the loaded damage variable D_s can be expressed as follows:

$$D_s = \int_0^{\varepsilon} \varphi(x)\mathrm{d}x = 1 - \exp\left[-\left(\frac{\varepsilon^*}{a}\right)^m\right], \tag{3}$$

where a, m are the distribution parameters, and ε^* is the microunit strain.

According to the strain equivalence principle proposed by Lemaitre [25], the constitutive relation of the damaged material is as follows:

$$\sigma = (1 - D_s)E_0\varepsilon. \tag{4}$$

From (2) and (3), it can be deduced that the loaded damage constitutive model of the backfill under pseudo-triaxial conditions is as follows:

$$\left.\begin{aligned} \sigma_1 &= E_0\varepsilon_1 \exp\left[-\left(\frac{\varepsilon^*}{a}\right)^m\right] + 2\mu\sigma_3 \\ (1-\mu)\sigma_3 &= E_0\varepsilon_3 \exp\left[-\left(\frac{\varepsilon^*}{a}\right)^m\right] + \mu\sigma_1 \end{aligned}\right\}. \tag{5}$$

Assume that the backfill obeys the Misses yield criterion and the Hooker theorem, the strain expression in equation (5) can be obtained as follows:

$$\left.\begin{aligned} \varepsilon_1^* &= \varepsilon_1 - \frac{(1-2\mu)\sigma_3}{E_0} \\ \varepsilon_3^* &= -\frac{\varepsilon_3}{\mu} + \frac{(1-2\mu)\sigma_3}{\mu E_0} \end{aligned}\right\}. \tag{6}$$

During the deformation and failure of the backfill, the stress-strain relationship at the peak point should satisfy the following geometric conditions: (1) When $\varepsilon_1 = \varepsilon_f$, $\sigma_1 = \sigma_f$

(2) When $\varepsilon_1 = \varepsilon_f$, $\partial\sigma_1/\partial\varepsilon_1 = 0$, where ε_f and σ_f are the strain and stress values at the extreme points of the stress-strain curve of the backfill, respectively.

According to the geometric conditions (1) and (2), the following can be derived from equations (5) and (6):

$$\left.\begin{aligned} a &= \left[\frac{\varepsilon_f - (1-2\mu)\sigma_3}{E_0}\right]\left[\frac{m\varepsilon_f}{\varepsilon_f - (1-2\mu)\sigma_3/E_0}\right]^{1/m} \\ m &= \frac{\varepsilon_f - (1-2\mu)\sigma_3/E_0}{\varepsilon_f \ln E_0\varepsilon_f/\sigma_f - 2\mu\sigma_3} \end{aligned}\right\}. \tag{7}$$

From equations (3) and (7), the loaded damage variable of backfill is as follows:

$$D_s = 1 - \exp\left\{\left[\frac{\varepsilon_1 - (1-2\mu)\sigma_3/E_0}{\varepsilon_f - (1-2\mu)\sigma_3/E_0}\right]^m \ln\frac{\sigma_f - 2\mu\sigma_3}{E_0\sigma_f}\right\}. \tag{8}$$

2.3. Mesodamage of Backfill under Seepage-Stress Coupling. According to the strain equivalence principle proposed by Lemaitre, the strain caused by the full stress σ acting on the damaged material is equivalent to the strain caused by the effective stress σ' acting on the nondestructive material. Therefore, the constitutive relation of the damaged material can be derived from the constitutive equation of the nondestructive material. As long as the nominal stress is replaced by the effective stress, the internal damage constitutive relation of the backfill is as follows:

$$\sigma = E_0(1 - D_s)\varepsilon, \tag{9}$$

where E_0 is elastic modulus of intact backfill; D_s is loaded damage variable of intact backfill.

According to the generalized strain equivalence principle proposed by Zhang et al. [26, 27], the seepage damage is regarded as the first damage state, and the loaded damage state after seepage damage is regarded as the second damage state. The internal damage constitutive relationship of the backfill is as follows:

$$\sigma = E_p(1 - D_s)\varepsilon. \tag{10}$$

The stress-strain constitutive relation expressed by the seepage and the loaded damage variable can be obtained from equations (1) and (10) as follows:

$$\sigma = E_0(1 - D_m)\varepsilon, \tag{11}$$

where

$$D_m = D_s + D_p - D_sD_p, \tag{12}$$

D_m is the seepage-load coupling damage of the backfill, and D_sD_p is the coupling term of the two kinds of damage.

Formula (12) shows that the damage of backfill is aggravated by the interaction of seepage and stress, but the total damage is not a simple superposition of seepage damage and loaded damage. The "–" sign before the coupling term indicates that the coupling effect of two stages of mesodamage reduces the total damage. According to the analysis, during the seepage process, the microdefects in the backfill are enhanced and the relative density is increased. Therefore, under the action of the load, the slip and displacement between the internal particles are hindered. During the loading process, the internal microdefects are closed and compacted, and the mesodefects are improved to alleviate the seepage damage.

From equations (1), (3), and (12), the damage evolution equation of the backfill under the action of seepage and load is as follows:

$$D_m = 1 - \frac{E_p}{E_0}\exp\left[-\left(\frac{\varepsilon^*}{a}\right)^m\right]. \tag{13}$$

2.4. Total Damage of Backfill with Prefabricated Fracture under Seepage-Stress Coupling. According to the theory of damage mechanics, the definition of damage variable is the premise and basis for the establishment of damage model. Therefore, the following is the first to discuss the damage variables of the backfill with prefabricated fracture under the seepage conditions, considering macroscopic and microscopic defects. The damage coupling of macroscopic and mesoscopic defects is concentrated as the coupling of damage variables.

In calculating the coupling of the damage variable of backfill with prefabricated fracture, the following basic assumptions are used: (1) Macroscopic damage and mesoscopic damage are visually and invisibly divided by human eyes and macroscopic and mesoscopic damage are considered to be isotropic damage. (2) The initial damage caused by the fracture to the backfill is defined as macroscopic damage D_1 and the damage caused by the seepage or the load is defined as mesoscopic damage D_2 and the coupling damage of seepage and load is D_{12}. (3) Coupling is based on the strain equivalent principle proposed by Lemaitre [25] and the two types of damage cannot be simply superposed.

As shown in Figure 1, it is assumed that Figures 1(a)–1(d), respectively, represent the backfill containing macroscopic and mesoscopic defects, the backfill only containing macroscopic defects, the backfill only containing mesoscopic defects, and the intact backfill [28]. The corresponding elastic moduli are, respectively, E_{12}, E_1, E_2, and E_0, and the corresponding strains under the action of external force are, respectively, ε_{12}, ε_1, ε_2, and ε_0. Based on the Lemaitre strain equivalence principle, then there is

$$\varepsilon_{12} = \varepsilon_1 + \varepsilon_2 - \varepsilon_0, \tag{14}$$

$$\frac{\sigma}{E_{12}} = \frac{\sigma}{E_1} + \frac{\sigma}{E_2} - \frac{\sigma}{E_0}. \tag{15}$$

From Lemaitre's hypothesis, we can see that

$$\begin{cases} E_{12} = E_0(1 - D_{12}), \\ E_1 = E_0(1 - D_1), \\ E_2 = E_0(1 - D_2). \end{cases} \tag{16}$$

Substituting Formula (16) into Formula (15), we can get the following formula:

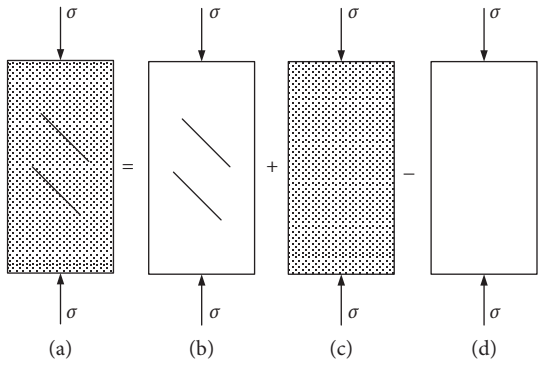

Figure 1: Schematic diagram of calculated equivalence strain.

$$D_{12} = 1 - \frac{(1 - D_1)(1 - D_2)}{1 - D_1 D_2}. \tag{17}$$

The initial damage state of the intact backfill is taken as the reference damage state, the damage caused by the prefabricated fracture is regarded as the macroscopic damage D_j, and the damage caused by the seepage and load coupling is regarded as the mesoscopic damage D_m. The total damage of the backfill with prefabricated fracture caused by the seepage-load coupling is regarded as the total damage D, then equation (17) is rewritten as follows:

$$D = 1 - \frac{(1 - D_j)(1 - D_m)}{1 - D_j D_m}, \tag{18}$$

where

$$D_j = 1 - \frac{E_j}{E_0}, \tag{19}$$

E_j is the elastic modulus of the backfill with prefabricated fracture.

Equations (13), (18), and (19) constitute a complete damage evolution model of backfill with prefabricated fracture, which takes into account the effects of seepage-stress coupling effects. The formula reflects the nonlinear characteristics of the interaction of seepage, load, and prefabricated fracture on the damage propagation of backfill. When the backfill is only affected by fracture, that is, $D_m = 0$, there is $D = D_j$; when the backfill does not contain macrodefects such as fractures, that is, $D_j = 0$, there is $D = D_m$.

According to the damage mechanics theory, the damage constitutive relation of the backfill with prefabricated fracture under the triaxial condition can be further deduced from formula (18):

$$\begin{cases} \sigma_1 = E_0 (1 - D)\varepsilon_1 + 2\mu_{jp}\sigma_3, \\ (1 - \mu_{jp})\sigma_3 = E_0 (1 - D)\varepsilon_3 + \mu_{jp}\sigma_1, \end{cases} \tag{20}$$

where μ_{jp} is Poisson ratio of the backfill with prefabricated fracture considering seepage.

Formulas (13), (18)–(20) constitute a complete damage constitutive equation of backfill with prefabricated fracture considering seepage-stress coupling effect.

From the above deductions, it can be seen that the stress at any point of backfill with prefabricated fracture under seepage-stress coupling is related to the fracture, seepage water pressure, ultimate strength, peak strain, and strain at that point. The distribution parameter m of backfill characterizes the brittleness of backfill; that is, the smaller the value of m, the more the plastic failure of backfill tends to be. The macroscopic strength of backfill is characterized by a.

3. Laboratory Experiments

3.1. Experimental Equipment. In order to verify the rationality and reliability of the above damage evolution model, the author performed three-axis compression tests under the seepage-stress coupling on the MTS815 rock mechanics test machine, as shown in Figure 2.

The system mainly tests the mechanical properties and seepage characteristics of high-strength and high-performance solid materials under complex stress conditions. The main features of the system are as follows: ① It can realize automatic data collection and processing by full computer control. ② Three independent servo systems are equipped, including axial pressure (maximum axial load is 280000 kN), confining pressure (maximum confining pressure is 80 MPa), and pore water pressure (maximum pore pressure is 80 MPa). ③ The servo response is fast (290 Hz) and the test accuracy is high. ④ The extensometer can work in high temperature and high pressure oil and can accurately measure the stress and strain of rock. ⑤ The test can be carried out with arbitrary loading waveform and rate. ⑥ The closed-loop heating system can provide a uniform temperature field and the maximum temperature is 200°C. The specimen size is a cylinder of ϕ50 mm × 100 mm and ϕ100 mm × 200 mm.

3.2. Materials Characteristics. The raw materials of the backfill are made up of coal gangue, fly ash, cement, and water according to a certain ratio. Coal gangue was taken from the gangue mountain of Daizhuang Coal Mine for secondary crushing, with the particle size between 0.1 and 15 mm. The fly ash was taken from the class II fly ash of Qingdao Power Plant. The cement was 32.5 ordinary Portland cement produced by Shandong Shanshui Cement Group Limited. The main chemical components of raw materials are shown in Table 1.

According to the engineering requirement of backfill coal mining, the State Key Laboratory of Mine Disaster Prevention and Control, which the author works in, has carried out a lot of tests and determined the mix proportion of backfill specimen, as shown in Table 2.

The uniformly stirred slurry was poured into a mold, and a fracture was prefabricated by a thin iron piece, the angle of the fracture is 45°, the length of the fracture is 20 mm, and the width of the fracture is 2.0 mm. According to the International Rock Mechanics Society (ISRM) test procedure, the cylinder specimens with a diameter of ϕ50 mm × 100 mm were made. After 1 day of maintenance, the mold was released and placed in a standard curing box

(a) (b)

Figure 2: The test apparatus. (a) MTS815 rock mechanics test system. (b) Test specimen installation details.

Table 1: Chemical composition of the main raw materials of backfill specimen.

Major element	Coal gangue (%)	Cement (%)	Fly ash (%)
SiO_2	56.1	22.95	52.35
Al_2O_3	18.6	5.32	32.60
Fe_2O_3	4.6	3.90	2.51
CaO	2.34	62.58	8.13
MgO	1.31	2.06	0.95
SO_3	0.12	2.33	0.51
LOI	10.23	2.58	11.62

Table 2: Mix proportion of backfill specimen.

Raw materials	Coal gangue (wt%)	Fly ash (wt%)	Cement (wt%)	Concentration (wt%)
Proportion	55	36	9	74

(relative humidity 95%, temperature 20°C) for 28 days. Before the test, each side of the specimen is ground flat with sandpaper, and the processing accuracy meets the rock test standard.

3.3. Experimental Method. Experimental steps: (a) Seal and wrap the specimen with heat shrinkable tube, then install it on the base of the test machine after installing axial and circumferential extensometers, as shown in Figure 2(b). (b) Control the hydraulic pump to apply confining pressure σ_3 to a predetermined value and keep it unchanged. (c) Apply seepage water pressure p_1 and p_2 ($\sigma_3 > p_1 \geq p_2 = 0$ MPa), respectively, on the upper and lower ends of the specimen, so as to form a stable seepage pressure difference at both ends of the specimen. (d) Adopt displacement loading method; the loading rate is 0.02 mm/min and the loading is continued until the specimen is broken. During the loading process, the stress-strain curve of the specimen is automatically recorded by computer. The stress mode of backfill specimen is shown in Figure 3.

Considering the feasibility of testing instruments and the rationality of pressure setting, the seepage water pressure at the inlet end of the specimen was set to 0 MPa, 0.3 MPa, 0.6 MPa, 0.9 MPa, and 1.2 MPa, and the outlet end of the specimen was connected to the atmosphere and the confining pressure was set to 0.5 MPa, 1.0 MPa, 1.5 MPa, and 2.0 MPa. The specific experimental scheme is shown in Table 3.

3.4. Model Verification. In order to verify the correctness and rationality of the damage constitutive model established in this paper, the stress-strain curves are drawn by the constitutive model and the experimental data and compared with the experimental curves of backfill with prefabricated fracture under different seepage water pressures (as shown in Figure 4).

It can be seen from Figure 4 that the theoretical calculation curves before peak strain are highly consistent with the experimental curves; the stress-strain curves are approximately linear; the post-peak curves are poorly consistent, but the basic trend is the same. Generally speaking, the damage constitutive model of the backfill with prefabricated fracture established in this paper is in good agreement with the experimental curves in both curve law and numerical value and can better reflect the stress-strain relationship of the backfill with prefabricated fracture specimen under seepage-stress coupling action. It can be used to analyze the damage evolution characteristics of

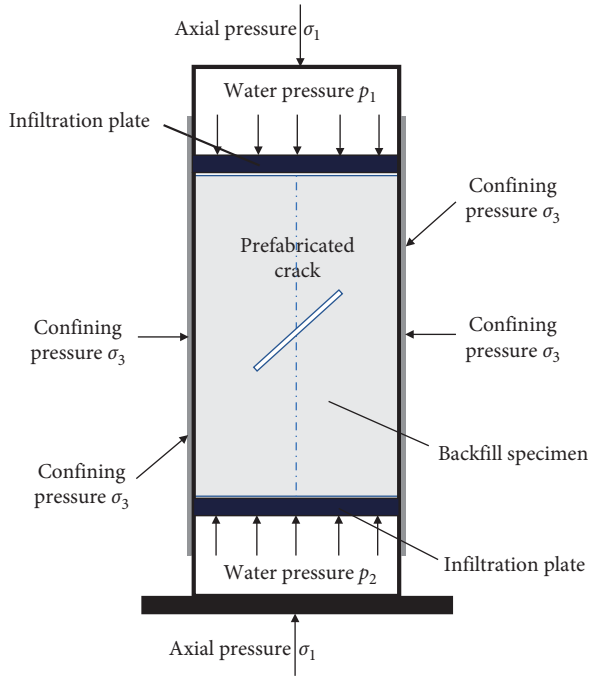

Figure 3: Loading diagram of backfill specimen.

Table 3: Experiment scheme.

Test number	Intact backfill specimens		Backfill specimens with prefabricated fracture		Remarks
	Seepage water pressure (MPa)	Initial confining pressure (MPa)	Seepage water pressure (MPa)	Initial confining pressure (MPa)	
1	0	1.5	0	1.5	Samples are saturated
2	0.3	1.5	0.3	1.5	
3	0.6	1.5	0.6	1.5	
4	0.9	1.5	0.9	1.5	
5	1.2	1.5	1.2	1.5	
6	0.3	0.5	0.3	0.5	
7	0.3	1.0	0.3	1.0	
8	0.3	1.5	0.3	1.5	
9	0.3	2.0	0.3	2.0	

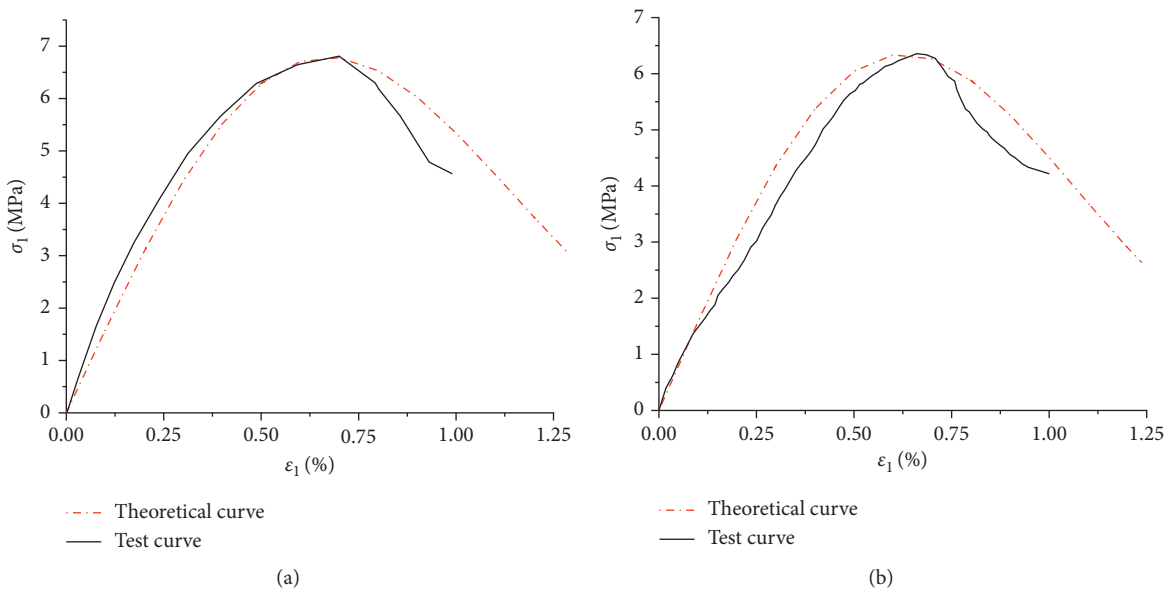

Figure 4: Continued.

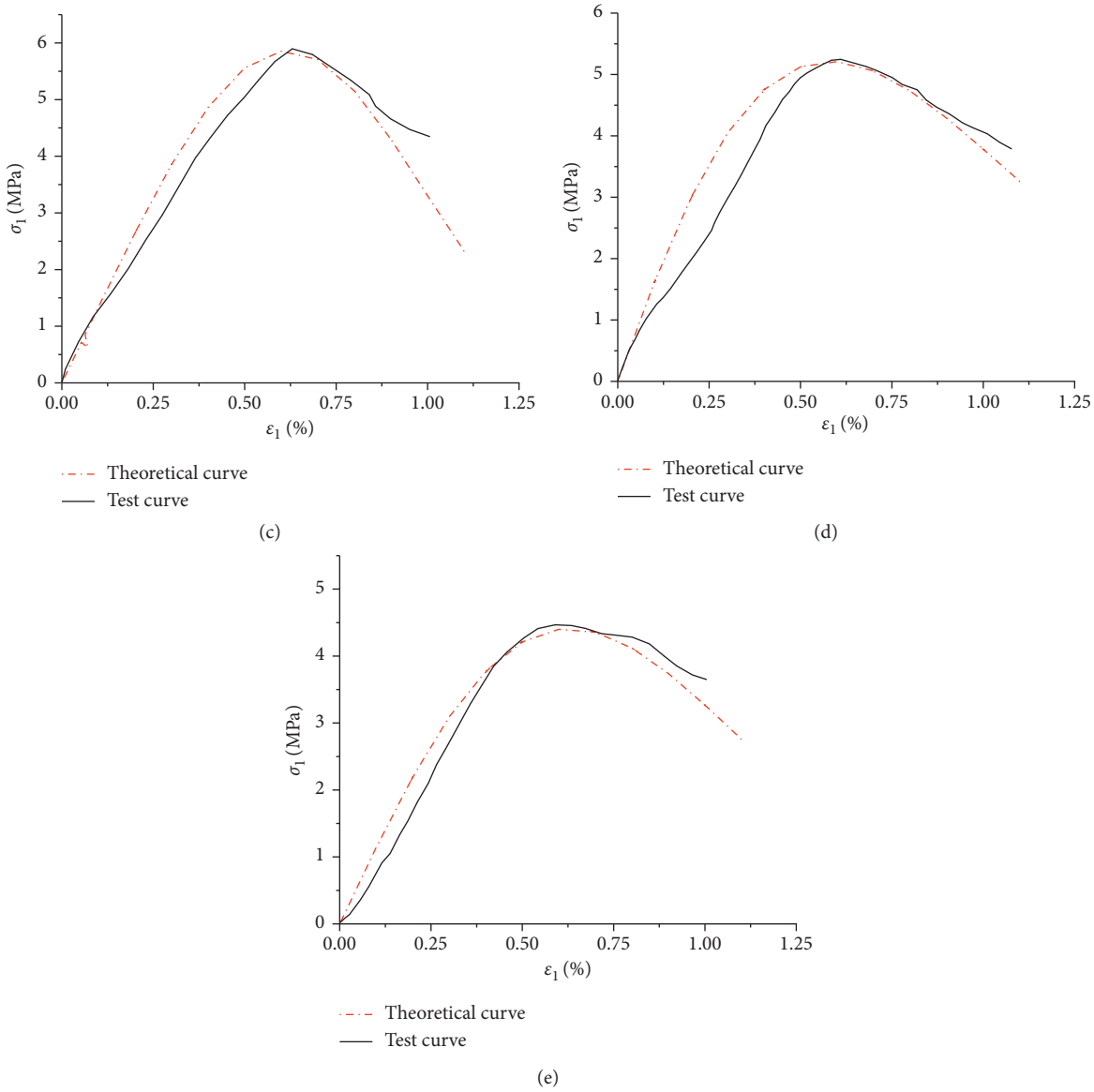

Figure 4: Calculated values of damage evolution model contrast with experimental values. (a) $p = 0$ MPa. (b) $p = 0.3$ MPa. (c) $p = 0.6$ MPa. (d) $p = 0.9$ MPa. (e) $p = 1.2$ MPa.

backfill with prefabricated fracture under seepage-stress coupling.

4. Damage Evolution Characteristics Analysis

4.1. Influence of Seepage on Backfill Damage. According to the mechanical parameters of the backfill under different seepage water pressures and formula (18), the intrinsic relationship between the seepage damage and the seepage water pressure can be obtained, as shown in Figure 5.

It can be seen from Figure 5 that there is seepage damage inside the backfill under the action of seepage, the seepage damage of the backfill increases with the increase of the seepage water pressure, especially in the presence of fractures, and the degree of damage is significantly different. Initial fracture damage D_j, seepage damage D_p, and seepage-fracture coupling damage D_{jp} were 0.16, 0.05–0.40, and 0.25–0.53, respectively.

It can be seen that fracture and seepage have a significant influence on the strength of backfill. Fracture damage dominates at low seepage water pressures, seepage damage dominates at high seepage water pressures, and total damage under the coupling action is more serious than that under single factor. Therefore, in the deep high-stress, high-permeability water-pressure mines, fractures in the backfill should be avoided as much as possible due to factors such as mining disturbance, blasting impact, or poor filling effect, so as to avoid the coupling effect to accelerate the damage development of the backfill.

Figure 6 shows the damage evolution curves of the backfill under different seepage water pressures when the confining pressure is 1.5 MPa. It can be seen in Figure 6.

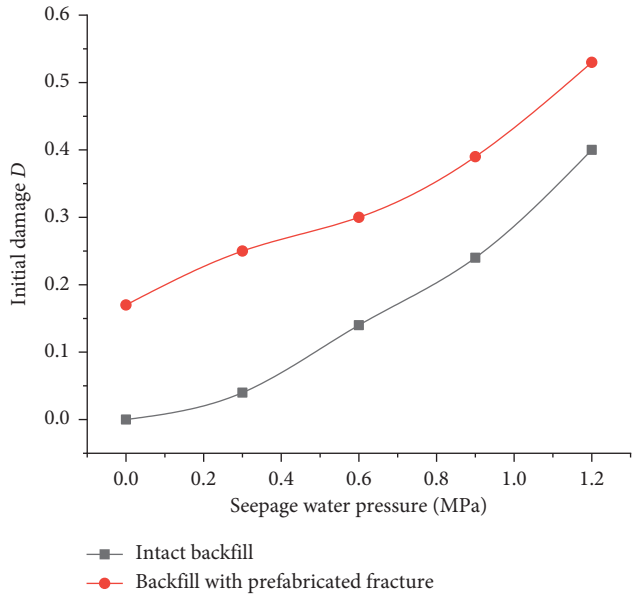

Figure 5: Relationship curves between initial damage and seepage water pressure.

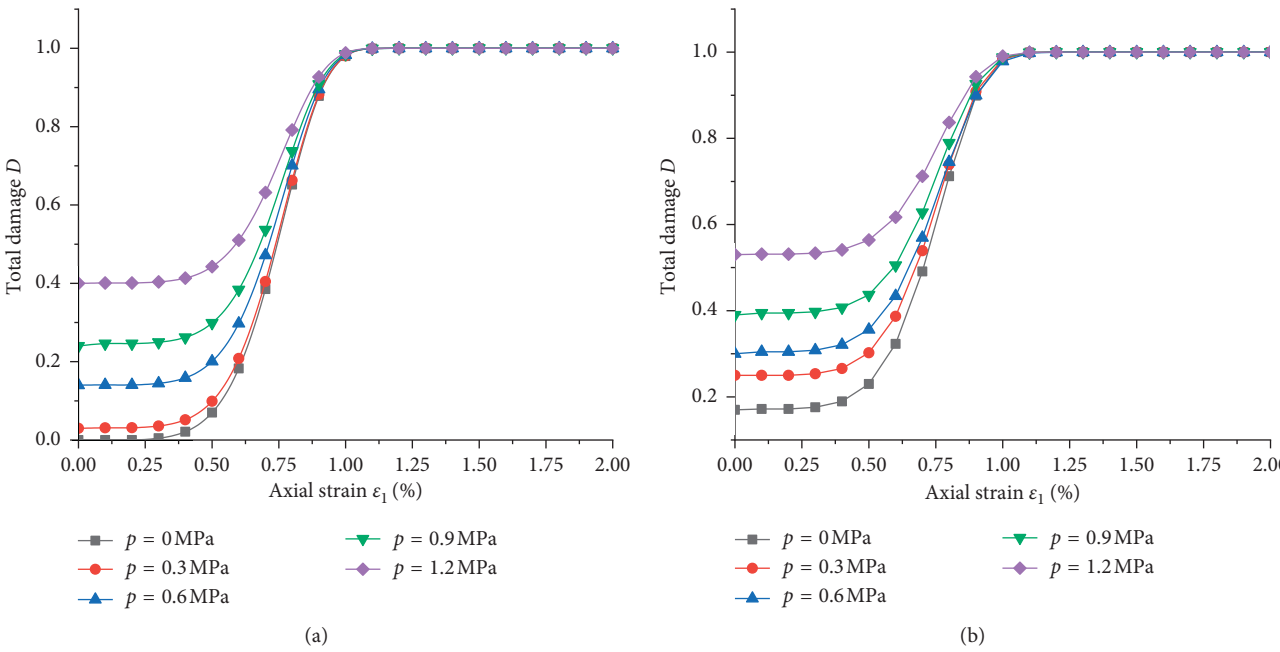

Figure 6: Damage evolution curves of backfill under different seepage water pressures. (a) Intact backfill. (b) Backfill with prefabricated fracture.

For the intact backfill, the total damage evolution law generally presents an S-shaped distribution with the increase of axial strain. At the initial stage of loading, the micropores and microfractures of the backfill are "compressed" to reduce the porosity and increase the density of the backfill, showing a compaction stage, and then the backfill is in a linear development stage. With the increase of axial strain, the micropores and microfractures in the backfill develop and evolve continuously, and the damage accelerates until the damage variable tends to 1. The whole process reflects the continuous generation and expansion of microfractures in the backfill from the microscopic point of view, and the deterioration of the mechanical properties of backfill from the macroscopic point of view. The development trend of damage evolution curves of backfill with prefabricated fracture is similar to that of intact backfill; that is, the existence of prefabricated fracture does not affect the development trend of damage evolution curves.

For the intact backfill, when the strain is 0, the initial damage of the backfill is the seepage mesodamage. For backfill with prefabricated fracture, when the strain is 0, the initial damage of backfill is the coupling damage of seepage

and fracture. With the increase of seepage water pressure, the initial damage increases gradually, and the cumulative damage process is more significant. It shows that the inclined section of damage evolution curves is shortened, and the macroscopic performance is that the backfill reaches the failure faster and the residual strength is lower.

For the intact backfill, when the seepage water pressure increases from 0.0 MPa to 1.2 MPa, the initial seepage damage of the backfill increases from 0.0 to 0.40. The value of seepage damage is relatively small, indicating that the mechanical properties of the backfill are mainly affected by the load at this time, and its compressive capacity is strong, but with the increase of the seepage water pressure, its compressive capacity is gradually weakened. For backfill with prefabricated fracture, when the seepage water pressure is 1.2 MPa, the initial seepage damage is 0.53, which is relatively large, indicating that the mechanical properties of the backfill are mainly affected by the coupling effect of fracture and seepage and its compressive capacity is poor.

4.2. Influence of Confining Pressure on Backfill Damage. It can be seen from Figure 7 that the development trend of the damage evolution curves of the backfill under different confining pressure conditions is basically the same. With the increase of the axial strain, the damage evolution curves show an S-type development trend. The development trend of the curves is slightly different under different confining pressure conditions. For the same strain value, the larger the confining pressure is, the smaller the total damage of the backfill is.

As can be seen from Figure 7(a), the initial seepage damage of the backfill decreases with the increase of confining pressure and the damage accumulation process becomes slower. It shows that the inclined section of the damage evolution curves increases and the macroscopic performance shows that the backfill achieves slower damage and higher residual strength. For example, when the confining pressure increases from 0.5 MPa to 2.0 MPa, the initial seepage damage of the backfill decreases from 0.14 to 0.02 and the drop rate reaches 0.12, which is 85.7% lower. It shows that, with the increase of confining pressure, the damage and degradation effect of seepage on the strength of the backfill is weakened. This is because the high confining pressure suppresses the expansion of the fracture in the backfill and the internal fracture is tightly closed.

It can be seen from Figure 7(b) that, under the same confining pressure and seepage water pressure, the initial damage of the backfill with prefabricated fracture is greater than that of the intact backfill. Compared with the intact backfill, when the confining pressure increases from 0.5 MPa to 2.0 MPa, the initial damage of the backfill with prefabricated fracture increases by 0.32, 0.21, 0.13, and 0.08, respectively. It indicates that the prefabricated fracture deteriorates the strength of the backfill, but as the confining pressure increases, the damage of the prefabricated fracture to the strength of the backfill is weakened.

5. Discussion

We have shown that the damage evolution model of backfill established by the macrostatistical damage model, considering the coupling effect of seepage, stress, and initial fracture, is highly consistent with the test curve. Based on the damage evolution model and test data, the damage evolution characteristics of the backfill with prefabricated fracture under the seepage stress coupling were analyzed. We found that prefabricated fractures and seepage have significant effects on the damage of the backfill, and the total damage under the coupling is more serious than that under the single factor. By comparing the total damage evolution curves of backfill under different confining pressure conditions, we found that confining pressure has a certain inhibitory effect on the damage evolution of backfill, which is consistent with the conclusions of laboratory tests.

Liu et al. [29] revealed the three-dimensional damage and energy consumption law of backfill with different proportions according to the mechanical test of four kinds of cement tailing backfill with different proportions of lime sand; Zhao and Liu [30, 31] and other researchers established the damage constitutive model of backfill under uniaxial compression, based on the statistical damage theory. Zhang [32] established two different damage constitutive equations by studying the microdamage mechanism of backfill. The above literatures are based on the macrostatistical damage model, the damage evolution model of the backfill and the damage characteristics of the backfill under load are analyzed and studied. It is found that the damage evolution curve of the backfill is S-shaped as the axial strain increases, and it is consistent with the conclusion of this paper. However, the above literature does not consider the influence of seepage and prefabricated cracks on the damage of backfill. According to the research in this paper, it is found that prefabricated fractures and seepage have significant effects on the damage of the backfill, and the total damage under the coupling effect is more serious than that under the single factor. Therefore, it is of great theoretical and engineering significance to introduce seepage and cracks into the damage evolution model of the backfill.

The primary contribution of this paper is proposing the concepts of fracture macrodamage, loaded mesodamage, seepage mesodamage, and total damage of the backfill and establishing the damage evolution model of backfill with prefabricated fracture considering the coupling effect of seepage and stress. The damage constitutive equation is expected to promote mining development in the following aspects: (a) understanding the damage constitutive relationship and deformation characteristics of the backfill with prefabricated fracture; (b) providing an accurate constitutive model for the backfill with prefabricated fracture under the coupling of seepage and stress; (c) identifying potential risks by estimating the stability of backfill after filling mining in deep high-stress and high-seepage water pressure mine.

The omission of chemical factors is a clear limitation of the current study, because the chemical composition of underground water in coal mines is relatively

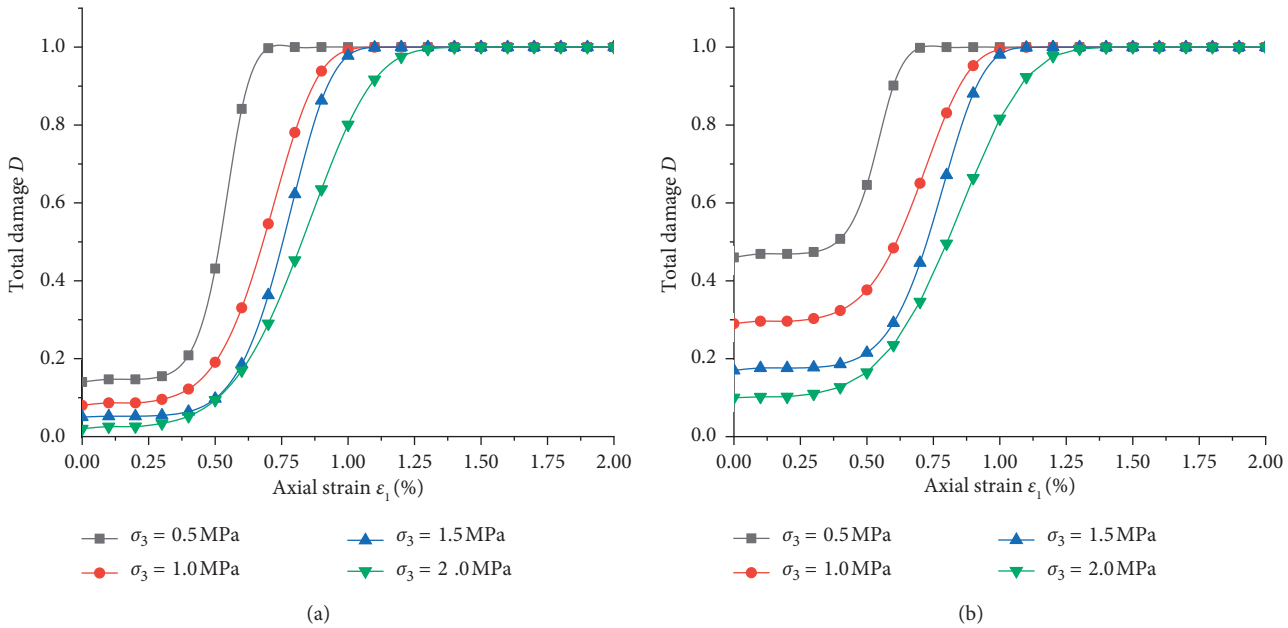

Figure 7: Damage evolution curves of backfill under different confining pressures. (a) Intact backfill. (b) Backfill with prefabricated fracture.

complex. Another limitation is that the number of tests is very small and only one kind mix proportion of backfill is studied.

6. Conclusions

(1) The concepts of fracture macrodamage, loaded mesodamage, seepage mesodamage, and total damage of backfill were proposed and the damage evolution model of backfill with prefabricated fracture considering the coupling effect of seepage and stress was established. The damage model established in this paper is in good agreement with the laboratory test results, can better reveal the damage evolution laws of the backfill with prefabricated fracture under seepage-stress coupling, and has certain rationality and feasibility.

(2) Fracture and seepage have significant effects on the damage and deterioration of the backfill. When the seepage water pressure is low, the fracture damage dominates; however, when the seepage water pressure is high, the seepage damage dominates; the total damage under the coupling action is more serious than the single factor.

(3) The development laws of the total damage evolution curves under different seepage water pressure and confining pressure are basically the same and the overall distribution is "S" type with the increase of axial strain. With the increase of confining pressure, the damage degradation effect of fracture and seepage on the strength of backfill is weakened and it indicates that confining pressure has a certain inhibition effect on the damage evolution of backfill.

Data Availability

All data are available within the article or can be obtained from the corresponding author upon request.

Conflicts of Interest

The authors declare that they have no conflicts of interest.

Acknowledgments

This work was supported by National Natural Science Foundation of China (Grant No. 51774195) and National Key Research and Development Program (2018YFC0604700).

References

[1] F. Cihangir, B. Ercikdi, A. Kesimal, A. Turan, and H. Deveci, "Utilisation of alkali-activated blast furnace slag in paste backfill of high-sulphide mill tailings: effect of binder type and dosage," *Minerals Engineering*, vol. 30, pp. 33–43, 2012.

[2] B. Cui, Y. Liu, H. Guo, Z. Liu, and Y. Lu, "Experimental study on the durability of fly ash-based filling paste in environments with different concentrations of sulfates," *Advances in Materials Science and Engineering*, vol. 2018, Article ID 4315345, 12 pages, 2018.

[3] C. C. Qi and A. Fourie, "Cemented paste backfill for mineral tailings management: review and future perspectives," *Minerals Engineering*, vol. 144, Article ID 106025, 2019.

[4] B. Ercikdi, F. Cihangir, A. Kesimal, and H. Deveci, "Practical importance of tailings for cemented paste backfill," *Paste Tailings Management*, pp. 7–32, 2017.

[5] S. Chen, D. Yin, F. Cao, Y. Liu, and K. Ren, "An overview of integrated surface subsidence-reducing technology in mining areas of China," *Natural Hazards*, vol. 81, no. 2, pp. 1129–1145, 2016.

[6] W. Zhu, J. Xu, J. Xu, D. Chen, and J. Shi, "Pier-column backfill mining technology for controlling surface subsidence," *International Journal of Rock Mechanics and Mining Sciences*, vol. 96, pp. 58–65, 2017.

[7] M. Li, J. X. Zhang, Y. L. Huang, and N. Zhou, "Effects of particle size of crushed gangue backfill materials on surface subsidence and its application under buildings," *Environmental Earth Sciences*, vol. 76, no. 17, pp. 603–620, 2017.

[8] Y. H. Yu and L. Q. Ma, "Application of roadway backfill mining in water-conservation coal mining: a case study in Northern Shaanxi, China," *Sustainability*, vol. 11, no. 13, pp. 1–22, 2019.

[9] M. Li, J. X. Zhang, X. X. Miao et al., "Strata movement under compaction of solid backfill," *Journal of China University of Mining and Technology*, vol. 43, no. 6, pp. 969–973, 2014.

[10] J. C. Wang and S. L. Yang, "Research on support-rock system in solid backfill mining methods," *Journal of China Coal Society*, vol. 35, no. 11, pp. 1821–1826, 2010.

[11] Q. D. Qu, L. Yao, X. H. Li et al., "Key factors affecting control surface subsidence in backfilling mining," *Journal of Mining & Safety Engineering*, vol. 27, no. 4, pp. 458–462, 2010.

[12] S. J. Chen, W. J. Guo, H. Zhou, and W. Guo-Hui, "Structure model and movement law of overburden during strip pillar mining backfill with cream-body," *Journal of China Coal Society*, vol. 36, no. 7, pp. 1081–1086, 2011.

[13] A. Fourie, M. Fahey, and M. Helinski, "Consolidation in accreting sediments: gibson's solution applied to backfilling of mine stopes," *Geotechnique*, vol. 60, no. 11, pp. 877–882, 2010.

[14] M. K. Mishra and U. M. R. Karanam, "Geotechnical characterization of fly ash composites for backfilling mine voids," *Geotechnical and Geological Engineering*, vol. 24, no. 6, pp. 1749–1765, 2006.

[15] W. B. Xu, C. B. Wan, and X. C. Tian, "Growth distribution laws and characterization methods of cracks of compact sandstone subjected to triaxial stress," *Journal of Mining & Safety Engineering*, vol. 35, no. 3, pp. 612–619, 2018.

[16] J. X. Fu, C. F. Du, and W. D. Song, "Strength sensitivity and failure mechanism of full tailings cemented backfills," *Journal of University of Science and Technology Beijing*, vol. 36, no. 9, pp. 1149–1157, 2014.

[17] C. H. Park and A. Bobet, "Crack coalescence in specimens with open and closed flaws: a comparison: a comparison," *International Journal of Rock Mechanics and Mining Sciences*, vol. 46, no. 5, pp. 819–829, 2009.

[18] Y. M. Yang, Y. Ju, L. T. Mao et al., "Growth distribution laws and characterization methods of cracks of compact sandstone subjected to triaxial stress," *Chinese Journal of Geotechnical Engineering*, vol. 36, no. 5, pp. 864–872, 2014.

[19] H. Hadi, K. Shahriar, M. F. Marji, and P. Moarefvand, "Cracks coalescence mechanism and cracks propagation paths in rock-like specimens containing pre-existing random cracks under compression," *Journal of Central South University*, vol. 21, no. 6, pp. 2404–2414, 2014.

[20] H. Hadi, A. Khaloo, and M. F. Marji, "Experimental and numerical analysis of Brazilian discs with multiple parallel cracks," *Arabian Journal of Geosciences*, vol. 8, no. 8, pp. 5897–5908, 2015.

[21] W. L. Heek and S. Jeon, "An experimental and numerical study of fracture coalescence in pre-cracked specimen under uniaxial compression," *International Journal of Solids and Structures*, vol. 48, no. 6, pp. 979–999, 2011.

[22] R. C. Liu, Y. J. Jiang, B. Li, L. yuan, and D. Yan, "Nonlinear seepage behaviors of fluid in fracture networks," *Rock and Soil Mechanics*, vol. 37, no. 10, pp. 2817–2824, 2016.

[23] M. M. Liu, S. H. Hu, Y. F. Chen et al., "An analytical model for nonlinear flow parameters of fractured rock masses based on high pressure packer tests," *Journal of Hydraulic Engineering*, vol. 47, no. 6, pp. 752–762, 2016.

[24] K. Wang, J. C. Sheng, H. C. Gao et al., "Study on seepage characteristics of rough fracture under the coupling action of stress seepage erosion," *Rock and Soil Mechanics*, vol. 41, no. 1, pp. 1–9, 2019.

[25] J. Lemaitre, *A Course on Damage Mechanics*, Springer-Verlag, Berlin, Germany, 1996.

[26] Q. S. Zhang, G. S. Yang, and J. X. Ren, "New study of damage variable and constitutive equation of rock," *Chinese Journal of Rock Mechanics and Engineering*, vol. 22, no. 1, pp. 30–34, 2003.

[27] H. M. Zhang and G. S. Yang, "Research on damage model of rock under coupling action of freeze-thaw and load," *Chinese Journal of Rock Mechanics and Engineering*, vol. 29, no. 3, pp. 471–476, 2010.

[28] L. M. Zhang, S. R. Lv, and H. Y. Liu, "A dynamic damage constitutive model of rock mass by comprehensively considering macroscopic and mesoscopic flaws," *Explosion and Shock Waves*, vol. 35, no. 3, pp. 428–436, 2015.

[29] Z. X. Liu, X. B. Li, G. Y. Zhao et al., "Three-dimensional energy dissipation laws and reasonable matches between backfill and rock mass," *Chinese Journal of Rock Mechanics and Engineering*, vol. 29, no. 2, pp. 344–348, 2010.

[30] S. G. Zhao, D. L. Su, W. R. Wu et al., "Study on damage model of backfill based on Weibull distribution under uniaxial compression," *China Mining Magazine*, vol. 26, no. 2, pp. 106–111, 2017.

[31] Z. X. Liu, Q. L. Liu, and W. G. Dang, "On softening-hardening intrinsically constitutive model for damage of tailings-cemented filling body," *Journal of Shandong University of Science and Technology (Natural Science)*, vol. 31, no. 2, pp. 36–41, 2012.

[32] F. W. Zhang, *Investigations on solidified characteristics and mechanism of slag cementitious materials in mine filling*, Ph.D. dissertation, Wuhan University, Wuhan, Hubei, China, 2009.

Hindawi
Advances in Materials Science and Engineering
Volume 2020, Article ID 1918278, 12 pages
https://doi.org/10.1155/2020/1918278

Research Article

Design and Application of Rapid Dewatering for Tailings Containing Sodium Silicate: Laboratory and Industrial Test Results

Guoquan Sun,[1,2] Keping Zhou,[1] Qian Kang,[1,2,3] Daolin Wang,[1] and Chongchun Xiao[4]

[1]*School of Resources and Safety Engineering, Central South University, Changsha 410083, China*
[2]*Sinosteel Maanshan General Institute of Mining Research Co., Ltd., Maanshan 243000, China*
[3]*School of Resources & Environment and Safety Engineering, University of South China, Hengyang 421001, China*
[4]*Feny Co., Ltd., Changsha 410083, China*

Correspondence should be addressed to Qian Kang; 79338186@qq.com

Received 19 October 2019; Accepted 31 January 2020; Published 28 February 2020

Guest Editor: Qi Jia

Focusing on the tailings containing high sodium silicate (water glass), this study conducted laboratory experiments and semi-industrial tests of flocculation and sedimentation for rapid tailings dewatering. Various reagent combinations, lime and anionic flocculant (APAM) (L&A), sulfuric acid and APAM (S&A), and calcium chloride and APAM (C&A), were tested. The results show that (i) all the three combinations presented a good effect in the laboratory experiments, and the relatively optimum dosages were L&A of 2 kg/t & 30 g/t, S&A of 2.6 kg/t & 20 g/t, and C&A of 3 kg/t & 30 g/t. (ii) The overflow water of the L&A group became turbid after 10 hours, and the pH increased to 14. While, for the S&A and C&A groups, the solid content in overflow wastewater (SCOW) fluctuated over time but could be mostly controlled in 300 ppm. The pH declined from 7 to 4 with time in the S&A group, and it was 7-8 in the C&A group. (iv) Thus, a backfill system with dewatering technology based on the C&A combination was designed. In the field application, the overflow water was recycled with the SCOW of less than 250 ppm and the pH of 7.5, while the underflow concentration was greater than 70 wt.%. The achievement provides a way to utilize the tailings containing sodium silicate effectively and environmentally, which will reduce the tailings dam on the Earth.

1. Introduction

Tailings are solid wastes generated from mineral processing. With the increasing demand of economic development for mineral resources, an astounding amount of tailings, approximately 1.2 billion tonnes per year in China, have been produced that have to be managed [1]. As a detrimental industrial waste, the improper disposal of tailings leads to some issues, such as floods, the proliferation of metal elements harmful to human health, the occupation of land, and the degradation of natural environment. In this case, the utilization of tailings for cemented tailings backfill (CTB) transported to underground has become widely used in many mines [2–4]. It has been also proven that CTB can not only reduce the cost of operation in a mine, but also provide an environmental way to treat this solid waste [5, 6]. The quality and performance of cemented tailings backfill are affected by many factors [3, 6–14], including the mass fraction. In industrial application, it is necessary to raise the mass fraction of CTB so that the setting time of the backfill can be shortened and the strength of backfill can be improved significantly [15]. In this case, tailings dewatering has become a crucial issue affecting the application of backfill technology in a mine [16]. For the requirement of continuous backfill technology, rapid dewatering by flocculation and sedimentation (FS), agglomerating the fine particles with polymeric flocculants, has been widely used in backfill mines [17–20]. Despite the rapid dewatering function, FS also plays a role in purifying the solid content in overflow wastewater (SCOW) [21], which makes it possible to recycle the overflow water and protect the environment.

Xianglushan Tungsten Mine (XTM), located in Jiangxi Province of China, is the second largest tungsten-producing mine in China, with a production capacity of 800,000 ton per year. A backfill system with a capacity of 80 m^3/h was constructed in 2011. However, many muddy foams were produced (Figure 1) on the liquid surface even after adding different flocculants, leading to high SCOW. The overflow water contained high solid that could not be recycled and then transported to the river nearby, which contaminated the environment seriously. Thus, as a result, the backfill system was banned by the local environmental protection department. In this case, tailings dewatering has been a troublesome issue for XTM to realize the backfill technology and sustainable mining. Actually, this issue occurred in other tungsten mines nearby, such as Dajishan Tungsten Mine (Jiangxi Province of China) and Pangushan Tungsten Mine (Jiangxi Province of China), which have severely restricted sustainable enterprise development.

Through surveys, it was found that in the flotation plant in these mines, a large amount of dispersants and sodium silicate (water glass) [22] are added, as shown in Table 1. Sodium silicate is a dispersant widely selected in the traditionally fatty acid flotation process of tungsten minerals [23]. It also plays an important role in the flotation of scheelite and calcite [24]. As a dispersant, sodium silicate makes the solution a kind of colloid that has adhesion stress. Then, the fine particles in the tailings slurry will form a very stable colloidal dispersion to prevent the adsorption between particles and flocculants [25, 26], which should be the key issue affecting the effect of FS.

Setting time is a key parameter for sustainable tailing operations and thereby paste backfill production. Larger underground stopes need greater filing rates for paste backfill production. Thus, chemicals that accelerate the settlement time of tailings must be chosen for nonstop backfilling. Previous researches presented effective schemes to treat mineral processing wastewater containing sodium silicate. Among them, lime is the most widely used for purifying mineral processing wastewater [27]. Additionally, as substitutes for lime, the usage of industrial by-products and cement kiln dust (CKD) was tested to treat the wastewater [28]. The chemical equation is as follows: $Na_2SiO_3 + Ca(OH)_2 = CaSiO3\downarrow + 2NaOH$. In addition, the strong acid was also selected as an agent in the treatment of mine drainage and achieved a good effect [29]. The chemical equation is as follows: $Na_2SiO_3 + 2H^+ \longrightarrow 2Na^+ + H_2SiO_3\downarrow$. However, they are both used in a concrete container with a large diameter for a static process, and the requirement of underflow concentration is about 38–45 wt.%, lower than that of 65–75 wt.% in CTB. Also, the setting time used was more than 8 hours, which could not satisfy the continuous operation of CTB. Anyway, the achievements above guide the research about treatment of sodium silicate in this paper. Furthermore, inspired by the previous outcomes, another strong electrolyte, $CaCl_2$, was taken consideration to treat the sodium silicate in this study.

Therefore, in this paper, focusing on the tailings slurry containing high sodium silicate in XTM, some laboratory experiments and semi-industrial tests were conducted. Lime, sulfuric acid, and calcium chloride were selected to remove the sodium silicate before FS with polymeric flocculant. Through evaluating the indexes, such as the qualitative settling velocity, the handling capacity, SCOW, and the underflow concentration, a feasible and reliable scheme for tailings dewatering was proposed. Finally, the industrial application of this craft has been presented and evaluated.

2. Materials and Methods

2.1. Materials

2.1.1. Tailings Slurry. In the laboratory experiments, the tailings slurry used were received from the tailings discharge outlet in XTM. The tailings slurry samples with concentrations of approximately 20 wt.% were collected every half an hour for 8 hours when the ore-dressing plant was in operation. The properties (especially the sodium silicate content) of the original tailings slurry could thus be maintained. In semi-industrial tests, the tailings slurry was directly pumped into a mixer located at the semi-industrial test site through a pipeline.

The particle size distribution and other physical properties of tailings are presented in Figure 2 and Table 2. As described in Figure 2, the particles smaller than 19 μm account for 30.40 wt.%, which makes it impossible to realize tailing dewatering by self-gravity, even if ignoring the sodium silicate [30, 31].

2.1.2. Reagents for the Treatment of Sodium Silicate (RTS). Considering the convenience and cost of obtaining the materials, lime, sulfuric acid, and calcium chloride were selected to treat the sodium silicate in this study. Lime was provided by XTM itself. The sulfuric acid and calcium chloride were manufactured by YiCheng Co., Ltd., Hunan Province of China, and their prices are 50 Yuan/L (98%) and 3000 Yuan/t, separately.

2.1.3. Polymeric Flocculant. Generally, APAM (anionic polyacrylamide) is a commonly used flocculant for tailings dewatering [32–34]. Then, after some trial tests comparing the effect of different flocculants, an APAM with a molecular weight of 18 million (manufactured by BASF SE, Germany) was selected in this paper. The price of APAM is 7000 Yuan/t.

2.2. Experimental Methods. The experiments in this study consisted of a laboratory experiment and a semi-industrial test. The laboratory experiment was a static test, and the purpose was to determine the optimum dosages of different reagents through observation of the qualitative settling velocity. Then, the semi-industrial test was aimed at verifying the effect by detecting various crucial indexes.

2.2.1. Laboratory Experiment. The laboratory experiment was divided into the following three groups: (i) adding the lime and APAM (L&A); (ii) adding the sulfuric acid and APAM (S&A); and (iii), adding the calcium chloride and

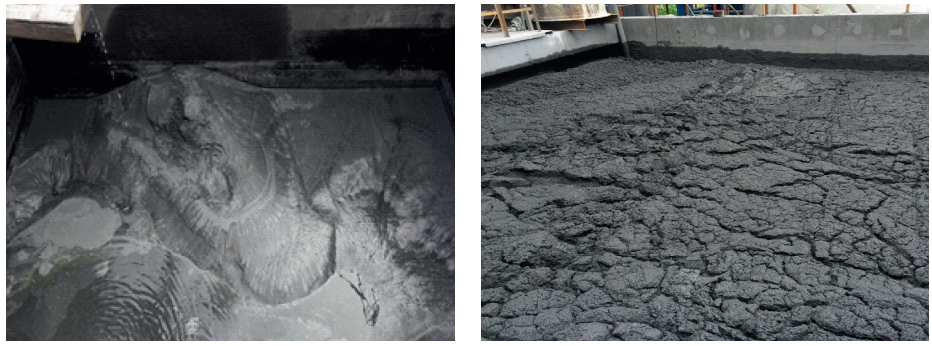

(a) (b)

Figure 1: Muddy foams on the liquid surface in XTM: (a) initial operation; (b) after 7 days.

Table 1: Sodium silicate added during the mineral process (kg per ton of original ore).

Mines	Xianglushan tungsten mine	Dajishan tungsten mine	Pangushan tungsten mine
Sodium silicate	10–15	4–6	8–12

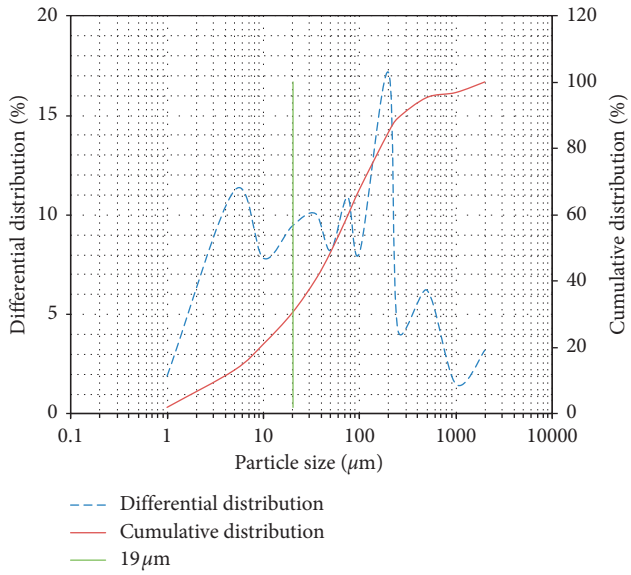

Figure 2: Particle size distribution of tailings.

APAM (C&A). The experimental method was conducted as follows:

(1) Preparation of reagents. A 10 wt.% sulfuric acid solution was prepared in 2000 mL beakers. The lime and calcium chloride were prepared and measured with an electronic scale when used.

(2) Preparation of APAM. An APAM solution of 1.0 wt. ‰ was prepared in 1000 mL measuring cylinders. Considering polyacrylamide dissolves slowly, this step was completed 0.5-1 hour ahead of the experiment.

(3) Preparation of tailing slurry. The tailings slurry selected from the ore-processing plant was mixed evenly under a lifting mixer (JJ-100W, Hongda, Hebei Province of China).

(4) Experimental progress. The tailings slurry in the lifting mixer was pumped into a 1000 mL measuring cylinder by a small peristaltic pump (BT-300EA, manufactured by Hengjie, Shanghai of China). Simultaneously, the designed RTS was added. Then, a stirrer mixed the mixture in the cylinder with a rubber mesh for 30 s after adding the APAM solution. Finally, the cylinder was placed on a table to monitor the height of the solid-liquid interface. The designed dosage of the reagents and flocculants can be observed in the results.

2.2.2. SEMI-Industrial Test

(1) Process of Semi-Industrial Test. A system of tailings dewatering based on a designed semi-industrial apparatus was constructed, as shown in Figure 3. As indicated in the figure, the tailings slurry from the ore-dressing plant of XTM was transported to a buffered mixer (XB-1000, Shicheng, Jiangxi) by self-flowing. The RTS was transported to the mixer at the same time. The RTS and APAM solutions were prepared in two flocculant preparation systems in the reagent preparation room. Then, the treated tailings slurry and APAM solution were concurrently pumped to a feed tank located at the top of a deep-cone thickener (diameter × height = 1000 mm × 8000 mm, manufactured by Feny Co. Ltd., Hunan Province of China) by a hose pump (KP 300, Jieheng, Chongqing of China).

(2) Indexes Detection. SCOW and pH. The tailings dewatering is a long-term and dynamic process in the industrial applications. Therefore, the variation of SCOW and pH with time should be considered. SCOW was detected through a vacuum filter (2BE, Zhongxing Co., Ltd., Beijing of China), as shown in Figure 4(a). According to the water recycling requirement studied in XTM before, the SCOW must be controlled to be less than 300 ppm [35]. Furthermore, the pH was detected with pH test pen.

Handling capacity. It is necessary to determine the best handling capacity first, which is a key parameter affecting the

Table 2: Physical properties of tailings in XTM.

$D < 19$ (μm)	D_{10} (μm)	D_{30} (μm)	D_{50} (μm)	D_{60} (μm)	C_u	C_c	G (g/m^3)	pH
30.40	3.89	19.58	53.32	46.12	11.86	2.14	2.99	9.0

Note: G depicts the specific gravity. C_u depicts uniformity coefficient. C_c depicts curvature coefficient.

Figure 3: Layout of the semi-industrial test.

SCOW and the design of the deep-cone thickener in industrial applications [17]. The handling capacity can be calculated through the feeding rate of tailings slurry as follows:

$$T_h = \frac{m_t}{A} = \frac{\rho Q C}{\pi r^2}, \quad (1)$$

where T_h denotes the HC, t·m^{-2}·h^{-1}; m_t is the tailings quality in a hour, t/h; ρ is the density of the tailings slurry, 1.28 t/m^3; Q denotes the feeding rate of the tailings slurry, m^3/h; C is the mass fraction of the tailings slurry, wt.%; and r depicts the radius of the deep-cone thickener, 0.5 m, so the area, A, is 0.785 m^2.

Underflow concentration. The underflow was collected and placed in a given container with certain weight and volume, as shown in Figure 4(b). After drying until the weight was stable, the weight of dry tailings was obtained. Then, the underflow concentration could be determined.

3. Results and Discussion

3.1. Static Dewatering in Laboratory Experiments

3.1.1. Effect of L&A. Figure 5 describes the height variation of the solid-liquid interface with time for different dosage combinations with lime and APAM. It can be observed from this figure that both the lime and APAM have an optimum dosage that makes the solid-liquid interface settle the fastest. As depicted in Figure 5(a), when the APAM was kept at 30 g/t, the FS shows the best effect when the additional amount of lime was 2 kg/t. Additionally, with the increase in lime consumption, the settling velocity decreased. This is because that the solubility of $Ca(OH)_2$ is not significant, and the excessive $Ca(OH)_2$ is suspended in the liquid, likely affecting the effect of FS.

In addition, when the lime was kept at 2 kg/t, an APAM addition of 30 g/t made the effect of the settling velocity of the solid-liquid interface the fastest, as shown in Figure 5(b). Previous publications have determined that the dosage of flocculants has a best value for a given material [36, 37].

The optimum combination of L&A is lime of 2 kg/t and APAM of 30 g/t. This combination was not extremely accurate but rather used as a reference for industrial application. Figure 6 presents photographs of the FS effect. Experiences indicate that excessive dosages (more than 30 g/t) of admixtures can create some problems: blockages and abrasiveness when there is a distance between thickener and backfill plant. Thus, selection of proper admixtures is vital for sustainable operations.

3.1.2. Effect of S&A. Similar to the lime, sulfuric acid is also used as a reagent to treat the sodium silicate in the tailings slurry. The chemical reaction is as follows: $Na_2SiO_3 + H_2SO_4 = Na_2SO_4 + H_2SiO_3\downarrow$.

The relative molecular masses of $Ca(OH)_2$ and H_2SO_4 are 74 and 98, respectively; thus, according to the optimum dosage of lime at 2 kg/t, the sulfuric acid consumption in this study was kept as $2\,\text{kg/t} \times (98/74) \approx 2.6\,\text{kg/t}$.

Figure 7(a) depicts the height variation of the solid-liquid interface with time when the addition of sulfuric acid was 2.6 kg/t and the APAM changed from 10 g/t to 40 g/t. This figure indicates that when the dosage of APAM is 20 g/t, the settling velocity presents the best effect. Then, with the increase of APAM, the settling trend variation is not obvious and even lower. The best combination of S&A is sulfuric acid of 2.6 kg/t and APAM of 20 g/t, approximately. In this case, the experimental photograph is shown in Figure 7(b).

3.1.3. Effect of C&A. Likewise, the relative molecular mass of $CaCl_2$ is 110; thus, the calcium chloride consumption was 3 kg/t. Additionally, in this case, Figure 8(a) shows the height variation of the solid-liquid interface with time when the addition of calcium chloride was 3 kg/t and the APAM changed from 10 g/t to 40 g/t. It can be concluded that the best combination is approximately calcium chloride of 3 kg/t and APAM of 30 g/t. Figure 8(b) presents the effect at this combination.

(a) (b)

Figure 4: Detection of (a) SCOW and (b) underflow concentration.

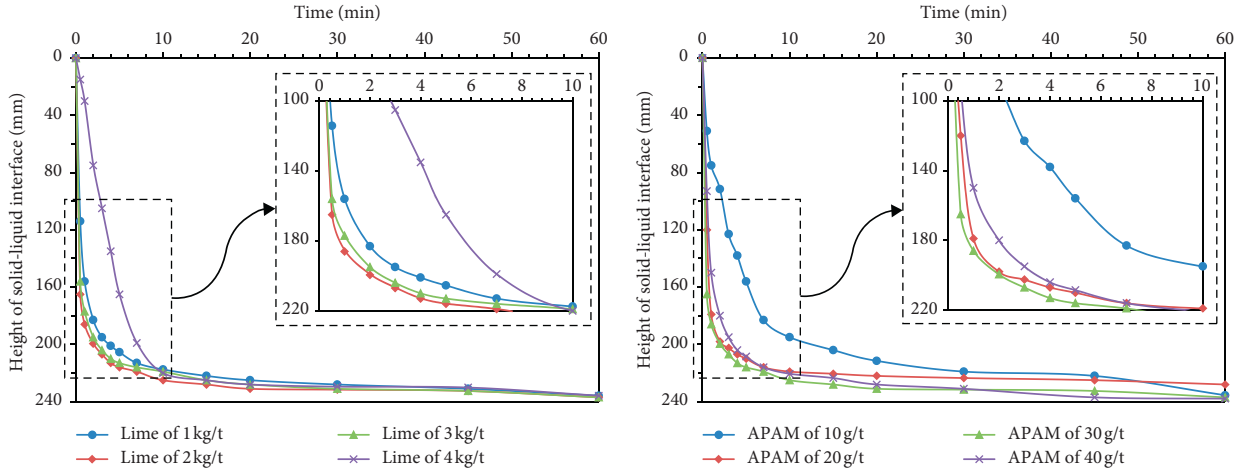

(a) (b)

Figure 5: Height variation of the solid-liquid interface with time (a) when the dosage of APAM was 30 g/t and the addition of lime changed from 1 kg/t to 4 kg/t; (b) when the addition of lime was 2 kg/t and the APAM changed from 10 g/t to 40 g/t.

3.2. Dynamic Dewatering in the Semi-Industrial Test

3.2.1. Best Handling Capacity (BHC). The reagent dosage was kept consistent with the results of the laboratory experiments, while the feeding rate of tailings slurry was changed from 1.6 m^3/h to 2.6 m^3/h to detect the SCOW variation. That is, the handling capacity changed from 0.39 $t \cdot m^{-2} \cdot h^{-1}$ to 0.64 $t\, m^{-2} \cdot h^{-1}$. This process lasted for only one hour. Figure 9 describes the variation of SCOW with varying handling capacity. This figure indicates that the SCOW increases with the handling capacity. According to the water recycling requirements, the SCOW must be controlled to be less than 300 ppm. In this case, it was concluded that the BHC values of L&A, S&A, and C&A groups were 0.54 $t \cdot m^{-2} \cdot h^{-1}$, 0.49 $t \cdot m^{-2} \cdot h^{-1}$, and 0.59 $t \cdot m^{-2} \cdot h^{-1}$, respectively. It is obvious that the S&A group presented the worst handling capacity in FS. As we know, unlike $CaSiO_3$, H_2SiO_3 is a flocculant precipitate in the water, which may more or less affect the adsorption between tailings and flocculants [38, 39].

3.2.2. Variation of SCOW and pH with Time. Figure 10 comprehensively depicts the change of SCOW and pH with time under the determined reagents dosages and BHC. Figure 11 presents the FS effect of different combinations on the liquid surface after 10 hours. Analysing these figures, the following conclusions are suggested:

(1) For the L&A group, the SCOW increased gradually with time. After 10 hours of continuous operation, the detected SCOW increased beyond the criterion higher than 300 ppm. And, many muddy foams gathered on the liquid surface at this time, as Figure 11(a) shows. In addition, the pH varied from 11 to 14, which meant that the

(a) (b)

Figure 6: Photographs of (a) sample without adding lime and (b) sample with lime of 2 kg/t and APAM of 30 g/t.

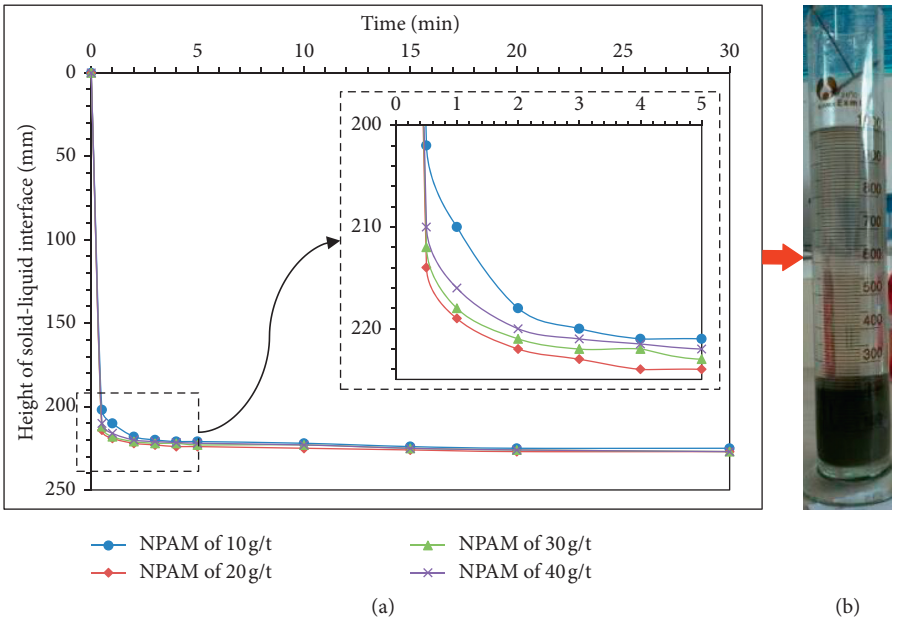

(a) (b)

Figure 7: (a) Height variation of the solid-liquid interface with time when the addition of sulfuric acid was 2.6 kg/t and the APAM changed from 10 g/t to 40 g/t; (b) experimental effect at sulfuric acid of 2.6 kg/t and APAM of 20 g/t.

overflow water was strongly alkaline because OH^- was produced after adding lime. In this alkaline environment, some of the remaining foaming agent and foam stabilizer used for flotation would produce stable foams [40]. These foams adsorbed some tailings particles to affect the FS effect and increase the SCOW. Stable muddy foams would also affect the thickener underflow and thereby the behaviour of cemented backfill produced from these tailings

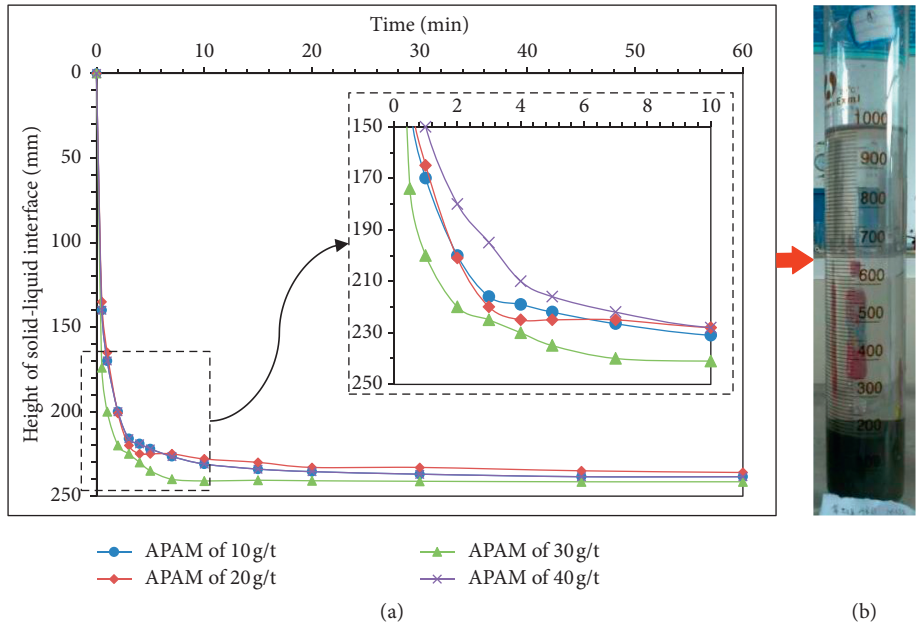

Figure 8: (a) Height variation of solid-liquid interface with time when the addition of calcium chloride was 3 kg/t and the APAM changed from 10 g/t to 40 g/t; (b) the effect of FS at calcium chloride of 3 kg/t and APAM of 30 g/t.

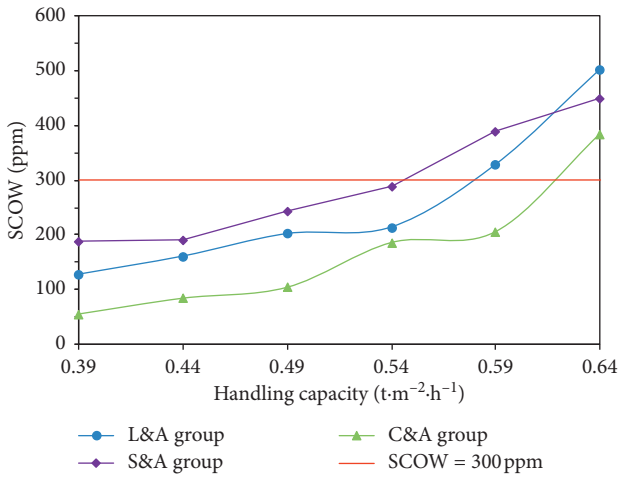

Figure 9: Variation of SCOW with varying handling capacity under the different reagent combinations.

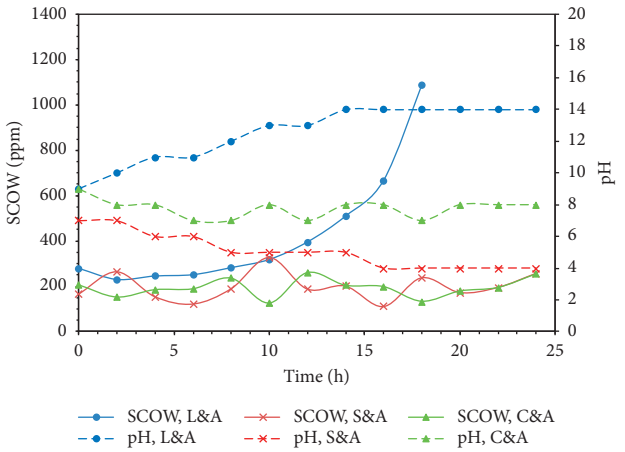

Figure 10: Variation of SCOW of different combinations with varying time.

(2) For the S&A and C&A groups, the SCOW fluctuated over time but was mostly controlled at 300 ppm. Furthermore, the pH declined from 7 to 4 with time in the S&A group, while the pH remained at 7-8 in the C&A group. It can be observed from Figures 11(b) and 11(c) that the overflow in these groups showed high clarity. However, the low pH in the S&A group required anticorrosion treatment for devices and a neutralization system for pH. These additions will increase both the initial investment and operating cost.

3.2.3. Variation of Underflow Concentration with Time. Figure 12 describes the underflow concentration variation for different combinations with time. It can be observed that the underflow concentration increased with time and remained mostly higher than 70 wt.% after 10 or 12 hours for the S&A group and C&A group, except for a trend of decline in the C&A group after 12 hours. Actually, the final concentration of tailings mainly depends on its own characteristics and the parameters of the deep-cone thickener [41, 42] regarding waste of time. However, in the continuous CTB backfill, the rapid dewatering is required to ensure the high underflow concentration in a limited time. As studied above, the effect became worse after 10 hours, which then affects the settling velocity and, as a result, the underflow concentration dropped.

3.2.4. Selection of Dewatering Scheme. Table 3 compares the effect of different combinations on FS. It is obvious that the cost of the C&A group is the most expensive. However, the

(a) (b) (c)

Figure 11: FS effect of different combinations on the liquid surface in the small deep-cone thickener after operating for 10 hours: (a) L&A group, (b) S&A group, and (c) C&A group.

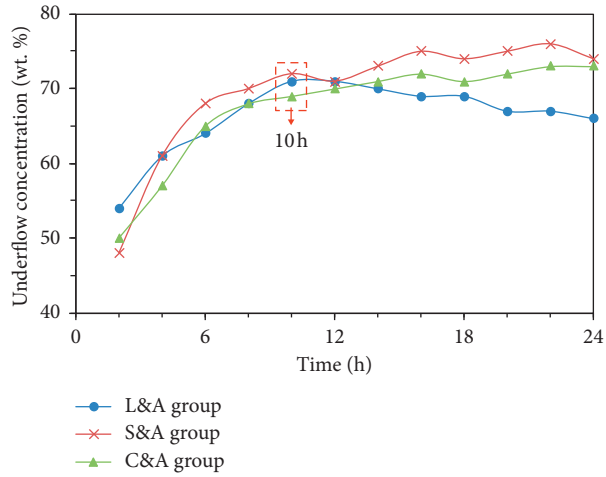

Figure 12: Variation of underflow concentration of different combinations with time.

other combinations require equipment to remove the foams or neutralize the pH of the overflow water. Specially, the acid environment in the S&A group is potentially harmful to people and requires devices to be treated for corrosion. These additional crafts will increase the cost more than the higher dosage cost in the C&A group. Complex craft leads to increased difficulty in operation and control. In addition, the BSU of the C&A group is maximal, which will reduce the diameter of the deep-cone thickener. Synthetically, the C&A group was selected in XTM.

3.3. Industrial Evaluation. Figure 13 depicts the backfill setup with new dewatering technology based on the results of this research. The tailings with the concentration of 20 wt.% from ore-dressing plant are pumped to a laminar mixer (CLHYQ-8, manufactured by Huaxing, Pingdingshan of China) with the calcium chloride solution. Then, the treated tailings slurry is transported to a deep-cone thickener (NGT-18, manufactured by Feny, Hunan of China) while the APAM solution is added. Next, a shear pump (60NJ-485, manufactured by Tianmen, Hubei of China) is used to pump the tailings with a concentration of 70 wt.% to a mixer (XB-2000, Shicheng, Jiangxi). The cemented paste will be formed in combination with the tailings, cement, and water (if needed). Finally, the paste is pumped to a stope underground, and the overflow water is stored in a recycling reservoir.

Figure 14presents the overflow water and underflow concentration in the field application. The figure indicates that the overflow water showed good clarity. Actually, the SCOW detected in the field could be controlled at approximately 250 ppm, while the underflow concentration maintained a concentration higher than 70 wt.% and often reached a highest value of 73 wt.%. In addition, the overflow water has been recycled in the ore-processing craft successfully, which shows an economic and environmental effect.

Table 3: Comparison of different dewatering schemes.

No	Items	L&A	S&A	C&A
1	Dosage of reagents			
1.1	Lime (kg/t)	2		
1.2	H_2SO_4 (kg/t)		2.6	
1.3	$CaCl_2$ (kg/t)			3
1.4	APAM (g/t)	30		30 g/t
1.5	NAPAM (g/t)		20	
2	Reagent cost (US $/t)	0.27	0.31	0.39
2	BHC (t/(m^2·h))	0.54	0.49	0.59
3	SCOW (ppm) in 24 hours	>300, after 10 hours	<300	<300
4	pH after 24 hours of operation	14	4	8
5	Underflow concentration	<70 wt.% after 12 hours	>70 wt.%	>70 wt.%
6	Additional devices			
6.1	Defoaming device	2 (one for spare)		
6.2	Neutralization system for pH	2 (one for spare)	2 (one for spare)	
6.3	Anticorrosion treatment		1	

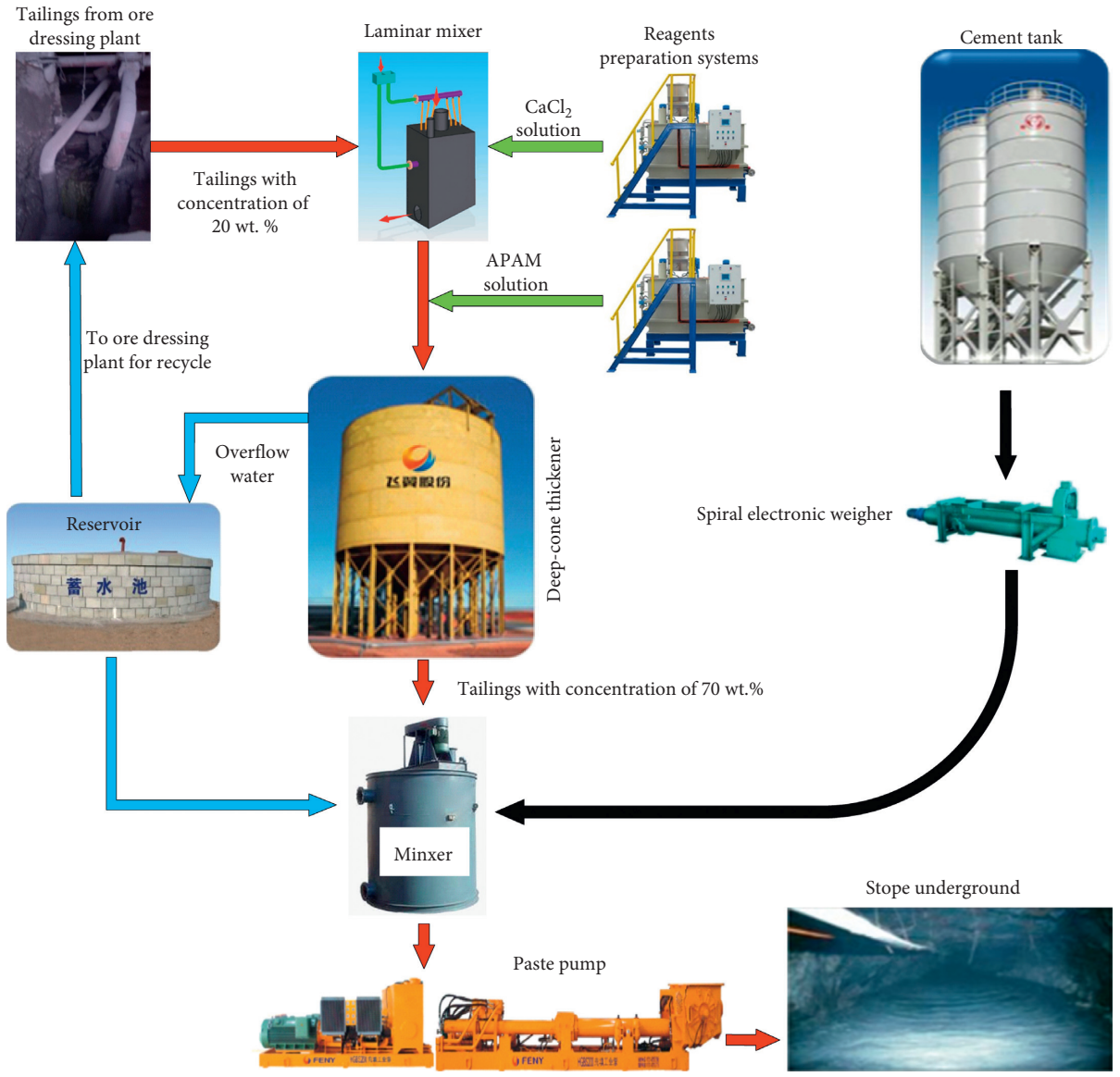

Figure 13: Backfill setup with new FS technology in XTM.

(a) (b)

Figure 14: Overflow water (a) and underflow tailings (b) in the field application.

4. Conclusions

This study conducted laboratory experiments and semi-industrial tests for dewatering the tailings containing high sodium silicate (water glass). In addition, the industrial application was also evaluated. Based on the results, the following conclusions are obtained.

(1) Lime, sulfuric acid, and calcium chloride showed a good FS effect in the laboratory experiments when combined with APAM.

(2) The selected BHC values of the L&A, S&A, and C&A groups were $0.54\,t{\cdot}m^{-2}{\cdot}h^{-1}$, $0.49\,t{\cdot}m^{-2}{\cdot}h^{-1}$, and $0.59\,t{\cdot}m^{-2}{\cdot}h^{-1}$, respectively.

(3) In the semi-industrial tests, the overflow water of the L&A group became turbid after 10 hours, and the pH increased to 14. For the S&A and C&A groups, the SCOW fluctuated over time but could be mostly controlled at 300 ppm. In addition, the pH declined from 7 to 4 with time in the S&A group, while the pH was 7-8 in the C&A group.

(4) The C&A group (calcium chloride and APAM) was selected in the field. The backfill craft with new FS technology based on the result was designed and operated. It presented a good effect with an SCOW of less than 250 ppm and an underflow concentration of greater than 70 wt.%. The achievement of this paper provides a way to utilize the tailings effectively and environmentally, which will also reduce the tailings dam on the Earth. It needs to be note that, however, the FS with two steps is too complicated in engineering application. A new technology with one reagent should be thus studied in the future.

Data Availability

The photograph data used to support the findings of this study are all included within the article.

Conflicts of Interest

The authors declare that there are no conflicts of interest regarding the publication of this paper.

Acknowledgments

This study was financially supported by the State Key Laboratory of Safety and Health for Metal Mines (2017-JSKSSYS-03 and 2019-JSKSSYS-02) and the Research Project of Education Department of Hunan Province(17C1375).

References

[1] X. Song, J. B. Pettersen, K. B. Pedersen, and S. Røberg, "Comparative life cycle assessment of tailings management and energy scenarios for a copper ore mine: a case study in northern Norway," *Journal of Cleaner Production*, vol. 164, 2017.

[2] A. Wu, Y. Wang, H. Wang, S. Yin, and X. Miao, "Coupled effects of cement type and water quality on the properties of cemented paste backfill," *International Journal of Mineral Processing*, vol. 143, pp. 65–71, 2015.

[3] Y. He, Q. Chen, C. Qi, Q. Zhang, and C. Xiao, "Lithium slag and fly ash-based binder for cemented fine tailings backfill," *Journal of Environmental Management*, vol. 248, p. 109282, 2019.

[4] Q.-S. Chen, Q.-L. Zhang, A. Fourie, X. Chen, and C.-C. Qi, "Experimental investigation on the strength characteristics of cement paste backfill in a similar stope model and its mechanism," *Construction and Building Materials*, vol. 154, pp. 34–43, 2017.

[5] Q. Chen, Q. Zhang, A. Fourie, and C. Xin, "Utilization of phosphogypsum and phosphate tailings for cemented paste backfill," *Journal of Environmental Management*, vol. 201, pp. 19–27, 2017.

[6] Y. Feng, Q. Yang, Q. S. Chen et al., "Characterization and evaluation of the pozzolanic activity of granulated copper slag modified with CaO," *Journal of Cleaner Production*, vol. 232, pp. 1112–1120, 2019.

[7] S. Cao, E. Yilmaz, and W. Song, "Evaluation of viscosity, strength and microstructural properties of cemented tailings backfill," *Minerals*, vol. 8, no. 8, p. 352, 2018.

[8] S. Cao, E. Yilmaz, and W. Song, "Dynamic response of cement-tailings matrix composites under SHPB compression load," *Construction and Building Materials*, vol. 186, pp. 892–903, 2018.

[9] S. Cao, E. Yilmaz, G. Xue, and W. Song, "Assessment of acoustic emission and triaxial mechanical properties of rock-cemented tailings matrix composites," *Advances in Materials Science and Engineering*, vol. 2019, Article ID 6742392, 12 pages, 2019.

[10] H. Jiang, H. Yi, E. Yilmaz, S. Liu, and J. Qiu, "Ultrasonic evaluation of strength properties of cemented paste backfill: effects of mineral admixture and curing temperature," *Ultrasonics*, vol. 100, Article ID 105983, 2020.

[11] H. Jiao, Y. Wu, X. Chen, and Y. Yang, "Flexural toughness of basalt fibre-reinforced shotcrete and industrial-scale testing," *Advances in Materials Science and Engineering*, vol. 2019, Article ID 6568057, 8 pages, 2019.

[12] H.-z. Jiao, S.-f. Wang, A.-x. Wu, H.-m. Shen, and J.-d. Wang, "Cementitious property of $NaAlO_2$-activated Ge slag as cement supplement," *International Journal of Minerals, Metallurgy and Materials*, vol. 26, no. 12, pp. 1594–1603, 2019.

[13] C. Qi, Q. Chen, X. Dong, Q. Zhang, and Z. Yaseen, "Pressure drops of fresh cemented paste backfills through coupled test loop experiments and machine learning techniques," *Powder Technology*, vol. 361, pp. 748–758, 2019.

[14] Z. Su, Q. Chen, Q. Zhang, and D. Zhang, "Recycling lead-zinc tailings for cemented paste backfill and stabilisation of excessive metal," *Minerals*, vol. 9, no. 11, p. 710, 2019.

[15] X. Wang, J. Liu, Q. Chen, C. Xiao, and X. Wan, "Optimal flocculating sedimentation parameters of unclassified tailings slurry," *Journal of Engineering Science and Technology Review*, vol. 32, no. 17, pp. 23–28, 2014.

[16] S. Li, X.-M. Wang, and Q.-L. Zhang, "Dynamic experiments on flocculation and sedimentation of argillized ultrafine tailings using fly-ash-based magnetic coagulant," *Transactions of Nonferrous Metals Society of China*, vol. 26, no. 7, pp. 1975–1984, 2016.

[17] S. Li and X.-M. Wang, "Fly-ash-based magnetic coagulant for rapid sedimentation of electronegative slimes and ultrafine tailings," *Powder Technology*, vol. 303, pp. 20–26, 2016.

[18] W. Ge, H. Li, Y. Ren, F. Zhao, and S. Song, "Flocculation of pyrite fines in aqueous suspensions with corn starch to eliminate mechanical entrainment in flotation," *Minerals*, vol. 5, no. 4, pp. 654–664, 2015.

[19] T. Su, T. J. Chen, Y. M. Zhang, and P. W. Hu, "Selective flocculation enhanced magnetic separation of ultrafine disseminated magnetite ores," *Minerals*, vol. 6, no. 3, 2016.

[20] Y. Liu, Q. Zhang, Q. Chen et al., "Utilisation of water-washing pre-treated phosphogypsum for cemented paste backfill," *Minerals*, vol. 9, no. 3, p. 175, 2019.

[21] Q. S. Chen, Q. L. Zhang, X. M. Wang, C. C. Xiao, and D. Xu, "Experimntal study on effect of magnetized water on flocculating sedimentation of unclassied tailings," *Journal of Central South University*, vol. 46, no. 11, pp. 4256–4261, 2015.

[22] Z. Gao, D. Bai, W. Sun, X. Cao, and Y. Hu, "Selective flotation of scheelite from calcite and fluorite using a collector mixture," *Minerals Engineering*, vol. 72, pp. 23–26, 2015.

[23] H. Han, Y. Hu, W. Sun et al., "Fatty acid flotation versus BHA flotation of tungsten minerals and their performance in flotation practice," *International Journal of Mineral Processing*, vol. 159, pp. 22–29, 2017.

[24] J. Wang, Z. Gao, Y. Gao, Y. Hu, and W. Sun, "Flotation separation of scheelite from calcite using mixed cationic/anionic collectors," *Minerals Engineering*, vol. 98, pp. 261–263, 2016.

[25] J. Bratby, "Coagulation and flocculation," *Water and Wastewater Treatment*, pp. 71–77, Taylor Support Services, Melbourne, Australia, 2nd edition, 2006.

[26] S. Ahuja, *Comprehensive Water Quality and Purification*, Academic Press, Cambridge, MA, USA, 2014.

[27] Y. M. Wang, *Treatment of the Mineral Separation Wastewater by Lime-Flocculant Sedimentation*, Hunan Nonferrous Metals, Zhuzhou, China, 2005.

[28] A. L. Mackie and M. E. Walsh, "Bench-scale study of active mine water treatment using cement kiln dust (CKD) as a neutralization agent," *Water Research*, vol. 46, no. 2, pp. 327–334, 2012.

[29] J. Kang, C. Chen, W. Sun et al., "A significant improvement of scheelite recovery using recycled flotation wastewater treated by hydrometallurgical waste acid," *Journal of Cleaner Production*, vol. 151, pp. 419–426, 2017.

[30] A. Fourie, *Electrokinetic Dewatering of Ultrafine Coal and Coal Tailings*, Australian Centre for Geomechanics, Perth, Australia, 2008.

[31] Y. Feng, Q. Chen, Y. Zhou et al., "Modification of glass structure via CaO addition in granulated copper slag to enhance its pozzolanic activity," *Construction and Building Materials*, vol. 240, p. 117970, 2020.

[32] X. Z. Shi, H. U. Hai-Yan, D. U. Xiang-Hong, L. I. Mao-Lin, and H. Y. Wang, "Experimental study on flocculating sedimentation of tailings slurry in a vertical sand tank," *Mining & Metallurgical Engineering*, vol. 27, no. 3, pp. 1–11, 2010.

[33] H. Z. Jiao, A. X. Wu, H. J. Wang, X. H. Liu, S. K. Yang, and Y. T. Xiao, "Experiment study on the focculation settlement characteristic of unclassified tailings," *Journal of University of Science & Technology*, vol. 33, no. 12, pp. 1437–1441, 2011.

[34] S. Wang, Q. L. Zhang, X. M. Wang, and L. I. Shuai, "Optimal calculation mode of vertical sand silo area based on flocculating sedimentation," *Journal of Northeastern University Natural Science*, vol. 37, no. 10, 2016.

[35] H. Jiao, S. Wang, Y. Yang, and X. Chen, "Water recovery improvement by shearing of gravity-thickened tailings for cemented paste backfill," *Journal of Cleaner Production*, vol. 245, Article ID 118882, 2019.

[36] L. Besra, D. K. Sengupta, S. K. Roy, and P. Ay, "Influence of polymer adsorption and conformation on flocculation and dewatering of kaolin suspension," *Separation and Purification Technology*, vol. 37, no. 3, pp. 231–246, 2004.

[37] J. H. Zhe, W. H. Jiang, W. A. Xiang, J. X. Wen, and Y. Q. Wen, "Beijing. Rule and mechanism of flocculation sedimentation of unclassified tailings," *Journal of University of Science & Technology Beijing*, vol. 32, no. 6, pp. 702–707, 2010.

[38] J. Hirsch and E. H. Ahrens Jr., "The separation of complex lipide mixtures by the use of silicic acid chromatography," *Journal of Biological Chemistry*, vol. 233, pp. 311–320, 1958.

[39] V. Lenher, "Silicic acid," *Journal of the American Chemical Society*, vol. 43, no. 3, pp. 391–396, 2002.

[40] D. L. Lord, A. H. Demond, and K. F. Hayes, "Effects of organic base chemistry on interfacial tension, wettability, and capillary pressure in multiphase subsurface waste systems," *Transport of porous media*, vol. 38, no. 1–2, pp. 79–92, 2000.

[41] H. Fang, "Study on limiting concentration of non-uniform particle flow," *International Journal of Sediment Research*, vol. 1, no. 11, pp. 83–88, 1996.

[42] H. Jiao, A. Wu, H. Wang, S. Zhong, R. Ruan, and S. Yin, "The solids concentration distribution in the deep cone thickener: a pilot scale test," *Korean Journal of Chemical Engineering*, vol. 30, no. 2, pp. 262–268, 2013.

[43] D. Wang, Q. Zhang, Q. Chen, C. Qi, Y. Feng, and Xiao, "Temperature variation characteristics in flocculation settlement of tailings and its mechanism," *International Journal of Minerals, Metallurgy and Materials*, vol. 28, no. 3, pp. 1–6, 2020.

Hindawi
Advances in Materials Science and Engineering
Volume 2020, Article ID 7421769, 14 pages
https://doi.org/10.1155/2020/7421769

Research Article

Effects of Corn Stalk Fly Ash (CSFA) on the Mechanical and Deformation Properties of Cemented Coal Gangue Backfill

Tingye Qi[1,2], **Haochen Wang**[1,2], **Guorui Feng**[1,2], **Xianjie Du**[1,2], **Zehua Wang**[1,2] **and Shufeng Zhang**[1,2]

[1]*College of Mining Engineering, Taiyuan University of Technology, Taiyuan, China*
[2]*Shanxi Province Research Centre of Green Mining Engineering Technology, Taiyuan, China*

Correspondence should be addressed to Guorui Feng; fgr09000@126.com

Received 17 October 2019; Accepted 17 January 2020; Published 11 February 2020

Guest Editor: Qiusong Chen

To reduce the amount of cement used in cemented coal gangue backfill (CCGB, a mixture of coal gangue, cement, fly ash, and water), mechanical and deformation properties of CCGB in which CSFA partially replaces the cement (0, 10, 20, 30, and 40 wt%) were studied. Compressive strength, acoustic emission during uniaxial loading, shear strength, and drying shrinkage were analysed. The compressive strength, shear strength, and drying shrinkage tests were performed at different curing times. The results showed that cemented coal gangue and corn stalk fly ash backfill (CGCAB) presented better performance, and the CGCAB with a 20% substitution rate had the best performance at day 28. Despite having the largest drying shrinkage value, 20% is the best choice for the substitution rate of CSFA. A 20% CSFA addition can enhance the bearing capacity of CGCAB and improve its failure mode, which is of great significance to support the upper overburden load and maintain the surface stability of the goaf.

1. Introduction

Backfilling mining is widely used to address surface subsidence caused by extensive mining, environmental pollution caused by coal gangue accumulation, and low coal recovery rate under buildings/railways/water-bodies [1, 2]. Cemented coal gangue backfill (CCGB) can be used to support overburden and prevent surface subsidence upon transportation through a pipeline to underground goaf [3–5]. CCGB can reuse solid waste and reduce landfill area, thus addressing environmental problems [6]. The CCGB for coal mine backfilling is an engineered mixture of coal gangue, fly ash, cement, and water; and the solids account for 75–85 wt% [7, 8]. In recent years, many scholars have conducted research on CCGB. Wu et al. [9] developed a coupling model to analyse the thermal-hydraulic-mechanical-chemical processes that occurred in CCGB. Yin et al. [10] proposed an electrochemical treatment to improve the early age strength and deformation characteristics of CCGB. Sun et al. [11] developed a test machine to test the creep disturbance effect of CCGB and established a creep disturbance constitutive model of CCGB. However, CCGB still presents many practical issues such as insufficient materials [12], excessive cost [13], and low strength [14].

To solve the above problems, the introduction of corn stalk fly ash (CSFA) in the preparation of CCGB has been proposed. On one hand, corn is the main crop in China, and its yearly corn stalk production is significantly large [15, 16]. Moreover, corn stalks are transported to biomass power plants, and large amounts of CSFA are produced every year. On the other hand, CSFA has a certain pozzolanic activity and a large content of silica [17, 18]. If CSFA was introduced for use in the CCGB, it could reduce costs as partial cement replacement and address the high CSFA production. However, a few studies investigated the CSFA content influencing the physical, mechanical properties and micromechanism of CCGB and other cement-based materials.

The other biomass ashes, such as rice husk ash, have been studied as partial cement replacement in concrete [19]. In general, rice husk ash presents pozzolanic activity, and the incorporation of rice husk ash into concrete can improve its

mechanical properties, such as compressive strength and splitting tensile strength. Givi et al. [20] replaced cement by agro-waste rice husk ash at different proportions (5, 10, 15, and 20 wt%) and using two different average particle sizes (5 and 95 μm). According to the authors, cement can be replaced by up to 15% of the rice husk ash of 95 μm and 20% of the 5 μm ones for increased strength. The optimal strength of concrete was obtained when 5 μm particles replaced 10% of the cement. Raisi et al. [21] replaced cement with different proportions (5, 10, 15, and 20 wt%) of rice husk ash and prepared a control group using 100% cement. The compressive strength, splitting tensile strength, and elastic modulus of the concrete increased relative to the control group for 5 and 10% substitution at 28 days. Moreover, the group with a substitute content of 5% showed the maximum compressive strength, close to 50 MPa, at 28 days. This result was mainly attributed to the pozzolanic activity and physical filling ability peculiar to rice husk ash [22, 23].

The explanation for rice husk ash improving the strength of concrete is that rice hush ash can react with calcium hydroxide formed by cement hydration to form a dense structure of C-S-H gel, which makes the internal pores of concrete more compact. As the calcium ion concentration continues to decrease, the degree of cement hydration is again enhanced. In addition, the particle size of rice husk ash is also essential to enable the physical filling ability. Furthermore, the structure of rice husk ash particles determines that they can be used as a porous medium to store water [24]. In the early stages of cement hydration, rice husk ash particles absorb free water into their pores. At the later stage, the rice husk ash particles gradually release the internally stored water, which further develops the cement hydration process. However, some research scholars have concluded that the addition of rice husk ash to concrete reduces its compressive strength. This behaviour happens due to specific operations in the preparation of the concrete mixture which differ from the conventional operations. For example, Ismail and Waliuddin [25] adjusted the water-cement ratio to maintain the consistency of workability. Thus, the compressive strength decreased. Olutoge and Adesina [26] used high-early-strength Portland limestone cement and missed the pozzolanic reaction stage of rice husk ash. Therefore, the compressive strength was not effectively improved. Based on similar material compositions and engineering backgrounds, the direction of concrete provides good references for CCGB.

In this study, the cement in CCGB was replaced by CSFA at 0, 10, 20, 30, and 40 wt%, and the effects of substitution rates on the mechanical and deformation properties of cemented coal gangue and corn stalk fly ash backfill (CGCAB) were investigated. Upon analysing the test results, the optimal substitution rate for CGCAB mechanical and deformation performance was selected. The compressive strength, shear strength, and drying shrinkage tests were performed at different curing times. The acoustic emission detection was performed at day 28 under uniaxial loading conditions.

2. Materials and Methods

2.1. Raw Materials. The coal gangue used in the tests was obtained from the Tunlan coal mine, Taiyuan City, Shanxi Province. After being crushed, it was divided into fine aggregate (particle diameter smaller than 5 mm) and coarse aggregate (particle diameter of 5–15 mm). The cement used in the tests was ordinary Portland cement with a strength grade of 42.5, from Taiyuan Lionhead Cement Co., Ltd., Taiyuan City, Shanxi Province. The fly ash used was Class F and Class II fly ash from Hebei Woyang Mineral Products Trading Co., Ltd., Shijiazhuang City, Hebei Province. The CSFA used in the tests is from a power plant in Shijiazhuang City, Hebei Province. To reduce the impact of water content on the test results, the CSFA was first spread out and dried in an oven at 80°C for 24°h. Scanning electron microscopy (SEM) images of fly ash and CSFA are shown in Figure 1. The fly ash particles are in the form of glass beads, and the CSFA particles are irregular in shape and are mostly elongated. The main chemical composition and physical properties of various solid raw materials are shown in Table 1. The particle size distributions of CSFA and fly ash are shown in Figure 2, and the gradation of coal gangue determined in previous study [27] is shown in Table 2.

2.2. Specimen Preparation. As shown in Table 3, a control group (C0) and four variable groups (C1, C2, C3, and C4) were established. In all five groups, the amount of fine coal gangue was 285 kg/m^3, the amount of coarse coal gangue was 665 kg/m^3, and the amount of fly ash was 380 kg/m^3. The amount of cement in the control group (C0) was 190 kg/m^3, and, in the variable groups, CSFA replaced 10wt% (C1), 20wt% (C2), 30wt% (C3), and 40wt% (C4) of cement, respectively. For all mixtures, the mass concentration and water-binder ratio were kept constant at 83% and 0.55, respectively.

Following the Chinese standard GB/T 50080–2016 "Standard for test method of performance on ordinary fresh concrete," the raw materials were mixed and stirred; then the mixtures were immediately poured into three types of cubic moulds: 100 mm × 100 mm × 100 mm (for compressive strength test and acoustic emission test), 70 mm × 70 mm × 70 mm (for shear strength test), and 100 mm × 100 mm × 515 mm (for drying shrinkage test). The fresh specimens were compacted using a vibrating table and then were covered with plastic sheets to prevent water loss. After 24 h, the specimens were removed from the moulds and placed in the curing room (temperature: 20 ± 2°C; humidity: 40 ± 5%) until the stable age. Before the start of each test, the surfaces of all test specimens were sanded with sandpaper.

2.3. Test Methods. The tests in this study were performed with three specimens each, and the final values were average values. The compressive strength test was performed in accordance with the Chinese standard GB/T 50081–2002 "Standard for test method of mechanical properties on ordinary concrete." This test was performed within 3, 7, 14,

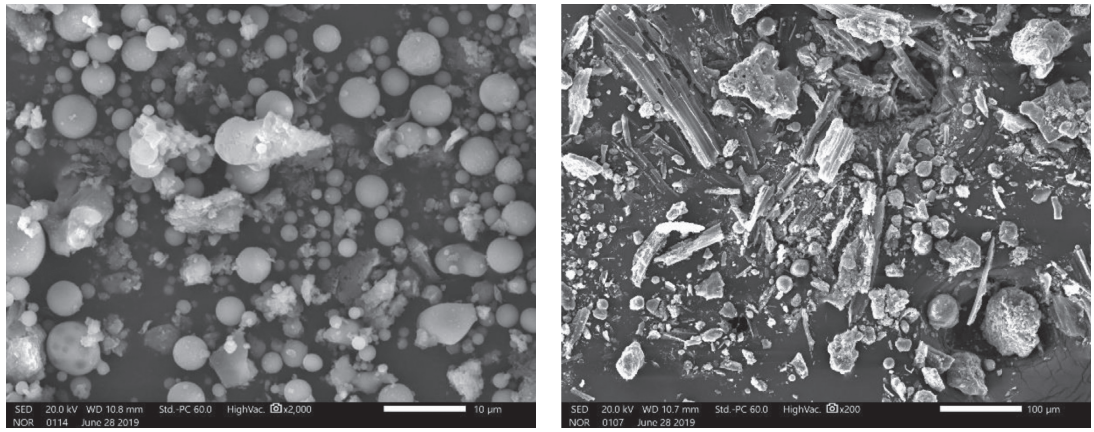

(a) (b)

Figure 1: SEM images of supplementary cementitious materials: (a) fly ash and (b) corn stalk fly ash.

Table 1: Main chemical composition and physical properties of various solid raw materials.

	Coal gangue	Cement	Fly ash	CSFA
SiO_2	28.46%	22.27%	52.42%	35.68%
Al_2O_3	12.11%	5.59%	32.48%	6.10%
Fe_2O_3	14.86%	3.47%	3.62%	7.40%
CaO	7.15%	65.90%	3.05%	9.98%
MgO	3.50%	0.81%	1.01%	2.60%
True density (g/cm^3)	2.31	3.10	2.09	2.13
Specific surface (m^2/kg)	—	349	415	222
Moisture content (%)	8.0	—	0.12	3.77

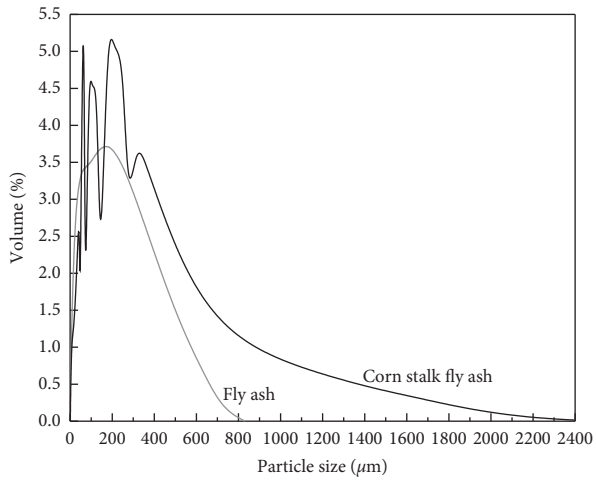

Figure 2: Particle size distribution of corn stalk fly ash and fly ash.

and 28 days after pouring. The pressure testing machine used a computer-controlled WDW-100 electronic universal testing machine with a full-scale specification of 100 kN, which can meet the failure load of the specimen to the fullest within 20–80% of the full scale of the press. For the compressive strength test, the loading rate was controlled at a displacement of 0.3 mm/min.

To grasp the failure characteristics of CGCAB under uniaxial loading conditions, acoustic emission test was used

Table 2: Gradation of coal gangue [27].

Sieve size (mm)	Percent passing (%)
0.15	7.97
0.3	10.93
0.6	16.49
1.18	22.65
2.36	26.29
4.75	38.85
9.5	67.11
16	100

for detection. The acoustic emission test under uniaxial loading conditions was performed within 28 days after pouring. The acoustic emission device adopted the DS5-8B acoustic emission device (Beijing Softland Times Scientific & Technology Co., Ltd.), with a preamplifier gain of 40 dB, a signal threshold of 40 dB, a sampling frequency of 25 kHz, a conversion accuracy of 16 bit, and a sampling rate of 5 million samples per channel. There were four signal receiving probes, which were arranged alternately on each side.

The shear strength test was performed in accordance with the Chinese standard DZ/T 0276.25–2015 "Regulation for testing the physical and mechanical properties of rock" (Part 25: Test for determining the shear strength of rock). The shear strength test was performed in the same day in comparison to the compressive strength test for the same mix proportion of the test specimens under the same curing age. The shear strength was measured through a wedge shear test, and the pressure testing machine used was the same as the one used for the compressive strength test. During the shear strength test, the selected angles of the shearing fixtures were 40°, 45°, 50°, and 55°. For the shear strength test, the loading rate was controlled at a displacement of 0.8 mm/min.

The drying shrinkage test was performed in accordance with the Chinese standard GB/T 50082–2009 "Standard for test methods of long-term performance and durability of ordinary concrete." For the drying shrinkage test, the specimens were removed and placed on the concrete

Table 3: Mix proportions (kg/m^3) of coal gangue backfilling materials.

Specimen	Substitution rate (wt%)	Fine gangue (0–5 mm)	Coarse gangue (5–15 mm)	Cement	Fly ash	CSFA	Water
C0	0	285	665	190	380	0	311.325
C1	10	285	665	171	380	19	311.325
C2	20	285	665	152	380	38	311.325
C3	30	285	665	133	380	57	311.325
C4	40	285	665	114	380	76	311.325

shrinkage meter after 3 days of curing. This test was performed at 1, 3, 7, 14, 28, 45, 60, 90, 120, and 180 days after curing. A concrete shrinkage meter (measuring gauge: 540 mm) and digital dial gauge (accuracy: 0.001 mm) were used.

3. Results and Discussion

3.1. Compressive Strength. The compressive strength of CGCAB at different ages and substitution rates is given in Figure 3. At day 3, the compressive strength showed a tendency to gradually decrease, and group C0 presented the highest compressive strength (2.4 MPa). At days 7 and 14, the compressive strength first increased and then decreased, and group C1 presented the highest compressive strengths (4.38 MPa and 6.25 MPa for days 7 and 14, respectively). At day 28, the compressive strength also first increased and then decreased. However, group C2 presented the highest compressive strength (9.69 MPa).

CSFA contains a large amount of oxides, such as silica and alumina, and it presents a certain pozzolanic activity. Thus, when CSFA is in contact with the calcium hydroxide formed by the hydration reaction of cement, a pozzolanic reaction occurs and calcium silicate hydrate (C-S-H) is formed [28]. C-S-H has an amorphous colloidal form with a dense structure that assists the increase of the pressure bearing capacity of CGCAB, thereby increasing its compressive strength. At early stages, the pozzolanic reaction has not yet entered the active stage. Therefore, if the substitution rate increases, the cement content decreases, and the compressive strength gradually decreases. When the curing time increases, especially at 28 days, the pozzolanic reaction gradually becomes effective. The CSFA addresses the absence of cementitious material and the compressive strength of CGCAB rapidly increases [29], which is especially clear when the substitution rate is 20%. For larger substitution rates, the water demand of CSFA causes the workability of CGCAB to decrease, thereby hindering the hydration and pozzolanic reactions, which cause the compressive strength to decrease [30, 31].

3.2. Acoustic Emission. It can be seen from Figure 4 that the strain corresponding to the stress peak is maintained within 0.02-0.03. When the substitution rate was 20%, the ring-down counts were the highest, which may be attributed to the increased production of C-S-H colloids with surface roughness and wrinkles [32, 33]. These colloids generate more transient elastic waves or stress waves by friction during uniaxial loading. The sources of acoustic

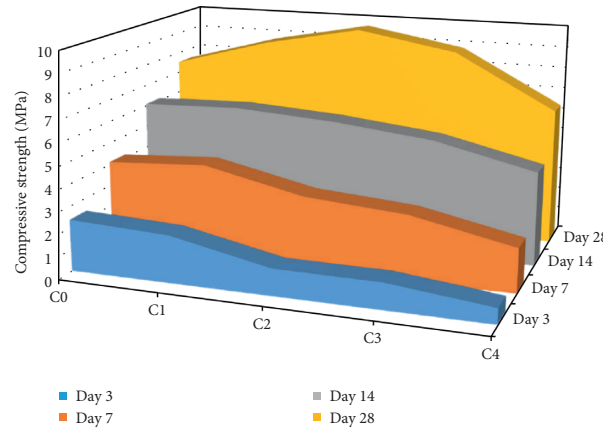

Figure 3: Trend of CGCAB compressive strength.

emissions inside the CGCAB include the friction between aggregate particles and the generation and expansion of cracks. Furthermore, the peak of the ring-down count generally occurred before the stress peak (after the yield point) and was in the unstable fracture development stage of CGCAB. These characteristics are established because the crack rapidly expands over a large area and the small fragments slid extensively during the specimen instability [34].

Figure 4 shows the schematic diagrams of the acoustic emission points in the uniaxial loading process which correspond to the final point of each stress-strain curve at day 28 and different substitution rates. The greater the compressive strength, the greater the number of acoustic emission fracture points. For groups C0 and C4, the relatively few fracture points are mostly concentrated on the diagonal face of the CGCAB cube specimen. For groups C1, C2, and C3, many fracture points are concentrated on the central column of the CGCAB cube specimen. Moreover, the failure mode of CGCAB is similar to that of concrete, and two opposite pyramid-shaped fracture surfaces are formed [35, 36]. We observed that the CGCAB law of failure mode was not the same as the concrete one, but it was similar to that of soft rock. These results may be attributed to the hardness of CGCAB, which is closer to soft rock and softer than concrete. The failure mode is a single slope for softer materials and an X-shaped conjugate slope for harder materials [37].

When the substitution rate was 0% or 40%, the hydration and pozzolanic reactions were relatively incomplete at day 28. Moreover, the CGCAB specimens were in a soft state. Thus, their failure mode was closer to a monoclinal fracture (Figures 4(a) and 4(e)). Such CGCAB specimens lose less

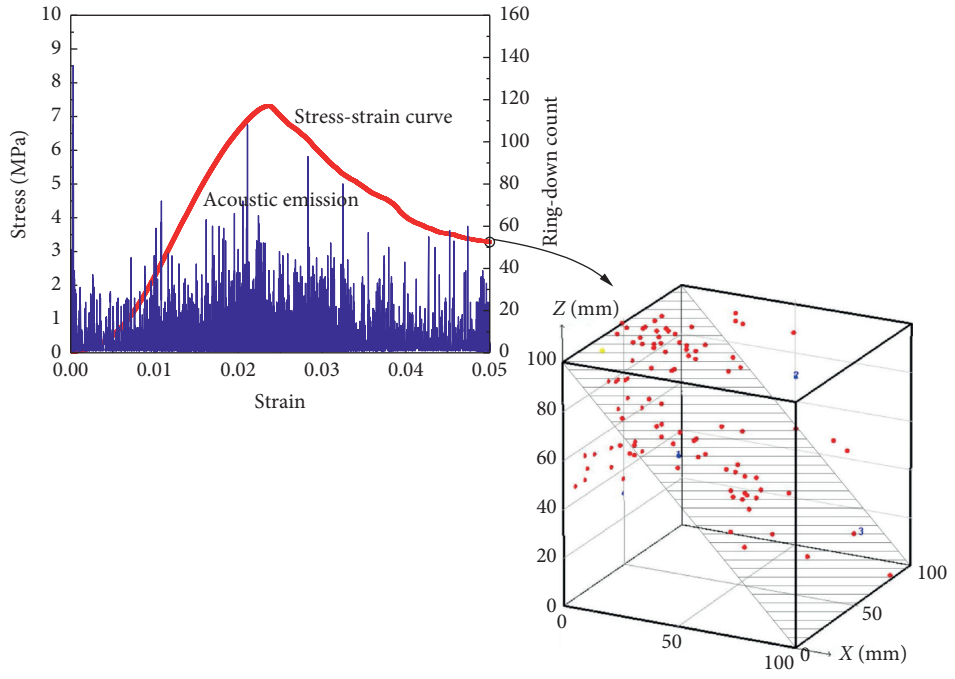

(a)

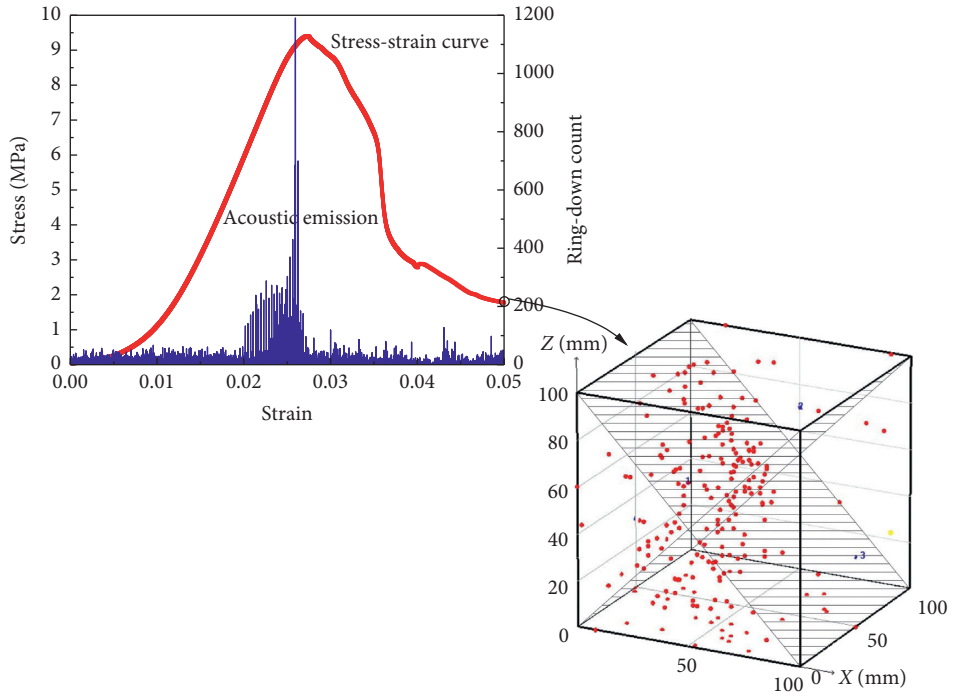

(b)

Figure 4: Continued.

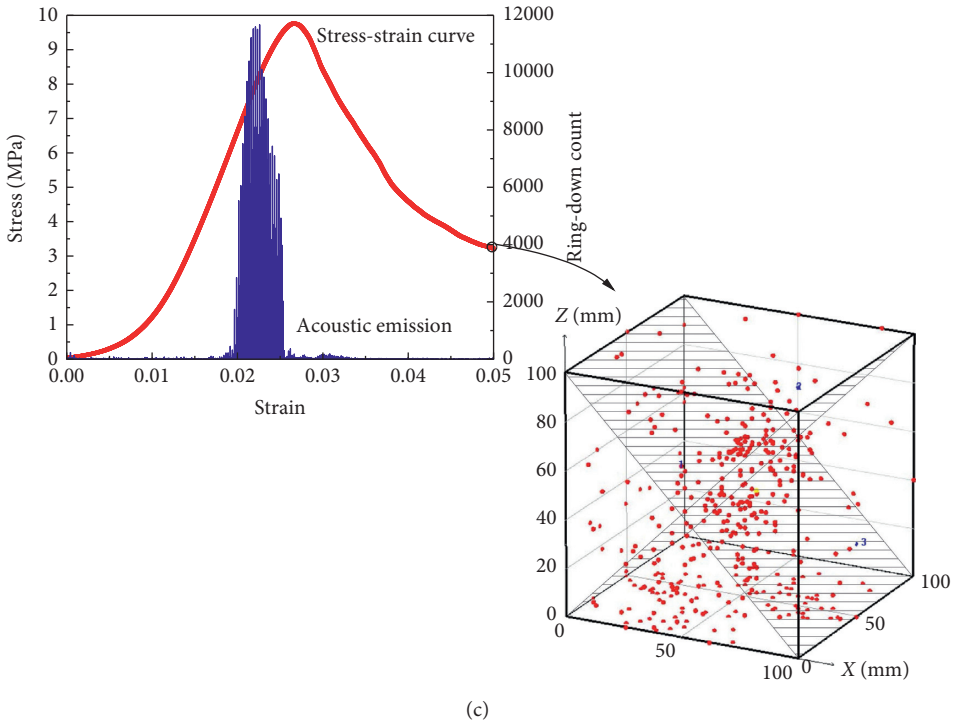

(c)

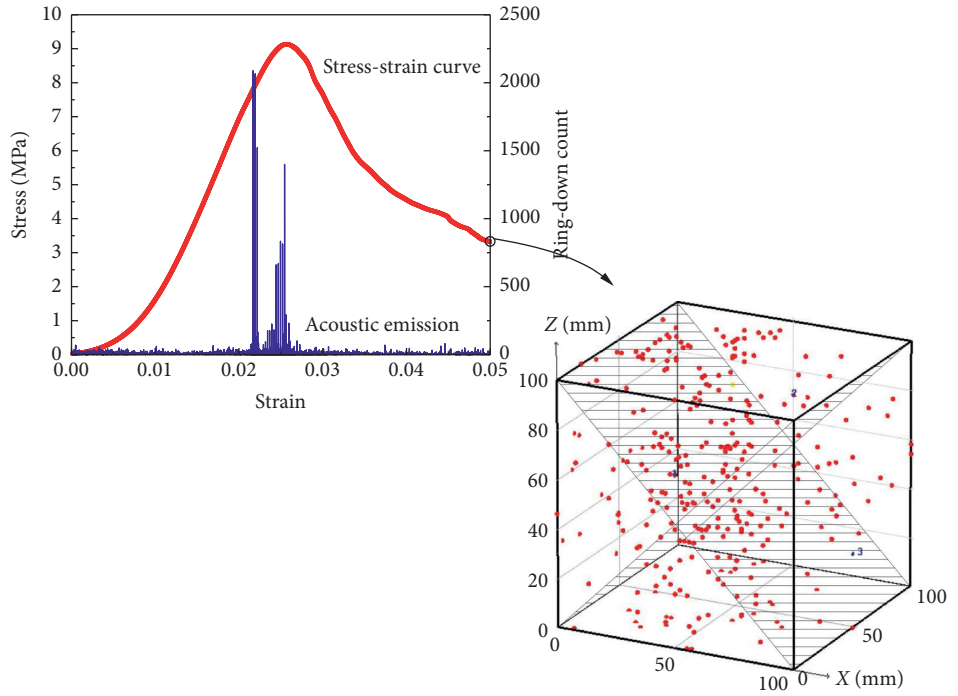

(d)

Figure 4: Continued.

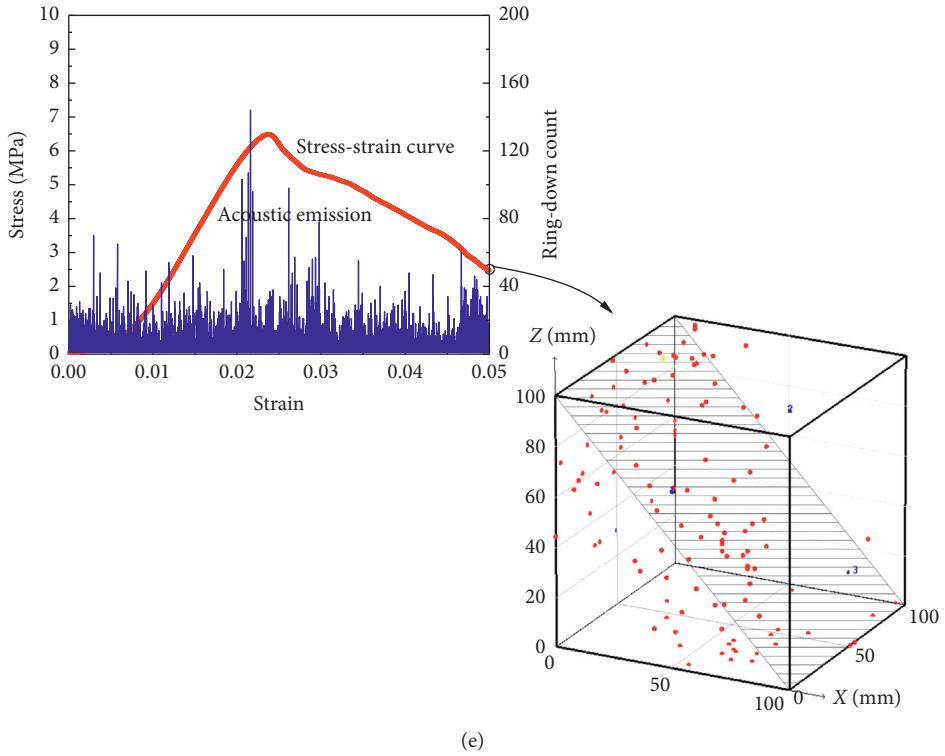

Figure 4: Stress-strain-acoustic emission ring-down count and fracture points during uniaxial loading at day 28 with different substitution rates: (a) 0% (C0), (b) 10% (C1), (c) 20% (C2), (d) 30% (C3), and (e) 40% (C4).

energy due to cracking during uniaxial loading than hard specimens for a moderate substitution rate of 10–30%. This conclusion can be confirmed in Figure 5. For group C2, the total amount of energy released by the CGCAB specimen detected by the acoustic emission device was the largest. The final accumulated energy was arranged from highest to lowest in the following order: C2, C3, C1, C0, and C4. At different substitution rates, the energy released during the pore closure stage and reversible elastic deformation stage slightly changed. The stage that causes the accumulated energy to rise sharply is the unstable fracture development stage (yield stage). For 20% or 30% substitution rate, the unstable fracture clearly develops, and the accumulated energy rises sharply. Under other substitution rates, the fracture development is relatively stable, and the accumulated energy rises steadily.

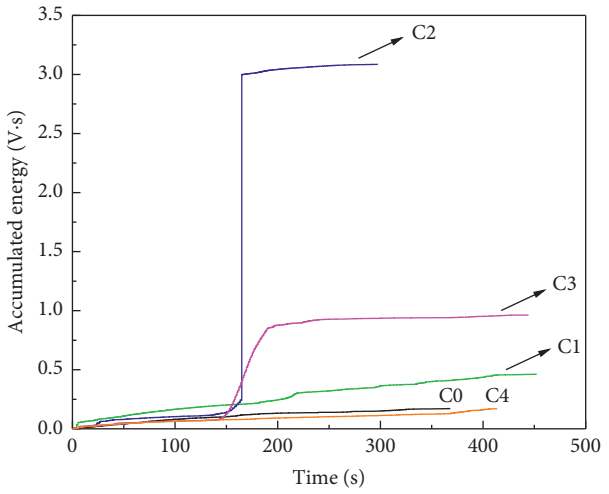

Figure 5: Correlation between accumulated energy and loading time at day 28.

3.3. Shear Strength. Considering the analysis of rock, soil, and concrete against shear strength, the Mohr-Coulomb criterion (equation 1) can be used to analyse the shear resistance of CGCAB [38–40].

$$\tau = \sigma \tan \phi + c, \quad (1)$$

where τ is the shear stress on the shear fracture surface (i.e., the shear strength of CGCAB), MPa; σ is the normal stress, MPa; φ is the internal friction angle, °; and c is cohesion, MPa.

The axial stress combined with the angle of the shearing fixture is decomposed into normal stress and shear stress (i.e., shear strength). The relationship between the shear strength of different shear angles (40°, 45°, 50°, and 55°) and the substitution rate under the same curing age is shown in Figure 6. At day 3, the shear strength showed a tendency to gradually decrease, and group C0 presented the highest shear strength. At days 7, 14, and 28, the shear strength first increased and then decreased. However, the corresponding substitution rate for the group with the highest shear strength was not the same. At day 7, the corresponding group with the highest shear strength was C1 for the four

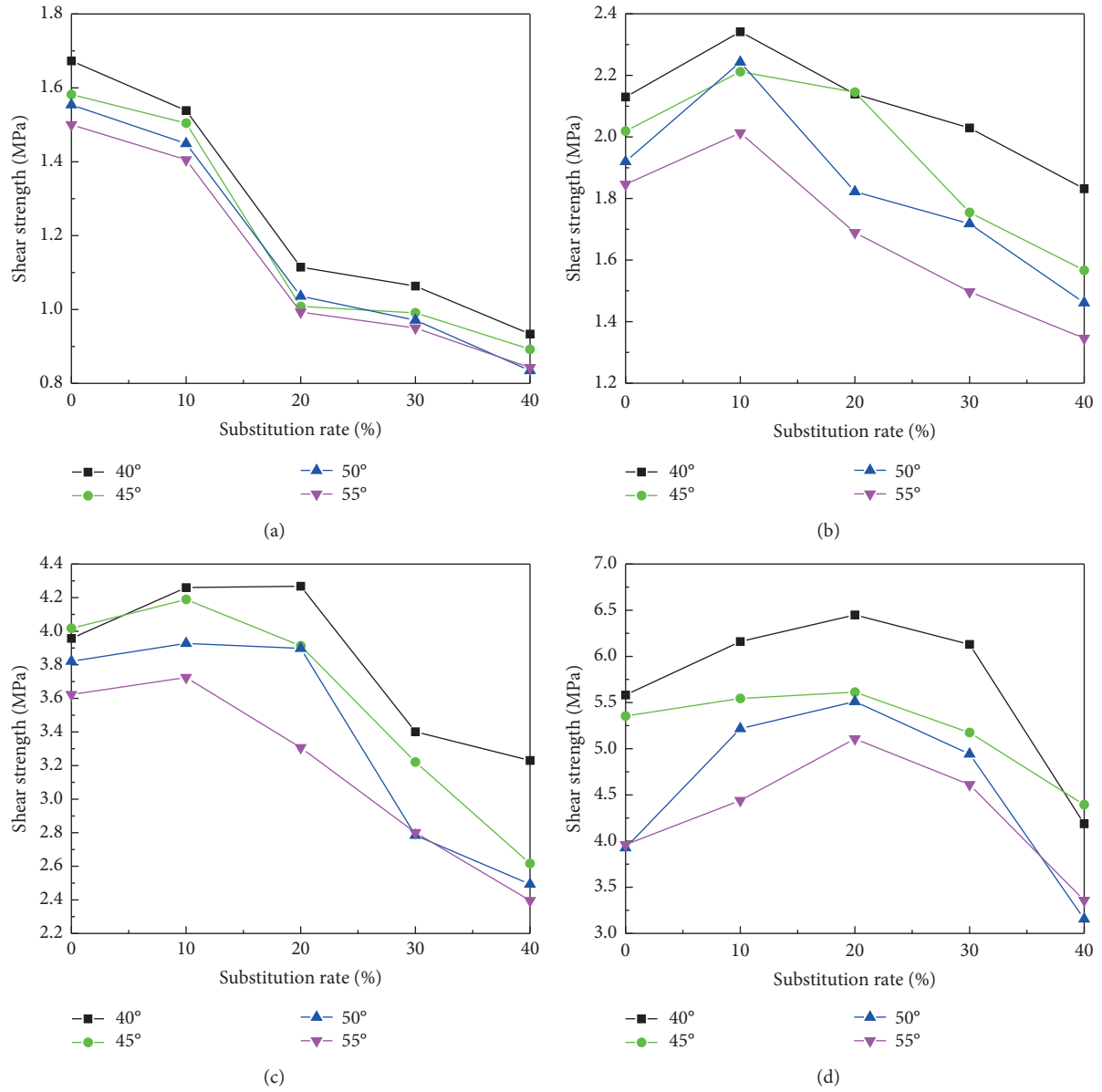

Figure 6: Correlation between shear strength and substitution rate at (a) 3, (b) 7, (c) 14, and (d) 28 days of curing age.

shear angles. At day 14, they were C1 for 45°, 50°, or 55° shear angle and C2 for 40° shear angle. At day 28, it was C2 for all four shear angles. The optimal substitution rate gradually changed from 10% to 20% with increasing curing time, which is consistent with the compressive strength results. This behaviour occurs because the internal mechanism of shear strength change is almost the same as the one of compressive strength. It was also observed that, at the same curing age and substitution rate, the shear strength decreases as the shear angle increases. Thus, the higher the shear angle, the higher the portion of axial stress decomposed into normal stress, the lower the portion decomposed into the shear stress, and the smaller the shear strength.

To further explore the relationship between substitution rate and parameters in the shear strength formula (i.e., the Mohr-Coulomb criterion), the Mohr circle for uniaxial loading was plotted, as shown in Figure 7. The abscissa of the right intersection of the Mohr circle and the horizontal axis is the maximum principal stress value. A similar result (difference of approximately 1 MPa) was obtained for the maximum principal stress on the drawn Mohr circle with compressive strength. This indicates that the Mohr-Coulomb criterion is suitable for evaluating the mechanical properties of CGCAB. For uniaxial loading, the radius represents half of the maximum principal stress in the Mohr circle. At day 3, the radius of the Mohr circle showed a decreasing trend with increasing substitution rate, and the radius of the Mohr circle for group C0 was the largest. At days 7 and 14, the radius of the Mohr circle first increased and then decreased with an increasing substitution rate. The radius of the Mohr circle for group C1 was

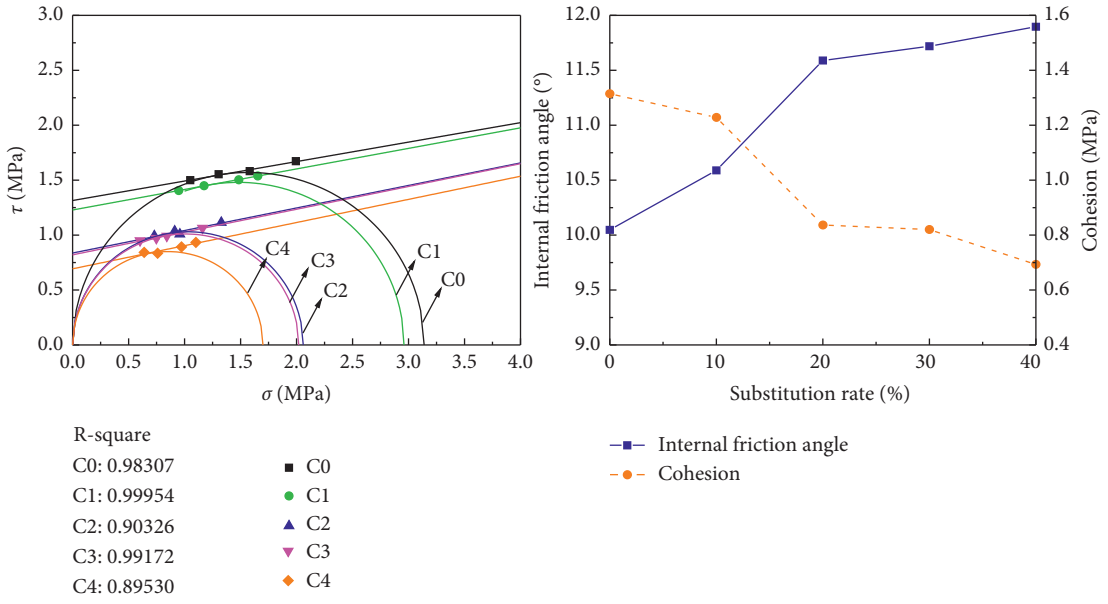

(a)

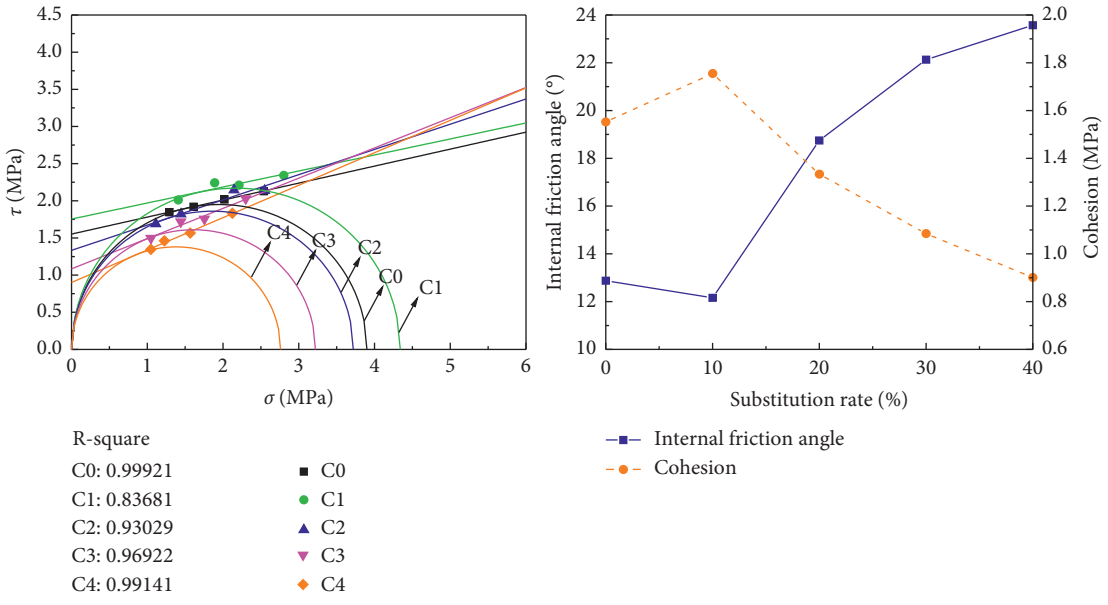

(b)

Figure 7: Continued.

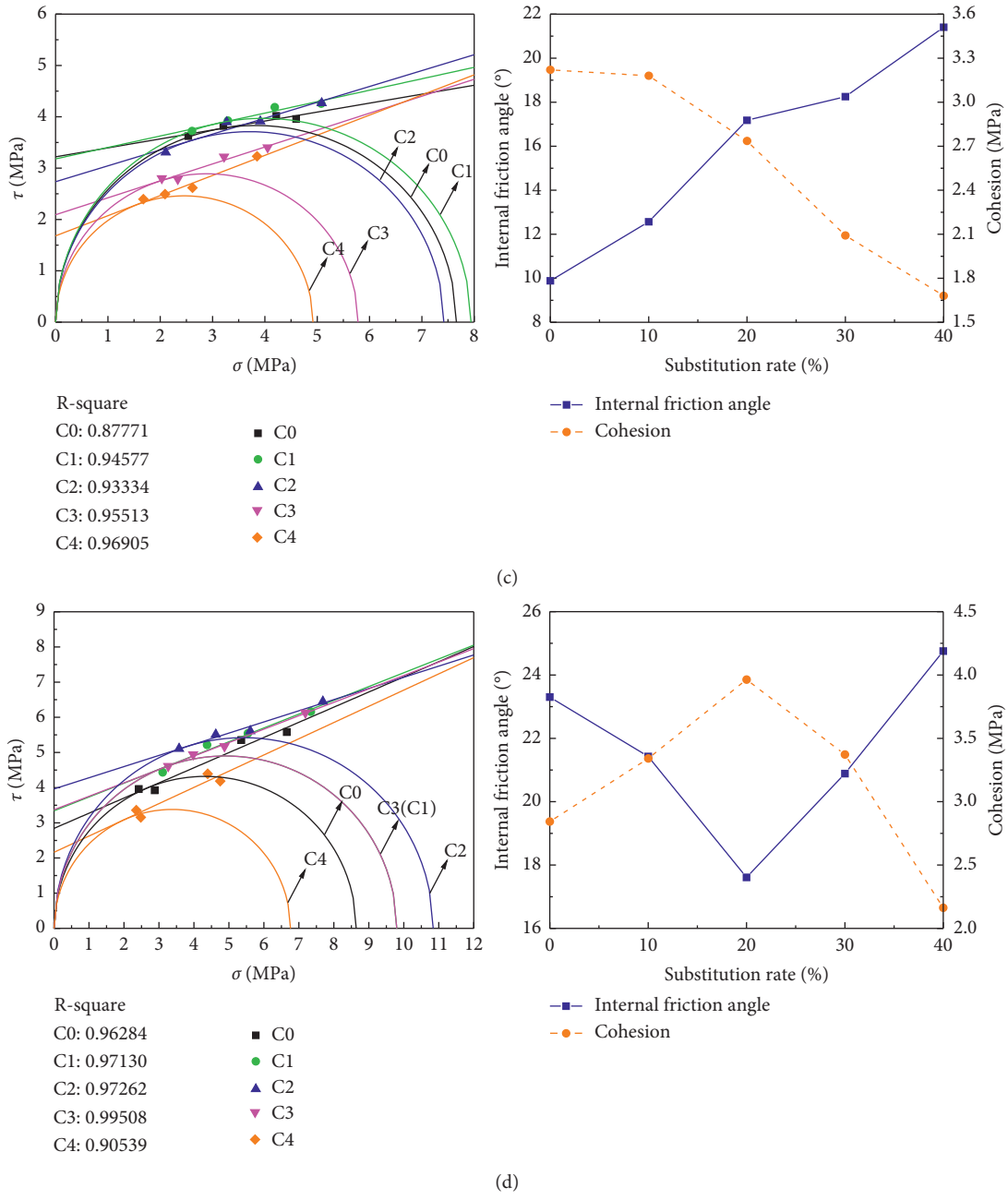

Figure 7: Mohr circles and CGCAB parameters at (a) 3, (b) 7, (c) 14, and (d) 28 days of curing age.

the largest. At day 28, the radius of the Mohr circle also presented an increasing trend first and then a decreasing trend upon increasing substitution rate. The radius of the Mohr circle was the largest for group C2. In addition, the relative positions of the various Mohr circles demonstrate that group C2's catch-up momentum is the strongest from medium to large, followed by group C3's. The remaining Mohr circles did not catch up with other Mohr circles but developed stepwise with age.

The tangent line of the Mohr circle is a linear envelope, known as the Mohr-Coulomb failure criterion. Its slope represents the tangent value of the internal friction angle, and its intercept represents the cohesion. These two important parameters correspond to the friction and cohesive strengths, respectively [41]. Figure 7 shows the internal friction angle and cohesion of CGCAB of various ages as functions of the substitution rate. At days 3 and 14, the internal friction angle gradually increased with increasing substitution rate, and the internal friction angles for group C4 were the largest (11.9° and 21.4° for days 3 and 14, respectively). In contrast, cohesion gradually decreased with increasing substitution rate, and the cohesion values for group C0 were the largest (1.3 MPa and 3.2 MPa for days 3 and 14, respectively). At day 7, the internal friction angle first decreased and then increased with increasing substitution rate. The internal friction angle for group C4 was still

the largest (23.6°). The cohesion first increased and then decreased with increasing substitution rate, and the cohesion for group C1 was the largest (1.8 MPa). At day 28, the trends of internal friction angle and cohesion were the same as the ones from day 7. The internal friction angle for group C4 was still the largest (24.8°), but the largest cohesion was observed for group C2 (4 MPa).

Comparing Figures 3 and 7, it is clear that the greater the compressive strength, the smaller the internal friction angle and the greater the cohesion for identical substitution rate compared to different substitution rates. This behaviour may happen because, after the pozzolanic reaction, the coal gangue is wrapped into a regular ellipsoid. Thus, the friction strength of the specimen is easily reduced with increasing substitution rate, whereas the cementation force increases with increasing C-S-H content, so that the cohesive strength of the specimen also increases with the increasing substitution rate. However, with the gradual increase of substitution rate, the change in workability hinders the maintenance of the pozzolanic reaction. Thus, the internal friction angle increases and the cohesion decreases. According to the acoustic emission fracture points (Figure 4), failure is mainly attributed to the shear of specimen, and the axial stress is transformed into normal and shear stress on the surface of the shear fracture. In the loading of CGCAB, both shearing and compression are possible, but it is not possible to consider only one of them.

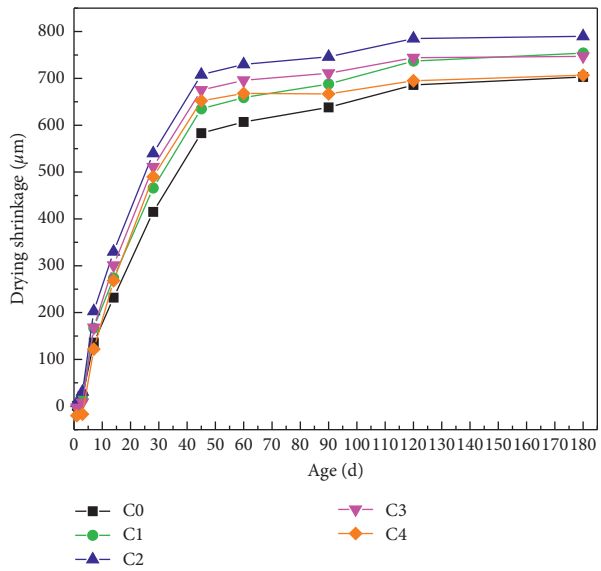

Figure 8: CGCAB drying shrinkage trend.

3.4. Drying Shrinkage. The drying shrinkage performance of CGCAB is related to an important quality index in the backfilling mining process: the rate of supporting pit roof. The larger the drying shrinkage is, the smaller the rate of supporting pit roof is and the more difficult it is for the CGCAB to meet the roof of the roadway during the actual backfilling process. Consequently, ground collapse is more likely to occur. The drying shrinkage of CGCAB at different ages (days 1, 3, 7, 14, 28, 45, 60, 90, 120, and 180) with different substitution rates is shown in Figure 8. It can be seen that the drying shrinkage increases with extended age due to the loss of water inside the specimen [42]. This loss can be attributed to the evaporation of internal water and the consumption of water by chemical reactions [43].

CGCAB specimens under natural dry conditions shrank faster from days 3 to 7 in this study. Thus, the chemical reaction rate was the fastest in that period, which was the key stage for strength development. For group C2, CGCAB presented the largest drying shrinkage after 3 days. For 20% substitution rate, the hydration and pozzolanic reactions in the CGCAB are thoroughly performed, so they consume the most water and produce the most C-S-H colloids. When the substitution rate is too small or too large, these reactions are inhibited by the shortage of CSFA or free water. Thus, less water is consumed, and the drying shrinkage is lower than when the substitution rate was 20%. In addition, it can be seen that, at 180 days, the drying shrinkages of C0 and C4 groups are almost equal, while C1 and C3 groups are also close. This indicates that the addition of CSFA can accelerate the completion of drying shrinkage. This may be related to the porous nature and coarse morphology of the CSFA particles.

3.5. Microscopic Analysis. To corroborate the mechanism analyses of the above subsections and ensure that they can be tested by practice, SEM images of CGCAB under different substitution rates at day 28 were obtained. As shown in Figure 9, C-S-H is produced in a fibrillar morphology [44]. The highest C-S-H production was observed for group C2. When CSFA was not added, C-S-H was distributed in a relatively dispersed form among the individual particles. For 20% CSFA, C-S-H was clearly concentrated in a large agglomerate shape and acted as a bridge connection between the particles. For 40% CSFA, the concentration of C-S-H was significantly weakened, and many particles were not covered by C-S-H. This behaviour likely occurred because their pozzolanic activity could not be exerted in a water-deficient environment. Moreover, for low cement content, the amount of calcium hydroxide formed by cement hydration was relatively small, and the degree of pozzolanic reaction was relatively low. Consequently, the reaction product formed was relatively small. Microscopic analysis establishes a similar relationship to mechanical properties. There is a positive correlation between mechanical strength and C-S-H content. With the increase of C-S-H content, the CGCAB is denser, and the compressive strength, acoustic emission energy, and shear strength are generally higher. These SEM images further confirm that 20% is the best substitution rate for CSFA to replace cement in CGCAB.

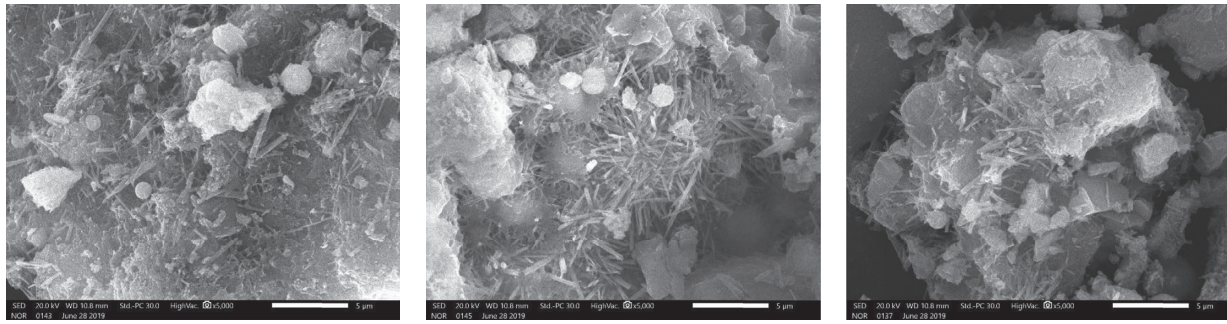

(a) (b) (c)

Figure 9: SEM images of CGCAB at day 28 and (a) 0% (C0), (b) 20% (C2), and (c) 40% (C4) substitution rates.

4. Conclusion

In this study, the cement in CCGB was replaced by CSFA at 0, 10, 20, 30, and 40 wt%, and the effects on the mechanical and deformation properties of CGCAB, including compressive strength, shear strength, stress-strain-acoustic emission, and drying shrinkage, were analysed. The compressive and shear strength tests were performed at the curing age of 3, 7, 14, and 28 days. The acoustic emission test was performed only for day 28. The drying shrinkage test was performed at days 1, 3, 7, 14, 28, 45, 60, 90, 120, and 180. The main conclusions are summarized as follows:

(1) At days 3, 7, and 14, the group with a 10% substitution rate showed the highest compressive strength. However, by day 28, the group with a 20% substitution rate presented the highest compressive strength. The peak of acoustic emission ring-down count was observed mainly in the unstable fracture development stage (yield stage) before the stress peak and after the yield point. When the substitution rate was 20%, the peak was the highest, and the amount of accumulated energy was the largest at day 28. In that same day, the failure mode was similar to two opposite pyramid-shaped fractures for substitution rate between 10% and 30%, whereas, for 0% or 40%, the failure mode was closer to a monoclinal fracture. It was observed in the SEM images that the calcium silicate hydrates in CGCAB have a fibrillar morphology and are mostly generated when the substitution rate was 20%.

(2) At day 3, the shear strength showed a tendency to gradually decrease, and the group with a substitution rate of 0% presented the highest shear strength. At days 7, 14, and 28, the shear strength first increased and then decreased. However, the corresponding substitution rate for the group with the highest shear strength was different (gradual transition from 10% to 20%). The Mohr-Coulomb criterion was applied to the shear strength test analysis of CGCAB. At days 3 and 14, the internal friction angle gradually increased, while the cohesion gradually decreased. At days 7 and 28, the internal friction angle first decreased and then increased, whereas the cohesion first increased and then decreased. In terms of shear strength, a 20% CSFA substitution rate is recommended for suitable internal friction angles and cohesion.

(3) The drying shrinkage increased with extended age, and the fastest shrinking rates of CGCAB under natural dry conditions occurred from day 3 to day 7. The group with a substitution rate of 20% presented the largest drying shrinkage at any age. The addition of CSFA can accelerate the completion of drying shrinkage.

Data Availability

The data used to support the findings of this study are included within the article.

Conflicts of Interest

The authors declare that they have no conflicts of interest.

Acknowledgments

This work was supported by the Joint Research Fund under a cooperative agreement between the NSFC and Funds for Coal-Based Low-Carbon Technology of Shanxi (nos. U1710258 and U1810120); the National Natural Science Foundation of China (nos. 51574172 and 51804208); the Key Research and Development Program (Social Development) of Shanxi Province (201803D31044); the Research Fund of the State Key Laboratory of Coal Resources and Safe Mining, CUMT (SKLCRSM18KF016); and the China Postdoctoral Science Foundation (2018M632423). Thanks are due to all who supported this basic research.

References

[1] X. X. Miao and M. G. Qian, "Research on green mining of coal resources in China: current status and future prospects," *Journal of Mining and Safety Engineering*, vol. 26, no. 1, pp. 1–14, 2009.

[2] X. J. Zhu, G. L. Guo, J. F. Zha, T. Chen, Q. Fang, and X. Y. Yang, "Surface dynamic subsidence prediction model of solid backfill mining," *Environmental Earth Sciences*, vol. 75, no. 12, p. 1007, 2016.

[3] M. Fall and M. Pokharel, "Coupled effects of sulphate and temperature on the strength development of cemented tailings backfills: portland cement-paste backfill," *Cement and Concrete Composites*, vol. 32, no. 10, pp. 819–828, 2010.

[4] M. Helinski, M. Fahey, and A. Fourie, "Coupled two-dimensional finite element modelling of mine backfilling with cemented tailings," *Canadian Geotechnical Journal*, vol. 47, no. 11, pp. 1187–1200, 2010.

[5] J. Huazhe, W. Shufei, Y. Yixuan, and X. Chen, "Water recovery improvement by shearing of gravity-thickened tailings for cemented paste backfill," *Journal of Cleaner Production*, vol. 245, p. 118882, 2020.

[6] Y. Feng, Q. Yang, Q. Chen et al., "Characterization and evaluation of the pozzolanic activity of granulated copper slag modified with cao," *Journal of Cleaner Production*, vol. 232, pp. 1112–1120, 2019.

[7] P.-M. Wang and X.-P. Liu, "Effect of temperature on the hydration process and strength development in blends of portland cement and activated coal gangue or fly ash," *Journal of Zhejiang University-SCIENCE A*, vol. 12, no. 2, pp. 162–170, 2011.

[8] D. Wu, S.-J. Cai, and Y.-C. Liu, "Effects of binder on suction in cemented gangue backfill," *Magazine of Concrete Research*, vol. 68, no. 12, pp. 593–603, 2016.

[9] D. Wu, T. Deng, and R. Zhao, "A coupled thmc modeling application of cemented coal gangue-fly ash backfill," *Construction and Building Materials*, vol. 158, pp. 326–336, 2018.

[10] B. Yin, T. Kang, J. Kang, and Y. Chen, "Experimental and mechanistic research on enhancing the strength and deformation characteristics of fly-ash-cemented filling materials modified by electrochemical treatment," *Energy & Fuels*, vol. 32, no. 3, pp. 3614–3626, 2018.

[11] Q. Sun, B. Li, S. Tian, C. Cai, and Y. Xia, "Creep properties of geopolymer cemented coal gangue-fly ash backfill under dynamic disturbance," *Construction and Building Materials*, vol. 191, pp. 644–654, 2018.

[12] H.-Z. Jiao, S.-F. Wang, A.-X. Wu, H.-M. Shen, and J.-D. Wang, "Cementitious property of naalo2-activated ge slag as cement supplement," *International Journal of Minerals, Metallurgy and Materials*, vol. 26, no. 12, pp. 1594–1603, 2019.

[13] Y. He, Q. Chen, C. Qi, Q. Zhang, and C. Xiao, "Lithium slag and fly ash-based binder for cemented fine tailings backfill," *Journal of Environmental Management*, vol. 248, Article ID 109282, , 2019.

[14] Q.-S. Chen, Q.-L. Zhang, A. Fourie, X. Chen, and C.-C. Qi, "Experimental investigation on the strength characteristics of cement paste backfill in a similar stope model and its mechanism," *Construction and Building Materials*, vol. 154, pp. 34–43, 2017.

[15] Y. Bi, C. Gao, Y. Wang, and B. Li, "Estimation of straw resources in China," *Transactions of the CSAE*, vol. 25, no. 12, pp. 211–217, 2009.

[16] Z. Wang, T. Lei, M. Yang et al., "Life cycle environmental impacts of cornstalk briquette fuel in China," *Applied Energy*, vol. 192, pp. 83–94, 2017.

[17] G. R. Feng, T. Y. Qi, Z. H. Wang, J. W. Bai, and Z. Li, "Physical and chemical characterization of Chinese maize stalk leaf ash: calcining temperature and aqueous solution," *Bioresources*, vol. 14, no. 1, pp. 977–995, 2019.

[18] G. G. Kaya, E. Yilmaz, and H. Deveci, "Sustainable nanocomposites of epoxy and silica xerogel synthesized from corn stalk ash: enhanced thermal and acoustic insulation performance," *Composites Part B: Engineering*, vol. 150, pp. 1–6, 2018.

[19] R. K. Sandhu and R. Siddique, "Influence of rice husk ash (rha) on the properties of self-compacting concrete: a review," *Construction And Building Materials*, vol. 153, pp. 751–764, 2017.

[20] A. N. Givi, S. A. Rashid, F. N. A. Aziz, and M. A. M. Salleh, "Assessment of the effects of rice husk ash particle size on strength, water permeability and workability of binary blended concrete," *Construction and Building Materials*, vol. 24, no. 11, pp. 2145–2150, 2010.

[21] M. R. Elias, V. A. Javad, and D. M. Reza, "Mechanical performance of self-compacting concrete incorporating rice husk ash," *Construction and Building Materials*, vol. 177, pp. 148–157, 2018.

[22] C. Fapohunda, B. Akinbile, and S. Ahmed, "Structure and properties of mortar and concrete with rice husk ash as partial replacement of ordinary Portland cement-a review," *International Journal of Sustainable Built Environment*, vol. 6, no. 2, pp. 675–692, 2017.

[23] R. Madandoust, M. M. Ranjbar, H. A. Moghadam, and S. Y. Mousavi, "Mechanical properties and durability assessment of rice husk ash concrete," *Biosystems Engineering*, vol. 110, no. 2, pp. 144–152, 2011.

[24] N. Van Tuan, G. Ye, K. van Breugel, and O. Copuroglu, "Hydration and microstructure of ultra high performance concrete incorporating rice husk ash," *Cement and Concrete Research*, vol. 41, no. 11, pp. 1104–1111, 2011.

[25] M. S. Ismail and A. M. Waliuddin, "Effect of rice husk ash on high strength concrete," *Construction and Building Materials*, vol. 10, no. 7, pp. 521–526, 1996.

[26] F. A. Olutoge and P. A. Adesina, "Effects of rice husk ash prepared from charcoal-powered incinerator on the strength and durability properties of concrete," *Construction and Building Materials*, vol. 196, pp. 386–394, 2019.

[27] X. Du, G. Feng, Y. Zhang, Z. Wang, Y. Guo, and T. Qi, "Bearing mechanism and stability monitoring of cemented gangue-fly ash backfill column with stirrups in partial backfill engineering," *Engineering Structures*, vol. 188, pp. 603–612, 2019.

[28] T. Sinsiri, W. Kroehong, C. Jaturapitakkul, and P. Chindaprasirt, "Assessing the effect of biomass ashes with different finenesses on the compressive strength of blended cement paste," *Materials & Design*, vol. 42, pp. 424–433, 2012.

[29] T. Zhang, H. Chen, X. Li, and Z. Zhu, "Hydration behavior of magnesium potassium phosphate cement and stability analysis of its hydration products through thermodynamic modeling," *Cement and Concrete Research*, vol. 98, pp. 101–110, 2017.

[30] S. M. S. Kazmi, M. J. Munir, P. Indubhushan, and Y.-F. Wu, "Pozzolanic reaction of sugarcane bagasse ash and its role in controlling alkali silica reaction," *Construction and Building Materials*, vol. 148, pp. 231–240, 2017.

[31] A. K. Parande, K. Stalin, R. K. Thangarajan, and M. S. Karthikeyan, "Utilization of agroresidual waste in effective blending in portland cement," *ISRN Civil Engineering*, vol. 2011, pp. 1–12, 2011.

[32] I. G. Richardson, "Tobermorite/jennite- and tobermorite/calcium hydroxide-based models for the structure of C-S-H: applicability to hardened pastes of tricalcium silicate, β-dicalcium silicate, Portland cement, and blends of Portland cement with blast-furnace slag, metakaolin, or silica fume," *Cement and Concrete Research*, vol. 34, no. 9, pp. 1733–1777, 2004.

[33] L. Zhang, K. Yamauchi, Z. Li, X. Zhang, H. Ma, and S. Ge, "Novel understanding of calcium silicate hydrate from dilute

hydration," *Cement and Concrete Research*, vol. 99, pp. 95–105, 2017.

[34] T. Qi and G. Feng, "Resistivity and ae response characteristics in the failure process of cgb under uniaxial loading," *Advances In Materials Science And Engineering*, vol. 2017, Article ID 7857590, 11 pages, 2017.

[35] S. Cao, E. Yilmaz, W. Song, E. Yilmaz, and G. Xue, "Loading rate effect on uniaxial compressive strength behavior and acoustic emission properties of cemented tailings backfill," *Construction and Building Materials*, vol. 213, pp. 313–324, 2019.

[36] G. Feng, X. Du, and Y. Zhang, ""Optical-acoustic-stress" responses in failure progress of cemented gangue-fly ash backfill material under uniaxial compression," *Nondestructive Testing and Evaluation*, vol. 34, no. 2, pp. 135–146, 2019.

[37] T. Szwedzicki, "A hypothesis on modes of failure of rock samples tested in uniaxial compression," *Rock Mechanics and Rock Engineering*, vol. 40, no. 1, pp. 97–104, 2006.

[38] D. A. Moran and C. P. Pantelides, "Elliptical and circular FRP-confined concrete sections: a Mohr-Coulomb analytical model," *International Journal of Solids and Structures*, vol. 49, no. 6, pp. 881–898, 2012.

[39] D. A. Moran, C. P. Pantelides, and L. D. Reaveley, "Mohr-coulomb model for rectangular and square frp-confined concrete," *Composite Structures*, vol. 209, pp. 889–904, 2019.

[40] L.-S. Tang, H.-T. Sang, J. Song, Z.-G. Luo, and Y.-L. Sun, "Mechanical model for failure modes of rock and soil under compression," *Transactions of Nonferrous Metals Society of China*, vol. 26, no. 10, pp. 2711–2723, 2016.

[41] D. He, W. Yang, and Y. Cheng, "Surface morphology of structural plane and effects of the shear strength parameters," *Advances in Civil Engineering*, vol. 2018, pp. 1–7, 2018.

[42] J. Yang, Q. Wang, and Y. Zhou, "Influence of curing time on the drying shrinkage of concretes with different binders and water-to-binder ratios," *Advances in Materials Science and Engineering*, vol. 2017, Article ID 2695435, 10 pages, 2017.

[43] J. Li and Y. Yao, "A study on creep and drying shrinkage of high performance concrete," *Cement and Concrete Research*, vol. 31, no. 8, pp. 1203–1206, 2001.

[44] I. G. Richardson, "The calcium silicate hydrates," *Cement and Concrete Research*, vol. 38, no. 2, pp. 137–158, 2008.

Hindawi
Advances in Materials Science and Engineering
Volume 2020, Article ID 5828514, 15 pages
https://doi.org/10.1155/2020/5828514

Research Article

Roof Movement and Failure Behavior When Mining Extra-Thick Coal Seams Using Upward Slicing Longwall-Roadway Cemented Backfill Technology

Xuejie Deng,[1,2,3] **Zongxuan Yuan**,[1] **Lixin Lan**,[4] **Benjamin de Wit**,[5] **and Junwen Zhang**[1]

[1]*School of Energy and Mining Engineering, China University of Mining and Technology, Beijing 100083, China*
[2]*State Key Laboratory of Coal Resources and Safe Mining, China University of Mining and Technology, Xuzhou 221116, China*
[3]*Kailuan (Group) Limited Liability Corporation, Tangshan 063018, China*
[4]*Department of Civil Engineering, Shanghai Jiao Tong University, Shanghai 200240, China*
[5]*Norman B. Keevil Institute of Mining Engineering, University of British Columbia, Vancouver, BC V6T 1Z4, Canada*

Correspondence should be addressed to Xuejie Deng; dengxj1989@gmail.com

Received 26 August 2019; Accepted 7 November 2019; Published 10 January 2020

Guest Editor: Qiusong Chen

A novel and environmental-friendly backfill mining method known as upward slicing longwall-roadway cemented backfill (USLCB) technology has recently been proposed and successfully applied in mines extracting extra-thick coal seams located under sensitive areas. This paper studies the effects USLCB had on roof movement and failure behavior using the mechanical analysis approach. The application of USLCB in the Gonggeyingzi Mine is taken as a case study with roof movement behavior being monitored over a single mining cycle, as well as over multiple mining cycles of different coal slices. In addition, backfill performance requirements to prevent roof failures where USLCB is implemented are studied. The results show that the deflection curves of the roof at the end of each mining cycle during mining the first and the six slices are symmetrical, but they change from asymmetrical to symmetrical during the mining progresses of the second slice to the fifth slice. The final state of roof movement after the first slice, and through to the fifth slice, displays an obvious "flat bottom" pattern in the middle of the deflection curve. The roof movement during the removal of the top slice is noticeably different from other slices. The results also show that the requirements of the elastic modulus, as well as the strength of the backfill, increase as the number of mined slices increases from 1 to 5, but the requirements drop sharply for mining the top slice.

1. Introduction

The process of mining can be defined as economically recovering valuable minerals or other materials from the earth's crust either at the surface or underground [1, 2]. Thick coal seams whose thickness is over 3.5 m comprise approximately half of the world's coal reserves and 70–80% of thick coal seams are extracted using underground mining methods [3, 4]. In underground mining, the underground voids created as a result of extracting the valuable materials can present serious environmental challenges and are expected to be managed and remedied by filling them through a process known as backfilling technology [5–7]. Backfilling technology can control ground movement and prevent strata fracture and surface subsidence, as well as serve as an opportunity to dispose waste materials created during the extraction process [8, 9]. An important backfill technology is cemented paste backfill [10–14], which is widely used across the industry for filling excavated stopes with a mixture of mine waste materials such as tailings, slags, and water [15–18]. Although cemented backfill has been widely used in industry because of its advantages, such as high backfilling ratio and flexible distribution systems [19, 20], the technology has been rarely applied in operations that are extracting extra-thick coal seams.

There are currently two main backfill mining methods used for extracting the majority of thick coal seams, including single-pass backfill mining and multislice backfill mining [3, 4, 21, 22].

The major constraint with applying the single-pass backfill mining method in extra-thick coal seams is the limiting factor of the maximum mining height [23, 24]. The multislice backfill mining method can provide a viable alternative to the previously stated methods for mining extra-thick coal seams as the backfill can support the overlying strata and prevent fractures and failures from developing [25, 26].

A novel and environmental-friendly mining and backfilling method known as upward slicing longwall-roadway cemented backfill (USLCB) technology to be proposed by Deng et al. and was initially published in 2017 [14]. The technical principles of the USLCB are shown in Figure 1 and described as follows [14]. The cemented backfill is prepared in a backfill plant at the surface and is transported underground to stopes through a network of backfilling pipelines [7, 27–29]. The extra-thick coal seam is divided into several slices with the deepest slice being mined first and the resulting void being filled with backfill material [30, 31]. Once the backfill material hardens [32, 33], it is used as a floor to facilitate the mining of the subsequent overlying slices as the entire coal seam is mined out progressively from bottom to top. The general longwall mining roadway system, including the preparation of roadways and gateways, is constructed prior to mining each slice. The roadheader is used to excavate crosscuts from the headgate to the tailgate, and after one crosscut is driven, it is filled with cemented backfill while the next crosscut is driven concurrently. A mining cycle contains 7 mining steps, and the mining sequence has been shown in Figure 2. After a mining cycle is finished, the coal pillar between first and second backfilling sections is totally mined out. The driving of crosscuts and the backfilling processes are repeated until the entire slice is mined out and backfilled.

The USLCB technology was applied to extract an extra-thick coal seam with a thickness of 21 meters located under aquifers to protect the water, and it achieved positive application results [14]. However, although USLCB has indicated it can be a successful technology, the roof movement and failure behavior of USLCB need to be studied further. In this paper, a mechanical analysis approach is used to study roof movement behavior in mining extra-thick coal seams using USLCB technology. The application of this technology in the Gonggeyingzi Coal Mine is taken as a case study, with the roof movement behavior monitored and analyzed over a single mining cycle, over multiple mining cycles, and within each pass to excavate the different slices. In addition, the performance requirements of backfill material to prevent roof failures during the mining process of USLCB are calculated.

2. The Roof Movement of Each Slice in the Mining Process of USLCB

A mechanical analysis approach [34–36] is used to study the roof movement characteristics during the mining of each slice when extracting an extra-thick coal seam using USLCB technology. Nonhomogeneous elastic foundation beam models are developed in which the roof during the USLCB mining process is simplified as a beam. The mining process of USLCB is also considered in the mechanical models. It should be noted that the term roof is used to refer to different things. It refers to the stratum above the coal seam during the mining of the top slice. However, during the mining of the bottom slices, the roof refers to the remaining coal located above the extracted slice.

The coal body, backfilling body, and the combination of coal and backfilling are sectionally simplified as nonhomogeneous elastic foundations in the mechanical models [37–39]. According to the specific conditions of mining the extra-thick coal seam using USLCB technology, two mechanical models are established: a mechanical model for mining the first slice, located at the bottom, and another mechanical model for mining the remaining overlying slices.

2.1. The Roof Movement Behavior of the First Slice

2.1.1. The Mechanical Model of Mining the First Slice. The process of USLCB technology is that mined-out space is immediately filled with backfill material so that overlying strata are supported by the backfilling body and the coal pillars. The foundation structure of mining the first slice is shown in Figure 2. Therein, L_s represents the total length of the mining area; L is the length of each mining cycle; n is the number of completed mining cycles; nL is the length of mined range; n_s represents the individual steps within the mining cycle; a represents the width of each excavation step; l_1 and l_3 denote the width of first and second backfilling sections in a mining cycle, respectively; l_2 is the width of the coal pillar between the first and second backfilling sections in a mining cycle; and l_4 is the width of the coal pillar after the second backfilling section in a mining cycle.

During the mining cycling, the values of l_1, l_2, l_3, and l_4 are constantly changing as the mining and backfilling operations undertaken; however, the sum of these lengths is fixed, as shown in the following equation:

$$L = l_1 + l_2 + l_3 + l_4. \tag{1}$$

There are 7 excavation steps in each mining cycle, so the value of n_s is from 1 to 7. The sizes of the crosscuts, pillars, and backfilling areas represented by the values l_1, l_2, l_3, and l_4 change as each step of the mining cycle is completed, and how these values change with each step of the mining cycle is summarized in Table 1.

The mechanical model of mining the first slice is shown in Figure 3, in which the elastic foundation beam is divided into 5 sections. Therein, L_0 and L_4 represent the range of the stress-concentrated area in the boundary pillars; L_1 is the range from the left mining limit boundary to the first coal pillar which means the width of past mining cycles plus the width of the first backfilling section in current mining cycle; L_2 is the width of the coal pillar between the first and second backfilling sections in present mining cycle; and L_3 represents the width of the second backfilling section in present mining cycle which begins after the first coal pillar and ends at the second coal pillar.

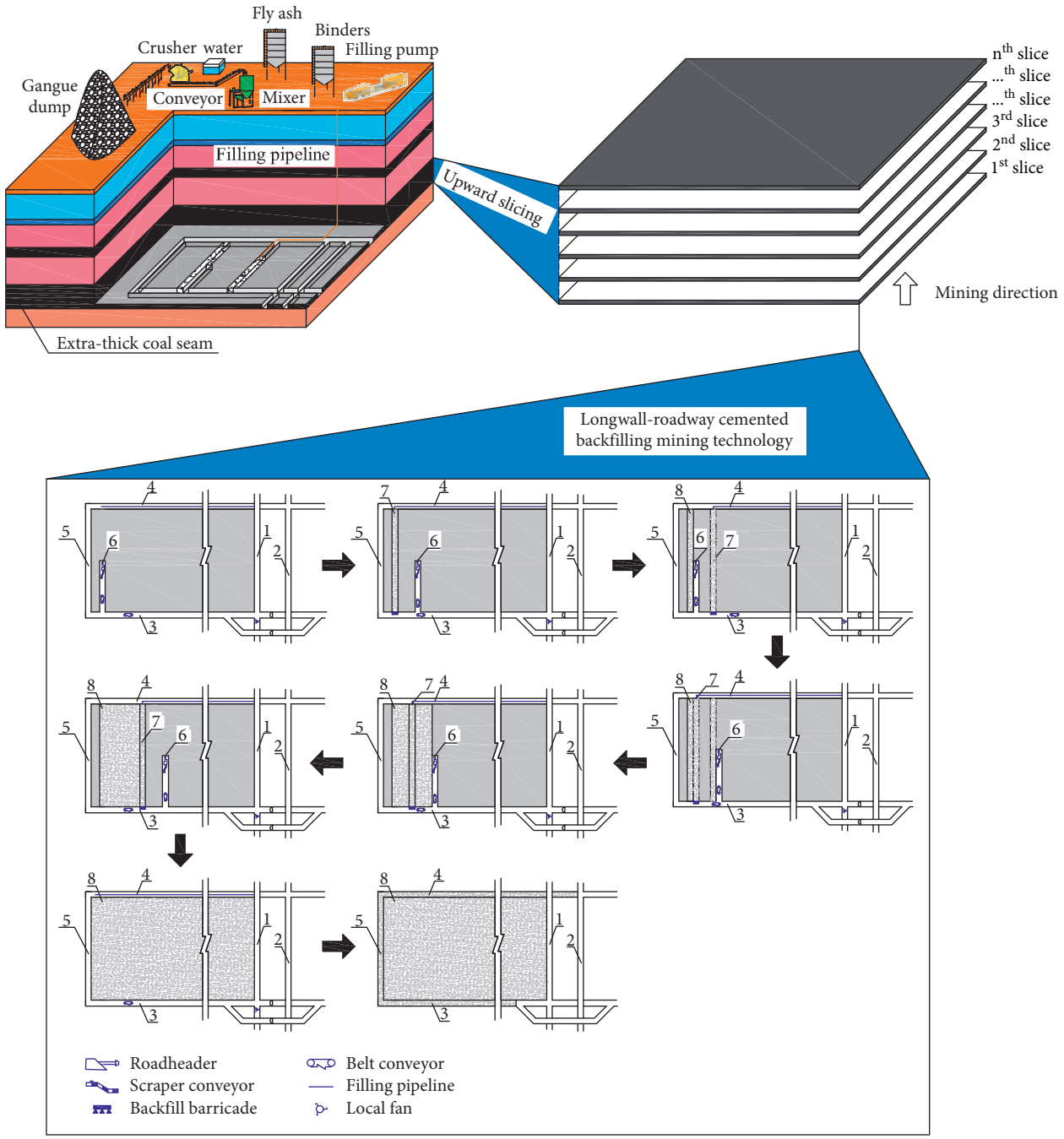

FIGURE 1: The technical principles of USLCB [14]. (1) Haulage rise; (2): rail rise; (3) headgate; (4) tailgate; (5) boundary crosscut; (6) mining working face; (7) backfilling working face; (8) backfilled body.

The parametric correspondence between the mechanical model of USLCB and the mining process of USLCB is shown in the following equation:

$$\begin{cases} L_1 = nL + l_1, \\ L_2 = l_2, \\ L_3 = l_3. \end{cases} \tag{2}$$

2.1.2. The Mechanical Analysis of Roof Deflection during the Mining of the First Slice. Taking the point O of the beam as the origin, a coordinate system is established with the X-axis as the direction of mining and the Y-axis as the vertically downward direction. These axes are shown in Figure 3. Therein, k_c and k_g are the elastic foundation coefficients of coal and the backfilling body, respectively. The deflection calculation process of the beam is shown as follows:

(1) Section L_0: $-L_0 - L_1 \le x \le -L_1$

When $-L_0 - L_1 \le x \le -L_1$, the differential equation for deflection of the roof is shown in the following equation:

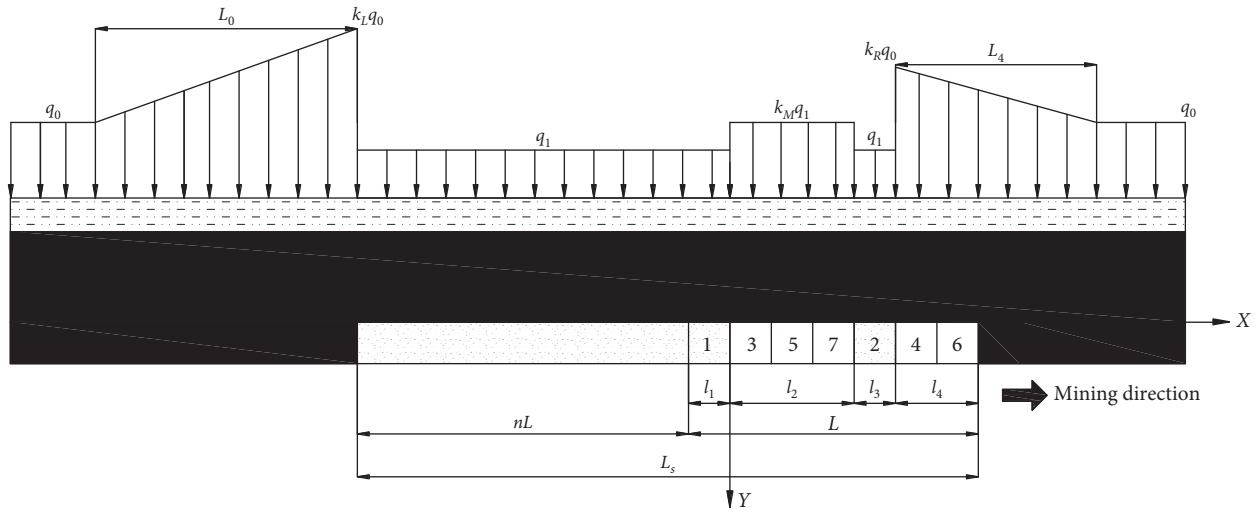

Figure 2: Diagram of the foundation structure for mining the first slice.

Table 1: The foundation structure of different excavation steps in a mining cycle.

n_s	l_1	l_2	l_3	l_4
1	a	$3a$	0	$4a$
2	a	$3a$	a	$3a$
3	$2a$	$2a$	a	$3a$
4	$2a$	$2a$	$2a$	$2a$
5	$3a$	a	$2a$	$2a$
6	$3a$	a	$3a$	a
7	$4a$	0	$3a$	a

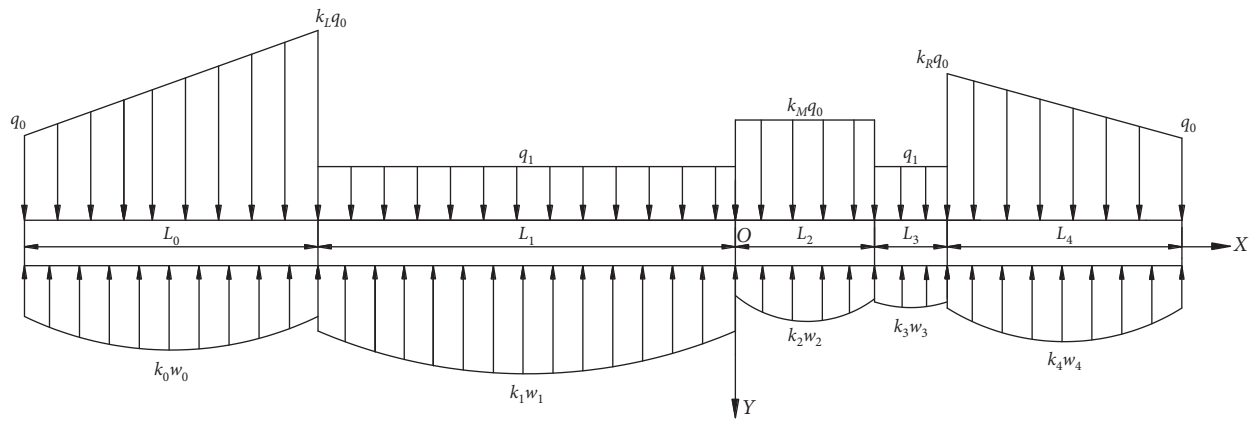

Figure 3: Mechanical model of mining first slice.

$$EI\frac{d^4w_0(x)}{dx^4} + k_0w_0(x) = q_1(x). \tag{3}$$

The load on the coal pillar can be expressed as follows:

$$q_1(x) = \frac{(k_l - 1)q_0}{L_0}x + k_lq_0 + \frac{L_1(k_l - 1)q_0}{L_0}, \tag{4}$$

where k_l is the dimensionless stress concentration factor.

The deflection of the roof section L_0 is shown in the following equation:

$$w_0(x) = e^{\alpha x}\left(A_0\cos(\alpha x) + B_0\sin(\alpha x)\right) + e^{-\alpha x}\left(C_0\cos(\alpha x) + D_0\sin(\alpha x)\right) + \frac{q_1(x)}{k_0}, \tag{5}$$

where $\alpha = \sqrt[4]{k_0/4EI} = \sqrt[4]{k_c/4EI}$ is the characteristic coefficient, in which $k_0 = k_c$ is the elastic foundation

coefficient of coal body, N/m^3; E is the elastic modulus of the roof, Pa; and I is the moment of inertia of the roof section, m^4.

As "x" tends towards negative infinity, the deflection of the roof is constant. The roof can be considered as a semi-infinite body, and this allows equation (5) to be simplified as follows:

$$w_0(x) = e^{\alpha x}\left(A_0\cos(\alpha x) + B_0\sin(\alpha x)\right) + \frac{1}{k_0}\left[\frac{(k_l-1)q_0}{L_0}x + k_l q_0 + \frac{L_1(k_l-1)q_0}{L_0}\right]. \tag{6}$$

(2) Section L_1: $-L_1 \le x \le 0$

When $-L_1 \le x \le 0$, the differential equation for deflection of the roof is shown in the following equation:

$$EI\frac{\mathrm{d}^4 w_1(x)}{\mathrm{d}x^4} + k_1 w_1(x) = q_1. \tag{7}$$

The deflection of the roof in section L_1 can be obtained and shown in the following equation:

$$w_1(x) = e^{-\beta x}\left(A_1\cos(\beta x) + B_1\sin(\beta x)\right) + e^{\beta x}\left(C_1\cos(\beta x) + D_1\sin(\beta x)\right) + \frac{q_1}{k_1}, \tag{8}$$

where $\beta = \sqrt[4]{k_1/4EI} = \sqrt[4]{k_g/4EI}$ is the characteristic coefficient, in which $k_1 = k_g$ is the elastic foundation coefficient of backfilling body, N/m^3.

(3) Section L_2: $0 < x \le L_2$

When $0 < x \le L_2$, the differential equation for deflection of the roof is shown in the following equation:

$$EI\frac{\mathrm{d}^4 w_2(x)}{\mathrm{d}x^4} + k_2 w_2(x) = k_m q_0, \tag{9}$$

where k_m is the dimensionless stress concentration factor.

The deflection of the roof section L_2 can be obtained and shown in the following equation:

$$w_2(x) = e^{-\alpha x}\left(A_2\cos(\alpha x) + B_2\sin(\alpha x)\right) + e^{\alpha x}\left(C_2\cos(\alpha x) + D_2\sin(\alpha x)\right) + \frac{k_m q_0}{k_2}, \tag{10}$$

where $k_2 = k_c$ is the elastic foundation coefficient of coal body, N/m^3.

(4) Section L_3: $L_2 < x \le L_2 + L_3$

When $L_2 < x \le L_2 + L_3$, the differential equation for deflection of the roof is shown in the following equation:

$$EI\frac{\mathrm{d}^4 w_3(x)}{\mathrm{d}x^4} + k_3 w_3(x) = q_1. \tag{11}$$

The deflection of the roof in section L_3 can be expressed as follows:

$$w_3(x) = e^{-\beta x}\left(A_3\cos(\beta x) + B_3\sin(\beta x)\right) + e^{\beta x}\left(C_3\cos(\beta x) + D_3\sin(\beta x)\right) + \frac{q_1}{k_3}, \tag{12}$$

where $k_3 = k_g$ is the elastic foundation coefficient of backfilling body, N/m^3.

(5) Section L_4: $L_2 + L_3 < x \le L_2 + L_3 + L_4$

When $L_2 + L_3 < x \le L_2 + L_3 + L_4$, the differential equation for deflection of the roof is shown in the following equation:

$$EI\frac{\mathrm{d}^4 w_4(x)}{\mathrm{d}x^4} + k_4 w_4(x) = q_2(x). \tag{13}$$

The load on the coal pillar can be expressed as follows:

$$q_2(x) = \frac{(1-k_r)q_0}{L_4}x + k_r q_0 + \frac{(L_2+L_3)(k_r-1)q_0}{L_4}, \tag{14}$$

where k_r is the dimensionless stress concentration factor.

The deflection of the roof section L_4 is shown in the following equation:

$$w_4(x) = e^{-\alpha x}\left(A_4\cos(\alpha x) + B_4\sin(\alpha x)\right) + e^{\alpha x}\left(C_4\cos(\alpha x) + D_4\sin(\alpha x)\right) + \frac{q_2(x)}{k_4}, \tag{15}$$

where $k_4 = k_c$ is the elastic foundation coefficient of coal body, N/m^3.

As "x" tends towards positive infinity, the deflection of the roof is constant. The roof can be considered as a semi-infinite body, and equation (15) can be simplified as follows:

$$w_4(x) = e^{-\alpha x}\left(A_4\cos(\alpha x) + B_4\sin(\alpha x)\right) + \frac{1}{k_4}\left[\frac{(1-k_r)q_0}{L_4}x + k_r q_0 + \frac{(L_2+L_3)(k_r-1)q_0}{L_4}\right]. \tag{16}$$

The rotation $\theta(x)$, bending moment $M(x)$, and shearing force $Q(x)$ of an arbitrary cross section of the beam can be calculated by using the following equation:

$$\begin{cases} \theta(x) = \dfrac{\mathrm{d}w(x)}{\mathrm{d}x}, \\ M(x) = -EI\dfrac{\mathrm{d}w^2(x)}{\mathrm{d}x^2}, \\ Q(x) = -EI\dfrac{\mathrm{d}w^3(x)}{\mathrm{d}x^3}. \end{cases} \tag{17}$$

The boundary conditions and the continuity conditions of the mechanical model are shown in equation (18). All the parameters of the model can be solved according to the following conditions:

$$\begin{cases} w_0(-L_1) = w_1(-L_1), \\ \theta_0(-L_1) = \theta_1(-L_1), \\ M_0(-L_1) = M_1(-L_1), \\ Q_0(-L_1) = Q_1(-L_1), \\ w_1(0) = w_2(0), \\ \theta_1(0) = \theta_2(0), \\ M_1(0) = M_2(0), \\ Q_1(0) = Q_2(0), \\ w_2(L_2) = w_3(L_2), \\ \theta_2(L_2) = \theta_3(L_2), \\ M_2(L_2) = M_3(L_2), \\ Q_2(L_2) = Q_3(L_2), \\ w_3(L_2 + L_3) = w_4(L_2 + L_3), \\ \theta_3(L_2 + L_3) = \theta_4(L_2 + L_3), \\ M_3(L_2 + L_3) = M_4(L_2 + L_3), \\ Q_3(L_2 + L_3) = Q_4(L_2 + L_3). \end{cases} \tag{18}$$

2.2. Roof Movement Behavior of the Remaining Upper Slices

2.2.1. The Mechanical Model of Mining the Remaining Upper Slices. When mining the first slice using the USLCB method, the floor is composed of the undisturbed original ground. However, after the first slice is mined, and subsequently backfilled, the remaining upper slices will have the backfilling body serving as their floor for mining activities. Therefore, the foundation structure for mining these remaining slices will be different from the first slice, as shown in Figure 4.

The mechanical model of mining the remaining upper slices is shown in Figure 5, in which the elastic foundation beam is divided into 6 sections. Therein, L_5 and L_{10} represent the range of the stress-concentrated area in the boundary pillars; L_6 is the range that is a combination of past mining cycles and the first backfilling section in current mining cycle; L_7 is the range of the coal pillar between the first and second backfilling sections in current mining cycle; L_8 represents the range of the second backfilling section in current mining cycle; and L_9 is the range of the coal pillar between the second backfilling sections in current mining cycle and the mining boundary of the previous slice.

The parametric correspondence between the mechanical model and applying USLCB to mining the remaining slices is shown in the following equation:

$$\begin{cases} L_6 = nL + l_1, \\ L_7 = l_2, \\ L_8 = l_3, \\ L_9 = L_s - (L_6 + L_7 + L_8). \end{cases} \tag{19}$$

2.2.2. Mechanical Model for Calculating Deflection When Mining the Remaining Upper Slices. The mechanical model to determine deflection when mining the remaining upper slices that follow the mining of the first slice is similar to how deflection was calculated when mining the first slice, and the deflection calculation process of the beam is shown as follows:

(1) Section L_5: $-L_5 - L_6 \le x \le -L_6$

When $-L_5 - L_6 \le x \le -L_6$, the differential equation for deflection of the roof is shown in the following equation:

$$EI\frac{\mathrm{d}^4 w_5(x)}{\mathrm{d}x^4} + k_5 w_5(x) = q_3(x). \tag{20}$$

The load on the coal pillar can be expressed as follows:

$$q_3(x) = \frac{(l_1 - 1)q_0}{L_5}x + l_1 q_0 + \frac{L_6(l_1 - 1)q_0}{L_5}, \tag{21}$$

where l_1 is the dimensionless stress concentration factor.

The deflection of the roof in section L_5 is shown in the following equation:

$$\begin{aligned} w_5(x) = {} & e^{\alpha_5 x}(A_5\cos(\alpha_5 x) + B_5\sin(\alpha_5 x)) + e^{-\alpha_5 x} \\ & \cdot (C_5\cos(\alpha_5 x) + D_5\sin(\alpha_5 x)) + \frac{q_3(x)}{k_5}, \end{aligned} \tag{22}$$

where $\alpha_5 = \sqrt[4]{k_5/4EI}$ is the characteristic coefficient, in which $k_5 = k_c/i$ $(i = 2, \ldots, 6)$ is the elastic foundation coefficient of coal body, N/m^3; E is the elastic modulus of the roof, Pa; and I is the moment of inertia of the roof section, m^4.

As "x" tends towards negative infinity, the deflection of the roof is constant. The roof can be considered as a semi-infinite body, so $C_5 = 0$ and $D_5 = 0$, and equation (22) can be simplified as follows:

$$\begin{aligned} w_5(x) = {} & e^{\alpha_5 x}(A_5\cos(\alpha_5 x) + B_5\sin(\alpha_5 x)) \\ & + \frac{1}{k_5}\left[\frac{(l_1 - 1)q_0}{L_5}x + l_1 q_0 + \frac{L_6(l_1 - 1)q_0}{L_5}\right]. \end{aligned} \tag{23}$$

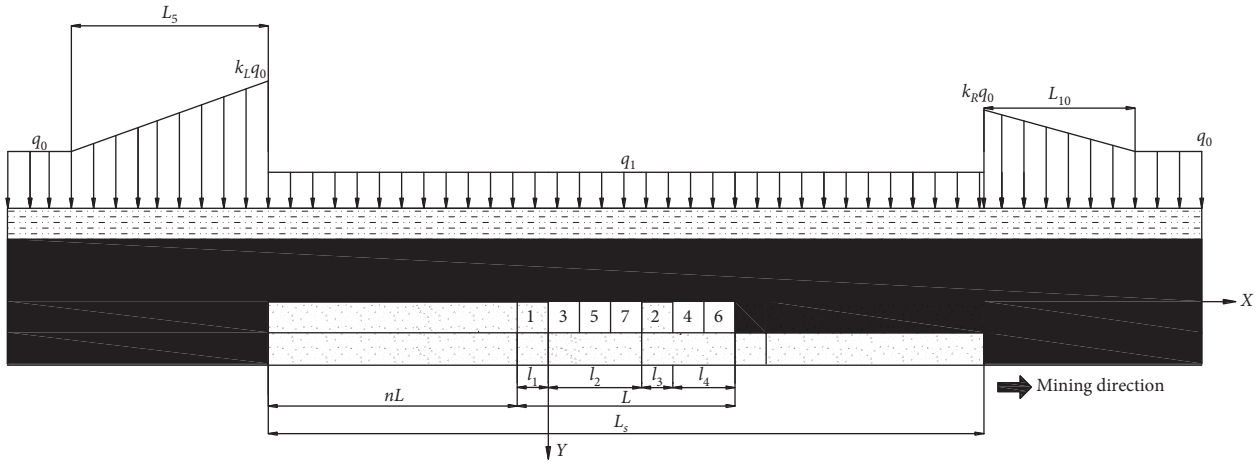

Figure 4: Foundation structure of mining the remaining upper slices.

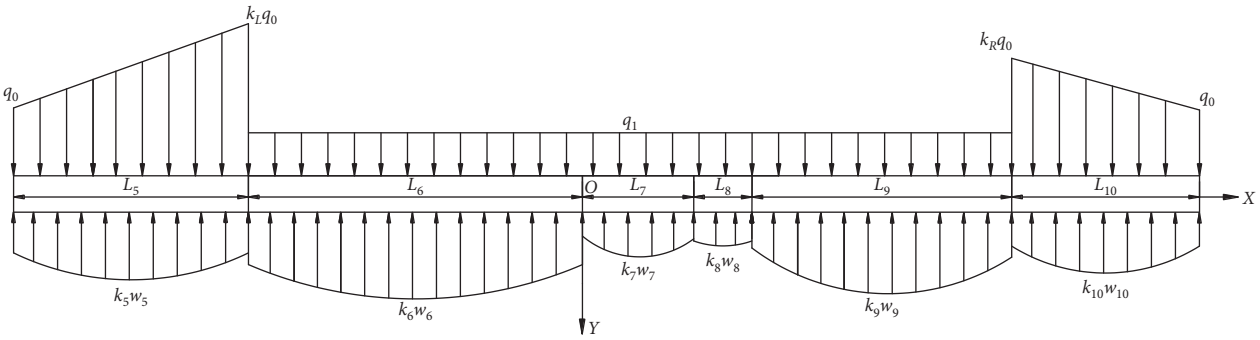

Figure 5: Mechanical model of mining the remaining upper slices.

(2) Section L_6: $-L_6 \le x \le 0$

When $-L_6 \le x \le 0$, the differential equation for deflection of the roof is shown in the following equation:

$$EI\frac{d^4w_6(x)}{dx^4} + k_6w_6(x) = q_2. \tag{24}$$

The deflection of the roof in section L_6 can be expressed as follows:

$$w_6(x) = e^{-\beta_6 x}\left(A_6\cos(\beta_6 x) + B_6\sin(\beta_6 x)\right) + e^{\beta_6 x}\left(C_6\cos(\beta_6 x) + D_6\sin(\beta_6 x)\right) + \frac{q_2}{k_6}, \tag{25}$$

where $\beta_6 = \sqrt[4]{k_6/4EI}$ is the characteristic coefficient, in which $k_6 = k_g/i$ $(i = 2, \ldots, 6)$ is the elastic foundation coefficient of the backfilling body, N/m^3.

(3) Section L_7: $0 < x \le L_7$

When $0 < x \le L_7$, the differential equation for deflection of the roof is shown in the following equation:

$$EI\frac{d^4w_7(x)}{dx^4} + k_7w_7(x) = q_2. \tag{26}$$

The deflection of the roof in section L_7 can be obtained and expressed as follows:

$$w_7(x) = e^{-\beta_7 x}\left(A_7\cos(\beta_7 x) + B_7\sin(\beta_7 x)\right) + e^{\beta_7 x}\left(C_7\cos(\beta_7 x) + D_7\sin(\beta_7)\right) + \frac{q_2}{k_7}, \tag{27}$$

where $\beta_7 = \sqrt[4]{k_7/4EI}$ is the characteristic coefficient, in which $k_7 = (k_c \cdot k_g)/((i-1)k_c + k_g)$ $(i = 2, \ldots, 6)$ is the elastic foundation coefficient for the combination of in situ coal and the backfilling body, N/m^3.

(4) Section L_8: $L_7 < x \le L_7 + L_8$

When $L_7 < x \le L_7 + L_8$, the differential equation for deflection of the roof is shown in the following equation:

$$EI\frac{d^4w_8(x)}{dx^4} + k_8w_8(x) = q_2. \tag{28}$$

The deflection of the roof in section L_8 can be expressed as follows:

$$w_8(x) = e^{-\beta_8 x}\left(A_8\cos(\beta_8 x) + B_8\sin(\beta_8 x)\right) + e^{\beta_8 x}\left(C_8\cos(\beta_8 x) + D_8\sin(\beta_8 x)\right) + \frac{q_2}{k_8}, \tag{29}$$

where $\beta_8 = \sqrt[4]{k_8/4EI}$ is the characteristic coefficient, in which $k_8 = k_g/i$ $(i = 2, \ldots, 6)$ is the elastic foundation coefficient of the backfilling body, N/m^3.

(5) Section L_9: $L_7 + L_8 < x \le L_7 + L_8 + L_9$

When $L_7 + L_8 < x \le L_7 + L_8 + L_9$, the differential equation for deflection of the roof is shown in the following equation:

$$EI\frac{\mathrm{d}^4 w_9(x)}{\mathrm{d}x^4} + k_9 w_9(x) = q_2. \tag{30}$$

The deflection of the roof section L_9 can be obtained and shown in the following equation:

$$\begin{aligned} w_9(x) = {} & e^{-\beta_9 x}\left(A_9\cos(\beta_9 x) + B_9\sin(\beta_9 x)\right) \\ & + e^{\beta_9 x}\left(C_9\cos(\beta_9 x) + D_9\sin(\beta_9 x)\right) + \frac{q_2}{k_9}, \end{aligned} \tag{31}$$

where $\beta_9 = \sqrt[4]{k_9/4EI}$ is the characteristic coefficient, in which $k_9 = (k_c \cdot k_g)/((i-1)k_c + k_g)$ $(i = 2, \ldots, 6)$ is the elastic foundation coefficient of the combination of backfilling and coal body, N/m^3.

(6) Section L_{10}: $L_7 + L_8 + L_9 < x \le L_7 + L_8 + L_9 + L_{10}$

When $L_7 + L_8 + L_9 < x \le L_7 + L_8 + L_9 + L_{10}$, the differential equation for deflection of the roof is shown in the following equation:

$$EI\frac{\mathrm{d}^4 w_{10}(x)}{\mathrm{d}x^4} + k_{10} w_{10}(x) = q_4(x). \tag{32}$$

The load on the coal pillar can be expressed as follows:

$$q_4(x) = \frac{(1-l_2)q_0}{L_{10}}x + l_2 q_0 + \frac{(L_7+L_8+L_{10})(l_2-1)q_0}{L_{10}}, \tag{33}$$

where l_2 is the dimensionless stress concentration factor.

The deflection of the roof section L_{10} is shown in the following equation:

$$\begin{aligned} w_{10}(x) = {} & e^{-\alpha_{10} x}\left(A_{10}\cos(\alpha_{10} x) + B_{10}\sin(\alpha_{10} x)\right) \\ & + e^{\alpha_{10} x}\left(C_{10}\cos(\alpha_{10} x) + D_{10}\sin(\alpha_{10} x)\right) + \frac{q_2(x)}{k_{10}}, \end{aligned} \tag{34}$$

where $\alpha_{10} = \sqrt[4]{k_{10}/4EI}$ is the characteristic coefficient, in which $k_{10} = k_c/i$ $(i = 2, \ldots, 6)$ is the elastic foundation coefficient of the coal body, N/m^3.

As "x" tends towards positive infinity, the deflection of the roof is constant. The roof can be considered as a semi-infinite body, so $C_{10} = 0$ and $D_{10} = 0$, and equation (34) can be simplified as follows:

$$\begin{aligned} w_{10}(x) = {} & e^{-\alpha_{10} x}\left(A_{10}\cos(\alpha_{10} x) + B_{10}\sin(\alpha_{10} x)\right) \\ & + \frac{1}{k_{10}}\left[\frac{(1-l_2)q_0}{L_{10}}x + l_2 q_0 + \frac{(L_7+L_8+L_{10})(l_2-1)q_0}{L_{10}}\right]. \end{aligned} \tag{35}$$

The boundary conditions and the continuity conditions of the mechanical model are shown in equation (36). All the parameters of the model can be solved according to the following conditions and equation (17):

$$\begin{cases} w_5(-L_6) = w_6(-L_6), \\ \theta_5(-L_6) = \theta_6(-L_6), \\ M_5(-L_6) = M_6(-L_6), \\ Q_5(-L_6) = Q_6(-L_6), \\ w_6(0) = w_7(0), \\ \theta_6(0) = \theta_7(0), \\ M_6(0) = M_7(0), \\ Q_6(0) = Q_7(0), \\ w_7(L_7) = w_8(L_7), \\ \theta_7(L_7) = \theta_8(L_7), \\ M_7(L_7) = M_8(L_7), \\ Q_7(L_7) = Q_8(L_7), \\ w_8(L_7+L_8) = w_9(L_7+L_8), \\ \theta_8(L_7+L_8) = \theta_9(L_7+L_8), \\ M_8(L_7+L_8) = M_9(L_7+L_8), \\ Q_8(L_7+L_8) = Q_9(L_7+L_8), \\ w_9(L_7+L_8+L_9) = w_{10}(L_7+L_8+L_9), \\ \theta_9(L_7+L_8+L_9) = \theta_{10}(L_7+L_8+L_9), \\ M_9(L_7+L_8+L_9) = M_{10}(L_7+L_8+L_9), \\ Q_9(L_7+L_8+L_9) = Q_{10}(L_7+L_8+L_9). \end{cases} \tag{36}$$

2.3. Roof Failure Criteria When Mining with USLCB Technology. The first strength theory, also known as the maximum tensile stress theory, is chosen as the failure criteria of the roof stratum. From the elastic foundation theory, the maximum tensile stress of the roof $\sigma_{\max}$ can be obtained from the maximum bending moment $M_{\max}$, which can be determined from the bending moment function $M(x)$, as shown in the following equation:

$$\sigma_{\max} = \frac{6 \cdot |M|_{\max}}{h^2}, \tag{37}$$

where h is the thickness of the roof, m.

Therefore, the failure criteria of the roof stratum can be expressed as follows:

$$|M|_{\max} \le \frac{h^2 \cdot [\sigma_{\max}]}{6}, \tag{38}$$

where $[\sigma_{max}]$ is the maximum allowable tensile stress of the roof, MPa.

3. Results and Discussion: A Case Study

The USLCB mining technology was applied at the Gonggeyingzi Coal Mine to exploit a 21 m thick coal seam that is located 52.3 m under multiple aquifers. Specific details about the location and geological conditions of this mine, as well as the mining technology implemented there, have been published in a previous paper entitled "Upward slicing longwall-roadway cemented backfilling technology for mining an extra-thick coal seam located under aquifers: a case study" [14]. The entire 21 m coal seam in this mine is divided equally into 6 slices, where the thickness of each slice is 3.5 m. The width of each excavation step is 5 m, the vertical in situ stress q_0 is 2.5 MPa, and the elastic modulus of the backfilling body is 10 MPa. To study the roof movement of mining different slices of the extra-thick coal seam with USLCB technology, the specific parameters of each unique mining condition in the mine are substituted into the deflection equations seen throughout Section 2, and the results are shown as follows.

3.1. Roof Movement Behavior inside a Single Mining Cycle. The process of extracting the first slice during the first mining cycle is used to explain the changes and development of roof movement and deformation behavior inside a single mining cycle. The deflection curves of the roof after each mining step during this process are shown in Figure 6.

Figure 6 shows that, over a single mining cycle, the deflection curves of the roof can be divided into three types, i.e., the small range unimodal deflection curve of step 1-1-1, the bimodal deflection curves of steps 1-1-2 through to 1-1-6, and the large range unimodal deflection curve of step 1-1-7.

(1) The small range unimodal deflection curve occurs during the first step (step 1-1-1) of the mining cycle and signifies a mining range that is a single backfilling crosscut. The maximum subsidence of the roof is 11.02 mm, and it appears in the middle of the deflection curve.

(2) Bimodal deflection curves occur through the second to the sixth mining steps (step 1-1-2 through to step 1-1-6) when there is a coal pillar in the middle of the mining range, which separates the active mining areas. When the mining range is symmetrical, the deflection curve is also symmetrically distributed. The two peaks appear above the two active parts of the mining range, respectively. The distance between two peaks varies between 25 and 30 m, and the maximum subsidence of the roof increases from 11.26 mm to 13.75 mm gradually.

(3) The large range unimodal deflection curve occurs during the last mining step (step 1-1-7) when the mining range is seven backfilling crosscuts and coal pillar in the middle has been removed. Although the shape of the deflection curve is similar to the curve during the first mining step, the subsidence range of the roof is much larger compared to the first mining step. The maximum subsidence of the roof appears in the middle of the deflection curve and it significantly increases to 25.22 mm.

3.2. Roof Movement Behavior during Multiple Mining Cycles. The first four mining cycles of each slice are used as examples to display different roof movement and deformation behavior during multiple mining cycles. The roof deflection curves of each slice at the end of the first four mining cycles are calculated and shown in Figure 7.

Figure 7(a) shows that all the roof deflection curves at the end of each mining cycle for the first slice all have a symmetrical distribution. As the number of mining cycles increases, both the range of roof subsidence and the maximum subsidence increase gradually. The maximum subsidence appears in the middle of the deflection curves. From the first to the fourth mining cycle of the first slice, the maximum subsidence of the roof is 25.22 mm, 45.48 mm, 52.86 mm, and 53.00 mm, respectively. After the third mining cycle of each slice, the maximum subsidence of the roof is almost achieved. Further subsidence after the third slice, resulting from an increase in the mining range, is relatively small, and only the range experiencing the near-maximum subsidence increases. After the fourth mining cycle, an obvious "flat bottom" pattern appeared in the middle of the deflection curve.

Figures 7(b)–7(e) show that the subsidence range of the roof does not significantly change during the mining of the second slice to the fifth slice, but the shape of the deflection curve changes significantly relative to the first slice. During the mining of the second slice to the fifth slice, the shape of the roof deflection curve changes from asymmetry (the end of the first three cycles) to symmetry (the end of the fourth cycle), and the maximum subsidence of the roof increases with its position moving gradually from the left side to the middle. Similar to the first slice, after the third mining cycle, there is a clear "flat bottom" pattern in the middle of the deflection curve of the roof, and the maximum subsidence is nearly achieved as there are no longer significant increases in subsidence with increases in the mining range.

Figure 7(f) shows that the deflection curve of the roof during the mining process of the sixth slice is obviously different from other slices. The main reason is that the roof for this final slice is the sandstone stratum overlying the entire extra-thick coal seam, whereas during the mining of previous slices the roof was overlying slices of coal that would eventually be extracted. After the fourth mining cycle is completed, the "flat bottom" pattern in the middle of the roof deflection curve is not particularly obvious. From the first to the fourth mining cycle, the maximum subsidence of the roof occurring at the end of each cycle is 433.51 mm, 480.56 mm, 510.58 mm, and 514.57 mm, respectively.

3.3. Comparing Roof Movement Behavior during the Mining of Different Slices. In order to compare the roof movement

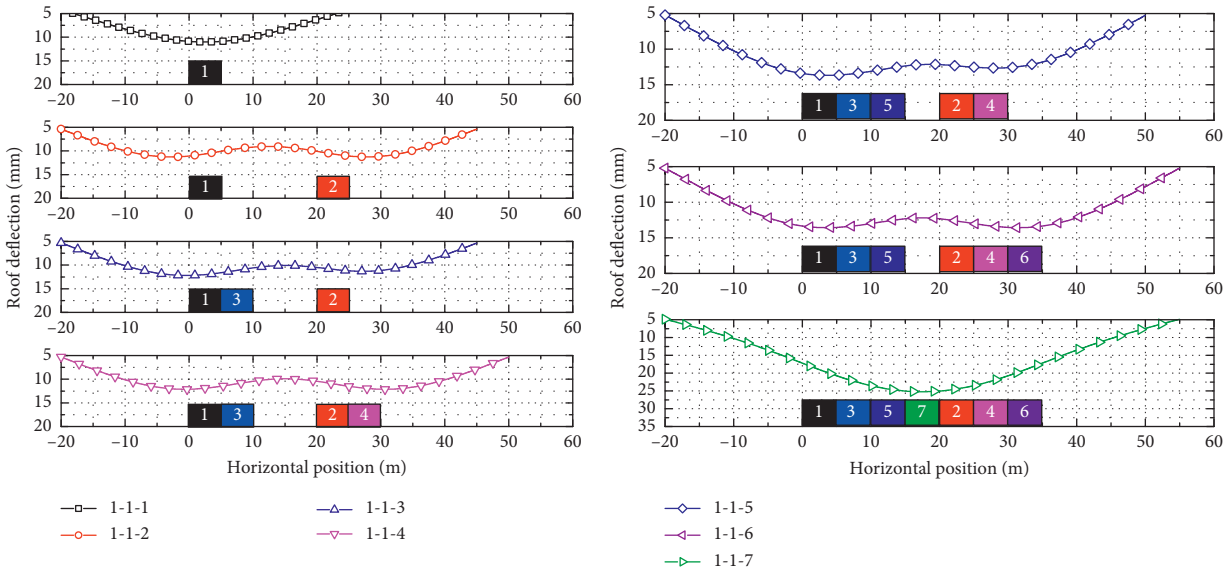

Figure 6: Deflection curves of the roof in the first mining cycle of the first slice. (a) 1-1-1~1-1-4 mining step and (b) 1-1-5~1-1-7 mining step.

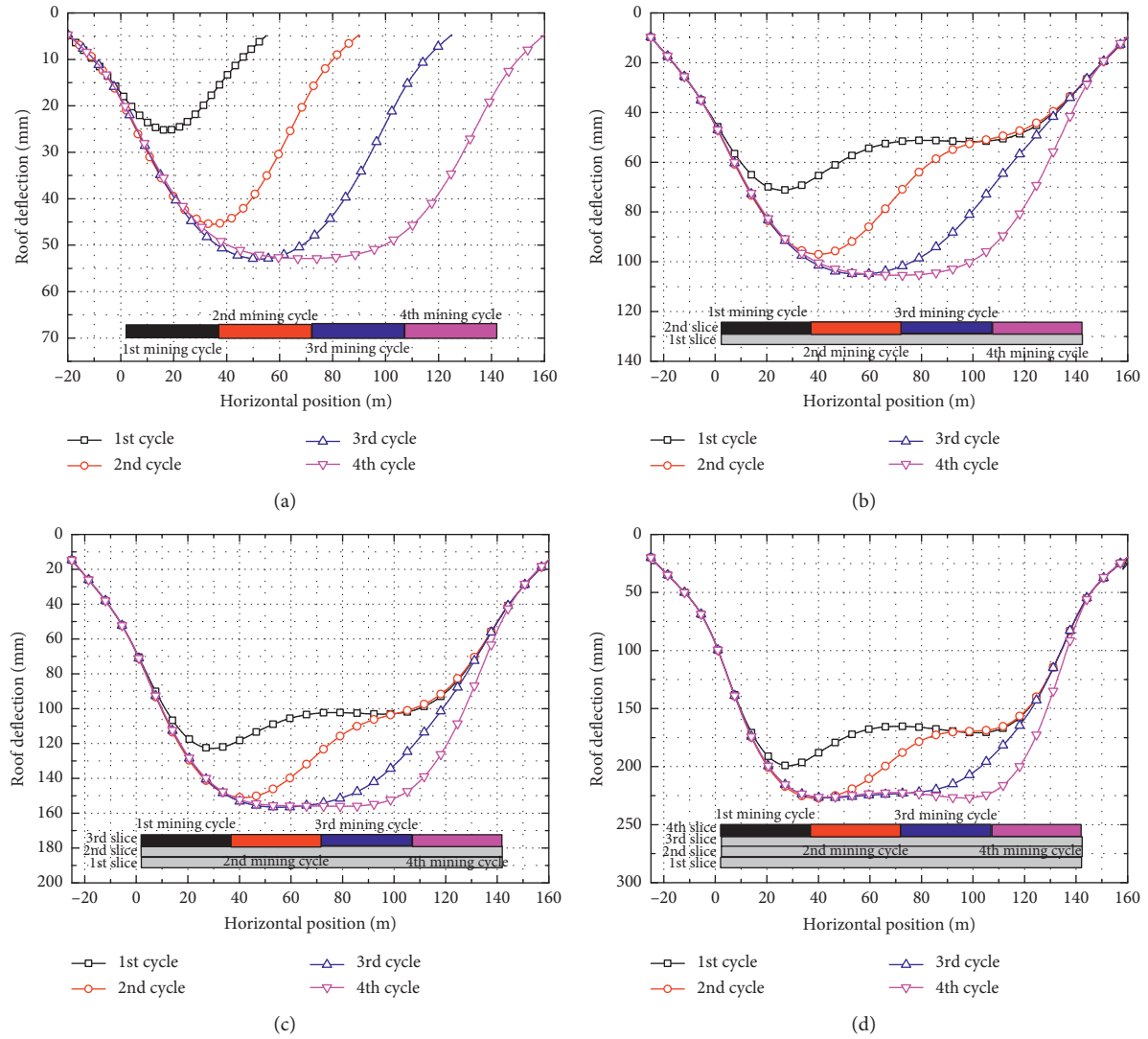

Figure 7: Continued.

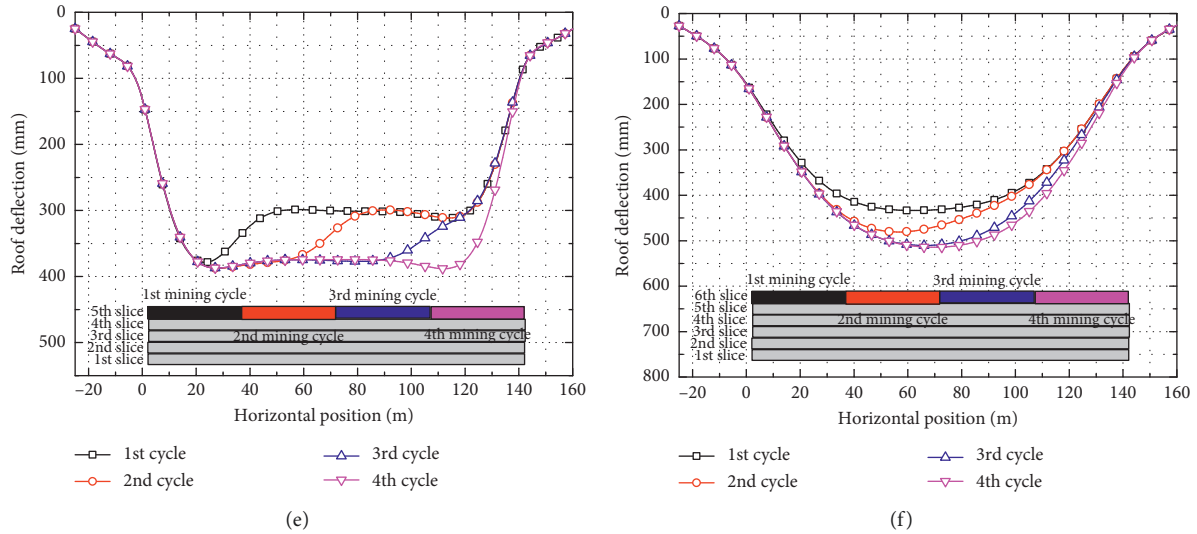

Figure 7: Deflection curves of the roof in different mining cycles of each slice: (a) first slice; (b) second slice; (c) third slice; (d) fourth slice; (e) fifth slice; (f) sixth slice.

behaviors seen when mining the different slices, the roof deflection curve during the sixth step in the first mining cycle is taken as a baseline example. It is compared with the roof deflection curves seen in the sixth step of subsequent slices. The results are plotted in Figure 8.

Figure 8 shows that, during the sixth step of the first mining cycle, the subsidence range of the first slice is much smaller than that of subsequent slices. An explanation is that mining the first slice is the initial disturbance to the stope, and mining subsequent slices are simply modifying an area that has already been disturbed with the roof being subjected to secondary and even numerous mining operations. The deflection curves of the roof in this sixth step of the first to fifth slices are bimodal curves, while it is a unimodal curve in the sixth slice. The reason for the occurrence of the bimodal curve is that there is a coal pillar in the middle of the mining range which can support the roof, but this supporting effect is relatively weaker during the mining of upper slices.

To compare the roof movement behavior of different slices during the mining process, the deflection curves of the roof after each mining cycle are calculated and plotted as shown in Figure 9.

Figure 9 shows that the deflection curve of the roof fluctuates less and is more symmetrical at the end of each mining cycle of the first and sixth slices, and the shape of the curve is noticeably different from other slices. The shape of the roof deflection curves is similar at the ends of each mining cycle of the second, third, fourth, and fifth slices, and as more slices are mined, increased roof subsidence is seen.

3.4. The Requirement of Backfill Performance to Prevent Roof Failure. The failure criteria of the roof are presented in Section 2.3. The allowable tensile stress and bending moment of the roof are different for each slice because of the different roof conditions in the mining process, as shown in Table 2.

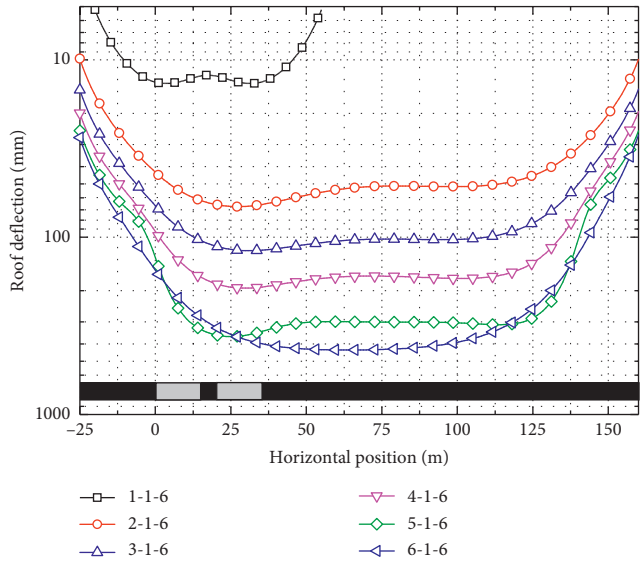

Figure 8: Deflection curves of the roof in the first to sixth mining step of each slice.

The elastic moduli for different types of backfilling materials are brought into the mechanical model to calculate the maximum bending moment of the roof during the mining process of each slice. Nonlinear regression is used to obtain a quantitative relationship between the elastic modulus of the backfilling material and the maximum bending moment of the roof for mining different slices. Combined with the allowable bending moment of the roof for each slice, the requirement for the elastic modulus of the backfilling material to ensure the roof does not break can be obtained. Then, the requirements for the strength of the backfilling material can be determined by measuring roof deflection and seeing when it reaches the critical failure state.

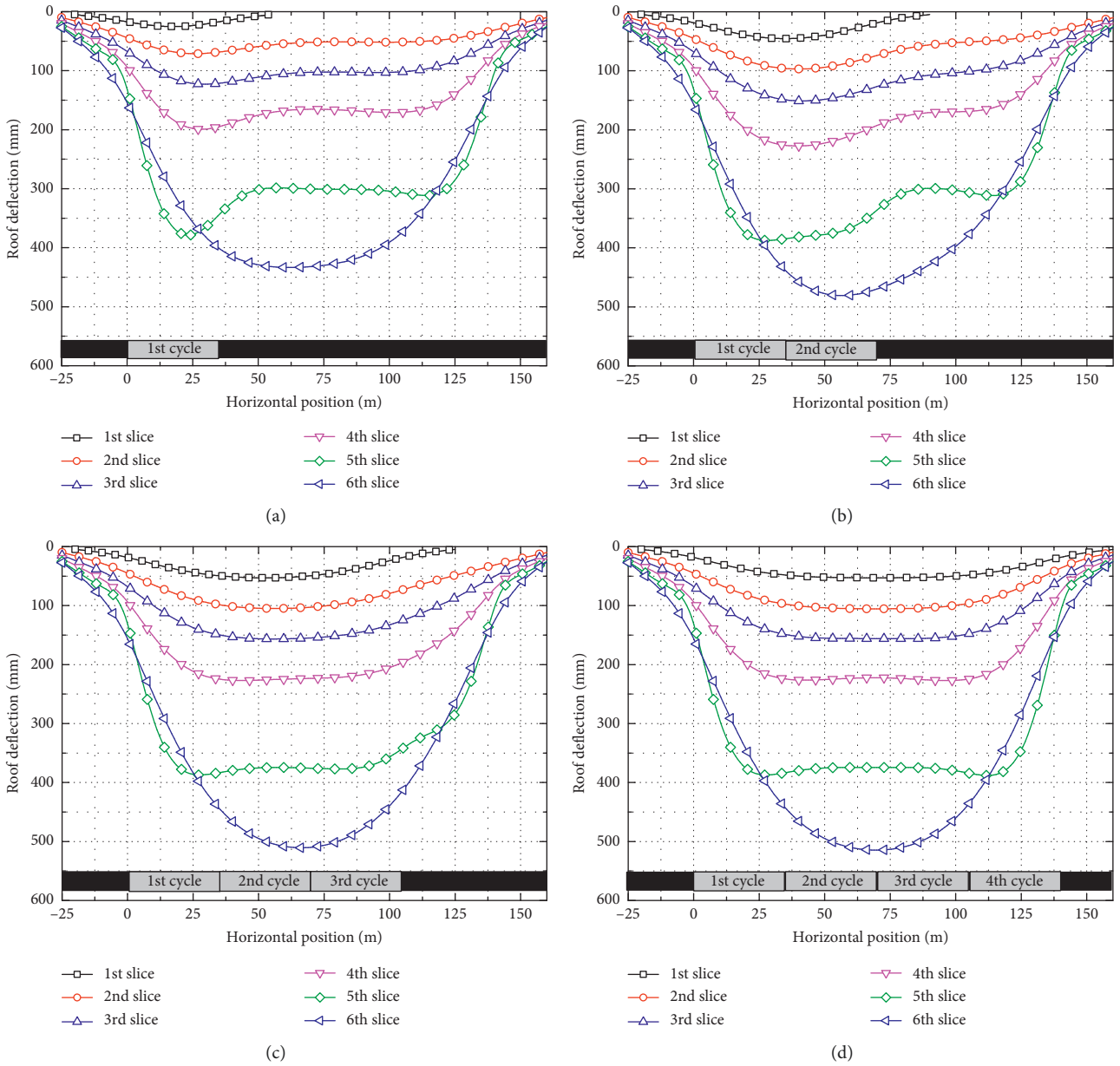

Figure 9: Deflection curves of the roof in different cycles during mining each slice: (a) first mining cycle; (b) second mining cycle; (c) third mining cycle; (d) fourth mining cycle.

Table 2: Allowable tensile stress and bending moment of the roof for different slices.

Slice number	1	2	3	4	5	6
Allowable tensile stress of the roof (MPa)	2.2	2.2	2.2	2.2	2.2	4
Allowable bending moment of the roof (N·m)	1.12*E*8	7.19*E*7	4.04*E*7	1.80*E*7	4.50*E*6	4.00*E*8

The results of determining the performance requirement of cemented backfill are shown in Figure 10.

Figure 10(a) shows that the quantitative relationship between the maximum bending moment of the roof and the elastic modulus of the backfilling material can be described effectively by the power function. As the elastic modulus of the backfilling material increases, the maximum bending moment of the roof shows an exponential decay. Due to the different conditions of the roof, the maximum bending moment of the roof during the sixth slice is obviously larger than that of the other slices with the same backfilling material.

Figure 10(b) shows that the elastic modulus requirement for the backfill material increases from 2.84 MPa to 29.44 MPa as the number of slices mined increases from 1 to 5, but the requirement drops to 1.86 MPa after the sixth slice is mined. The compressive strength requirement of the

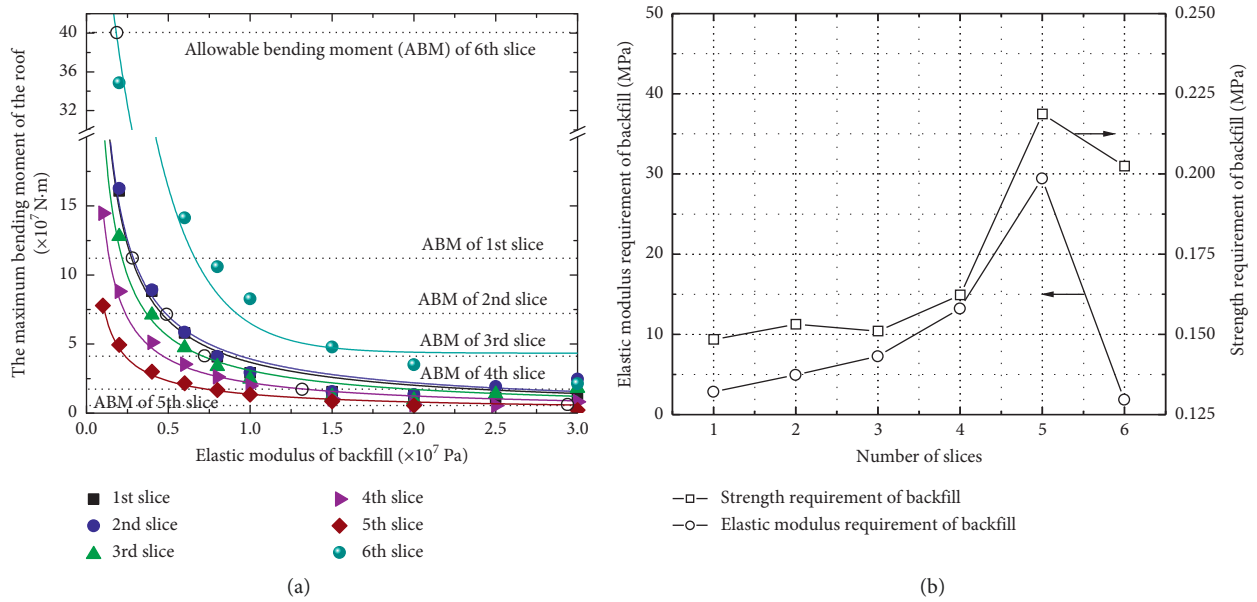

Figure 10: The performance requirement of cemented backfill: (a) the elastic modulus of backfill versus the maximum bending moment of the roof; (b) the elastic modulus and strength requirement of backfill for different slices.

backfill varies slightly within the range of 0.148 to 0.153 MPa when the first three slices are mined. However, the strength requirement rapidly increases to 0.219 MPa when the fifth slice is mined and decreases to 0.202 MPa when the sixth slice is mined. The significant change in backfill requirement for the sixth slice shown in the calculation results is due to the different roof conditions compared to other slices. In this case, of all the slices, it is the fifth slice that requires the strongest backfill material for mining the entire extra-thick coal seam with USLCB technology. The performance requirement of cemented backfill calculated by this model is the final condition, which means that the final strength and elastic modulus of the cemented backfill should meet this requirement theoretically. Taking into account the safety margins, the performance of the cemented backfill with a curing time of 7 days can be selected to meet this requirement for the industry application.

4. Conclusions

In this paper, a mechanical analysis approach is used to study roof movement and roof control in mining extra-thick coal seam using USLCB technology. The main findings and conclusions are as follows:

(1) In a single mining cycle of the first slice, the deflection curves of the roof can be divided into three types, i.e., the small range unimodal deflection curve in the initial step, the bimodal deflection curves of the middle steps with two active areas, and the large range unimodal deflection curve in the final step when the support pillar is removed. The shape of the curve is significantly affected by the mined area.

(2) All of the roof deflection curves that occur at the end of each mining cycle during the extraction of the first slice are symmetrical in their distribution. Also, there is an obvious "flat bottom" pattern occurring in the middle of the deflection curve after the fourth mining cycle is completed.

(3) During the mining of the second slice to the end of the fifth slice, the shape of the roof deflection curve changes from asymmetrical to symmetrical. After the third mining cycle is completed during the mining of these slices, there is a clear "flat bottom" pattern in the middle of the roof deflection curve. The roof movement during the mining of the top slice is noticeably different from roof movement during the mining of other slices. This difference is due to that the roof lithology of the top slice is different from previous slices whose immediate roof is actually the remaining coal seam.

(4) The relationship between the maximum bending moment of the roof and the elastic modulus of the backfilling material can be well described by the power function. The requirements of the backfill material's elastic modulus and strength increase as the number of mined slices increases from 1 to 5, but the requirements drop sharply when the sixth slice is mined.

Data Availability

The data used to support the findings of this study are included within the article.

Conflicts of Interest

The authors declare that they have no conflicts of interest.

Acknowledgments

This work was supported by the National Key R&D Program of China (Grant no. 2018YFC0604701), National Natural

Science Foundation of China (Youth Program) (Grant no. 51804308), the Research Fund of the State Key Laboratory of Coal Resources and Safe Mining, CUMT (Grant no. SKLCRSM18KF022), and the Natural Science Foundation of Heilongjiang Province of China (Grant no. LH2019E118). The authors would like to thank those researchers who have made great contributions to the project. Special thanks go to the Gonggeyingzi Coal Mine for providing everything for the field application studied in this research.

References

[1] A. Kesimal, E. Yilmaz, and B. Ercikdi, "Evaluation of paste backfill mixtures consisting of sulphide-rich mill tailings and varying cement contents," *Cement and Concrete Research*, vol. 34, no. 10, pp. 1817–1822, 2004.

[2] J. X. Zhang, X. J. Deng, X. Zhao, F. Ju, and B. Y. Li, "Effective control and performance measurement of solid waste backfill in coal mining," *International Journal of Mining, Reclamation and Environment*, vol. 31, no. 2, pp. 91–104, 2017.

[3] A. K. Ghose, "Underground methods of extraction of thick coal seams-a global survey," *Mining Science and Technology*, vol. 2, no. 1, pp. 17–32, 1984.

[4] B. Unver and N. E. Yasitli, "Modelling of strata movement with a special reference to caving mechanism in thick seam coal mining," *International Journal of Coal Geology*, vol. 66, no. 4, pp. 227–252, 2006.

[5] Y. Huang, J. Zhang, Q. Zhang, and S. Nie, "Backfilling technology of substituting waste and fly ash for coal underground in China coal mining area," *Environmental Engineering & Management Journal (EEMJ)*, vol. 10, 2011.

[6] X. Deng, J. Zhang, T. Kang, and X. Han, "Strata behavior in extra-thick coal seam mining with upward slicing backfilling technology," *International Journal of Mining Science and Technology*, vol. 26, no. 4, pp. 587–592, 2016.

[7] X. Deng, J. Zhang, B. Klein, N. Zhou, and B. deWit, "Experimental characterization of the influence of solid components on the rheological and mechanical properties of cemented paste backfill," *International Journal of Mineral Processing*, vol. 168, pp. 116–125, 2017.

[8] J. F. Archibald, J. L. Chew, and P. Lausch, "Use of ground waste glass and normal Portland cement mixtures for improving slurry and paste backfill support performance," *CIM Bulletin*, vol. 92, pp. 74–80, 1999.

[9] P. K. Senapati, B. K. Mishra, R. R. Barik, and D. P. Mohanty, "Evaluating the head loss of coal ash slurry pipelines at high solids concentrations using rheological data for mine backfilling," *Energy Sources, Part A: Recovery, Utilization, and Environmental Effects*, vol. 37, no. 14, pp. 1542–1549, 2015.

[10] L. Festugato, A. Fourie, and N. C. Consoli, "Cyclic shear response of fibre-reinforced cemented paste backfill," *Géotechnique Letters*, vol. 3, no. 1, pp. 5–12, 2013.

[11] E. Yilmaz, T. Belem, B. Bussière, M. Mbonimpa, and M. Benzaazoua, "Curing time effect on consolidation behaviour of cemented paste backfill containing different cement types and contents," *Construction and Building Materials*, vol. 75, pp. 99–111, 2015.

[12] A. Wu, Y. Wang, H. Wang, S. Yin, and X. Miao, "Coupled effects of cement type and water quality on the properties of cemented paste backfill," *International Journal of Mineral Processing*, vol. 143, pp. 65–71, 2015.

[13] B. D. Thompson, W. F. Bawden, and M. W. Grabinsky, "In situ measurements of cemented paste backfill at the Cayeli mine," *Canadian Geotechnical Journal*, vol. 49, no. 7, pp. 755–772, 2012.

[14] X. J. Deng, J. X. Zhang, N. Zhou, B. de Wit, and C. T. Wang, "Upward slicing longwall-roadway cemented backfilling technology for mining an extra-thick coal seam located under aquifers: a case study," *Environmental Earth Sciences*, vol. 76, no. 23, pp. 1–15, 2017.

[15] J. P. Doherty, A. Hasan, G. H. Suazo, and A. Fourie, "Investigation of some controllable factors that impact the stress state in cemented paste backfill," *Canadian Geotechnical Journal*, vol. 52, no. 12, pp. 1901–1912, 2015.

[16] F. Cihangir, B. Ercikdi, A. Kesimal, A. Turan, and H. Deveci, "Utilisation of alkali-activated blast furnace slag in paste backfill of high-sulphide mill tailings: effect of binder type and dosage," *Minerals Engineering*, vol. 30, pp. 33–43, 2012.

[17] M. Fall, M. Benzaazoua, and S. Ouellet, "Experimental characterization of the influence of tailings fineness and density on the quality of cemented paste backfill," *Minerals Engineering*, vol. 18, no. 1, pp. 41–44, 2005.

[18] A. Kesimai, E. Yilmaz, B. Ercikdi, I. Alp, M. Yumlu, and B. Ozdemir, "Laboratory testing of cemented paste backfill," *Madencilik*, vol. 41, no. 4, pp. 11–20, 2002.

[19] F. Sofrá and D. V. Boger, "Environmental rheology for waste minimisation in the minerals industry," *Chemical Engineering Journal*, vol. 86, no. 3, pp. 319–330, 2002.

[20] B. E. Wickland, G. W. Wilson, D. Wijewickreme, and B. Klein, "Design and evaluation of mixtures of mine waste rock and tailings," *Canadian Geotechnical Journal*, vol. 43, no. 9, pp. 928–945, 2006.

[21] P. K. Mandal, R. Singh, J. Maiti et al., "Underpinning-based simultaneous extraction of contiguous sections of a thick coal seam under weak and laminated parting," *International Journal of Rock Mechanics and Mining Sciences*, vol. 45, no. 1, pp. 11–28, 2008.

[22] J. Wang, B. Yu, H. Kang et al., "Key technologies and equipment for a fully mechanized top-coal caving operation with a large mining height at ultra-thick coal seams," *International Journal of Coal Science & Technology*, vol. 2, no. 2, pp. 97–161, 2015.

[23] A. Vakili and B. K. Hebblewhite, "A new cavability assessment criterion for longwall top coal caving," *International Journal of Rock Mechanics and Mining Sciences*, vol. 47, no. 8, pp. 1317–1329, 2010.

[24] G. X. Xie, J. C. Chang, and K. Yang, "Investigations into stress shell characteristics of surrounding rock in fully mechanized top-coal caving face," *International Journal of Rock Mechanics and Mining Sciences*, vol. 46, no. 1, pp. 172–181, 2009.

[25] M. R. Islam, D. Hayashi, and A. B. M. Kamruzzaman, "Finite element modeling of stress distributions and problems for multi-slice longwall mining in Bangladesh, with special reference to the Barapukuria coal mine," *International Journal of Coal Geology*, vol. 78, no. 2, pp. 91–109, 2009.

[26] A. Majdi, F. P. Hassani, and M. Y. Nasiri, "Prediction of the height of destressed zone above the mined panel roof in longwall coal mining," *International Journal of Coal Geology*, vol. 98, pp. 62–72, 2012.

[27] X. Deng, B. Klein, L. Tong, and B. de Wit, "Experimental study on the rheological behavior of ultra-fine cemented backfill," *Construction and Building Materials*, vol. 158, pp. 985–994, 2018.

[28] Y. He, Q. Chen, C. Qi, Q. Zhang, and C. Xiao, "Lithium slag and fly ash-based binder for cemented fine tailings backfill," *Journal of Environmental Management*, vol. 248, Article ID 109282, 2019.

[29] Y. Liu, Q. Zhang, Q. Chen, C. Qi, Z. Su, and Z. Huang, "Utilisation of water-washing pre-treated phosphogypsum for cemented paste backfill," *Minerals*, vol. 9, no. 3, p. 175, 2019.

[30] X. J. Deng, B. Klein, D. J. Hallbom, B. de Wit, and J. X. Zhang, "Influence of particle size on the basic and time-dependent rheological behaviors of cemented paste backfill," *Journal of Materials Engineering and Performance*, vol. 27, no. 7, pp. 3478–3487, 2018.

[31] X. J. Deng, B. Klein, J. X. Zhang, D. Hallbom, and B. de Wit, "Time-dependent rheological behaviour of cemented backfill mixture," *International Journal of Mining, Reclamation and Environment*, vol. 32, no. 3, pp. 145–162, 2018.

[32] Y. Feng, J. Kero, Q. Yang et al., "Mechanical activation of granulated copper slag and its influence on hydration heat and compressive strength of blended cement," *Materials*, vol. 12, no. 5, p. 772, 2019.

[33] Y. Feng, Q. Yang, Q. Chen et al., "Characterization and evaluation of the pozzolanic activity of granulated copper slag modified with CaO," *Journal of Cleaner Production*, vol. 232, pp. 1112–1120, 2019.

[34] M. Li, J. Zhang, and R. Gao, "Mechanical analysis of roof subsidence based on rheological properties of solid backfill materials," *Tehnicki Vjesnik—Technical Gazette*, vol. 25, no. 1, pp. 152–157, 2018.

[35] Q. Guo, G. Guo, X. Lv, W. Zhang, Y. Lin, and S. Qin, "Strata movement and surface subsidence prediction model of dense solid backfilling mining," *Environmental Earth Sciences*, vol. 75, no. 21, 2016.

[36] A. Vervoort, "Surface movement above an underground coal longwall mine after closure," *Natural Hazards and Earth System Sciences Discussions*, vol. 16, no. 9, pp. 2107–2121, 2016.

[37] V. Kajzar, R. Kukutsch, P. Waclawik, and J. Nemcik, "Innovative approach to monitoring coal pillar deformation and roof movement using 3D laser technology," *Procedia Engineering*, vol. 191, pp. 873–879, 2017.

[38] J. Ning, J. Wang, L. Jiang, N. Jiang, X. Liu, and J. Jiang, "Fracture analysis of double-layer hard and thick roof and the controlling effect on strata behavior: a case study," *Engineering Failure Analysis*, vol. 81, pp. 117–134, 2017.

[39] G. Song and S. Yang, "Investigation into strata behaviour and fractured zone height in a high-seam longwall coal mine," *Journal of the Southern African Institute of Mining and Metallurgy*, vol. 115, no. 8, pp. 781–788, 2015.

Hindawi
Advances in Materials Science and Engineering
Volume 2019, Article ID 3574190, 10 pages
https://doi.org/10.1155/2019/3574190

Research Article

A Novel Prediction Model of Strength of Paste Backfill Prepared from Waste-Unclassified Tailings

Haiyong Cheng,[1,2] Shunchuan Wu,[1] Xiaoqiang Zhang ,[1] and Junhong Li[1]

[1]*Kunming University of Science and Technology, Faculty of Land Resources Engineering, Kunming 650093, China*
[2]*Key Laboratory of Ministry of Education of China for Efficient Mining and Safety of Metal Mines, Beijing 100083, China*

Correspondence should be addressed to Xiaoqiang Zhang; xiaoqiangzhang@cqu.edu.cn

Received 30 August 2019; Revised 8 October 2019; Accepted 14 October 2019; Published 31 October 2019

Guest Editor: Chongchong Qi

Paste backfilling is an important support for the development of green mines and deep mining. It can effectively reduce a series of risks of underground goaf and surface tailings ponds. Reasonable strength of backfill is an effective guarantee for controlling ground stress and realizing safe mining function. Under the combination of complex materials and local conditions, ensuring the optimal design and effective proportion for paste backfill strength is the bottleneck problem that restricts the safety, economy, and efficiency of filling mining. The strength developing trend of paste backfilling prepared from waste rock and unclassified tailings has been studied. Different levels of cement contents, tailings-waste ratios, and slurry concentrations were investigated through orthogonal design to obtain the relationship between the *UCS* and the multi-influential factors. Combined with the experimental results and the previous strength prediction models, the waste rock-unclassified tailings paste strength prediction model was proposed. Introducing the water-cement ratio, the cement-tailings ratio, the amount of cement, and the packing density that characterizing the overall gradation of unclassified tailings and waste rock, as well as the curing time, a strength prediction model of multifactors was developed. Moreover, the microscopic structure of the paste prepared from waste-unclassified tailings was analyzed with an Environment Scanning Electron Microscope (ESEM), and the influence mechanism was ascertained. The weight coefficient of strength development is carded in this paper, and the strength model of unclassified tailings-waste paste considering five factors is obtained, which is of great significance to guide the mining engineering.

1. Introduction

In many countries, paste backfill mining technology is an important method for dealing with mine wastes and thus is widely recognized as a green and new technology in twenty-first century [1]. Paste backfill, without segregation and dewatering, also has flow ability [2], which is mainly composed of three parts, namely, unclassified tailings, cemented materials, and water. Unclassified tailings, containing a certain proportion of fine particles [3, 4], has a large surface area [5, 6], thus leading to a strong water saturation performance [7]. Therefore, the paste slurry possesses good plasticity properties and easy for transmission [8]. The C-S-H generated from the hydration of binders encapsulates the tailings particles, facilitating the condensation and hardening of paste slurry [9, 10].

Qi and Fourie [11] summarized recent progress in CPB design, with particular emphasis on flocculation and sedimentation, CPB mix design and CPB pipe transport, and envisaged a future in which the CPB design is optimized in an integrated CPB design system, accelerated by artificial intelligence and interpreted using atomic simulation. Qi [12–14] proposed a strength prediction model integrating boosted regression trees (BRT) and particle swarm optimization (PSO) and thought that more efficient reuse of waste tailings as CPB can be achieved by reducing the required number of mechanical experiments during engineering applications. At the same time, an intelligent modelling framework for the mechanical properties prediction using machine learning (ML) algorithms and genetic algorithm (GA) was proposed [15–17]. Lu et al. [18]

improved a method to estimate the unconfined compressive strength of CPB. The strength of paste is usually determined mainly on the demand of the adopted mining technology. Buck believed that it was more important to consider the impact of water-cement ratio on the strength of concrete [19, 20]. Under the same water-cement ratio, the compressive strength of recycled concrete declined about 8 Mpa than the ordinary concrete [21], but the same strength could be reached by reducing water-cement ratio. Rashad and Zeedan deemed that the compressive strength of all pastes increased with the increase in hydration time. In the initial 3~7 days, the strength growth rate was high while the strength showed a linear increase after 7 days [22].

Swan considered that the strength was closely related to the cement content, so he introduced the "cementation coefficient" and established the Swan model. However, this model is often unable to be accurately calculated because it is difficult to obtain its parameters. Adding waste rock aggregates makes the relationship between paste strength and its materials more complex [12, 23]. The traditional strength forecasting model is generally based on a fine granularity and good homogeneity of paste tailings [24], so the waste particles of a few millimeters and even 10 mm do not apply to this model. The forecasted strength is often determined according to rich experience or numerous experiments; at the same time, the strength formation mechanism of paste prepared from waste-unclassified tailings still needs some further research [25].

The present work is to identify the factors influencing the strength of paste prepared from waste-unclassified tailings via a series of tests and then to determine their effects on the strength by regression analysis. On the basis of the existed strength model as well as the compactness theory and with the analysis results, a paste strength prediction model applied to waste-unclassified tailings is developed.

2. Materials and Methods

The materials used mainly include unclassified tailings, waste rock, and cement, all of which were collected from the No. 2 mine area of Jinchuan Group in western China. The Jinchuan Nickel Deposit is located in Jinchang City, Gansu province in western China. In 1958, the amount of nickel metal reached 5.57 million tons, accounting for 79% of China's proven reserves, which is the largest copper nickel sulfide deposit in China and the third in the world. The deposit is famous for its thick ore body, deep burial, rock fragmentation, and high in-situ stress. It is a large complex and difficult underground deposit that is rarely seen worldwide. Before starting the experiment, materials were dried in an oven at 105°C for 12 hours. The materials were mixed with tap water to make a certain concentration of slurry paste for a series of tests.

2.1. Basic Physical and Chemical Properties. Tailing samples were collected from the underflow of an ordinary thickener in the processing plant. After outdoor drying, the density of the tailings was measured via pycnometer method, and the bulk density was measured by compacting density tube. The cement used is 32.5 ordinary Portland cement provided by Jinchang cement plant. The results are shown in Table 1.

Chemical compositions of the tailings, waste rock, and cement were analyzed by using X-ray diffraction and chemical element calibration method, as shown in Table 2.

Particle size distribution of the unclassified tailings and waste rocks is shown in Figure 1. As shown in Figure 1, the content of −200 mesh particles is 88.73%, and the $-20\,\mu$m particles account for 47%, which means the overall particle size is a little fine, while waste rocks, with −200 mesh particles accounting for 20.12% and $-20\,\mu$m particles accounting for 13.1%, are mainly coarse particles. It can be summarized from the composition of material particles that any of the materials cannot meet the requirements of the amount of $-20\,\mu$m particles [9, 26]; thus, the two kinds of materials are needed to be mixed at a certain proportion.

2.2. Experiment Preparation. In order to consider the influence of multifactors on the strength development, orthogonal method was taken for the design of the experiments, of which the results could be analyzed by range analysis, variance analysis, and regression analysis. The factors taken into consideration included the waste content, tailings content, cement proportion, and slurry concentration. In total, 16 groups of specimens were prepared in $70.7 \times 70.7 \times 70.7$ mm molds and then maintained in a curing container with the temperature set at 20°C and the humidity at 90% in accordance with the underground conditions. The two smooth sides of the specimen were used to measure its 3 days, 7 days, and 28 days uniaxial compressive strength. The preparation of the specimen is shown in Table 3. Through a large number of experiments in the early stage, it is concluded that the cement content, paste concentration, and tailings-waste ratio are important factors affecting the paste strength, and other parameters can be derived from these basic parameters or be idealized as secondary factors [11, 27]. The proportion is based on previous exploratory experiments and slump tests with slump values ranging from 23 to 26, which are of good fluidity and stability. At the same time, the engineering application is also referred. Under the condition of low concentration, excessive waste rock content or larger waste particles can easily lead to serious segregation. However, if the maximum particle size of waste is less than 10 mm with high concentration, the segregation rate of slurry can be controlled within 5%~15%.

2.3. Experiments. The density of mixtures of different proportions of unclassified tailings and waste rock was measured and packing density under different proportions was obtained by compaction experiment in a copper cylinder [28]. Slump test was carried out to test the slurry flow ability and to observe its viscosity and water saturation property directly. Generally, a slump of approximately 23~26 cm can meet the requirements of paste pipeline transportation [29, 30]. Besides, because of simplicity and reliability, the unconfined compressive strength (*UCS*) test

Table 1: Physical properties of the materials.

Type of material	Density (t/m^3)	Bulk density (t/m^3)	Porosity (%)
Tailings	2.85	1.55	45.61
Waste	2.81	1.84	34.52
Cement	3.1	1.1	64.52

Table 2: Chemical compositions and some physical properties of the materials.

Materials	SiO_2	Al_2O_3	Fe_2O_3	CaO	MgO	S	Ni	Cu	Others
Tailings (%)	36.41	7.77	9.9	3.09	27.79	1.63	0.28	0.2	12.93
Waste (%)	70.5	12.1	4.5	2.4	0.9	0.2	—	—	9.4
Cement (%)	21.5	4.5	2	63.5	4.0	2.5	—	—	2

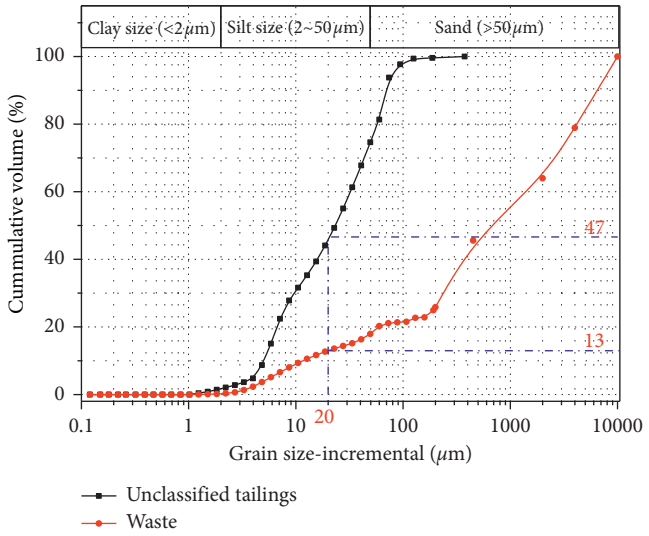

Figure 1: Grain size distribution (GSD) curves of the unclassified tailings compared to a typical range of GSD curves of waste.

was used to investigate the mechanical properties of the paste backfill samples [31]. In order to obtain the strength of 3, 7, and 28 days, all of the experiments were prepared and tested in triplicate, and the mean values of the *UCS* were presented in the results. The experimental process and samples are shown in Figure 2.

3. Results and Discussion

As orthogonal design was used in the experiments, to study the influence of multiple factors on the strength development, the experiment results needed to be processed by statistical analysis. Water-cement ratio $W/C = (M_{water} + M_{binder})$ and binder' ratio $B/(T+S) = (M_{binder}/(M_{tailings} + M_{waste}))$ were calculated.

3.1. Relationship between UCS Development and Concentration. The relationship between uniaxial compressive strength and weight concentration was obtained by regression analysis [32]. Figure 3 shows the 28-day strength of the CPB samples consisting of different content of materials. In the graph, it can be seen that the increase in cement content has a noticeable beneficial effect on the growth of uniaxial compressive strength. In Figure 3(a), when the cement content rises from 240 kg/m^3 to 300 kg/m^3, the strength increases 79.1%, from 4.01 MPa to 7.18 MPa at a concentration of 78%, while at the concentration of 81%, the strength increases from 4.74 MPa to 7.6 MPa, a growth of 60.3%. The gap caused by adding different proportion of cement reduces, which reveals that increasing the concentration at a certain extent will reduce the effect of cement, or in some other words, a smaller amount of cement is needed.

Table 3: Scheme of experiment $L_{16}(4^3)$.

CPB sample no.	Binder (kg/m^3)	Concentration (%)	Tailings-waste ratio (T/S)
1	240	78	3 : 7
2	260	79	4 : 6
3	280	80	5 : 5
4	300	81	6 : 4

3.2. Relationship between UCS and Water-Cement Ratio. Water-cement ratio $W/C = (M_{water} + M_{binder})$ refers to the proportion of water to cement in per volume unit of slurry [33]. Water in paste slurry not only involves the hydration reaction with cement but also lubricates slurry, equipping the paste with good fluidity [20]. In Figure 4, it can be seen that generally, the uniaxial compressive strength gradually decreases with an increase in the water-cement ratio. By using regression analysis, the change trend was figured out to be a basically negative exponential growth. The correlation coefficient of the regression curve is between 0.864 and 0.963 and the credibility is high. Meanwhile, although different tailings-waste ratio has a certain different effect on the strength of CPB samples, the overall trend is similar.

3.3. Relationship between UCS and the Binder Content. Binder content $B/(T+S) = (M_{binder}/(M_{tailings} + M_{waste}))$ indicates the relation between cement and aggregates and also the capacity owned by the binder to enclose the aggregates and to make them stick together [34]. Figure 5 reveals the relationship between the 28-day *UCS* and the binder content. In Figure 5(a), it can be seen that at the same weight concentration but different tailings-waste ratios, the *UCS* basically rises with the increase in binder content. Through regression analysis, the developing trend is

(a) (b) (c)

Figure 2: *UCS* tests and experimental samples. (a) *UCS* tests. (b) Tailings sample. (c) Waste sample.

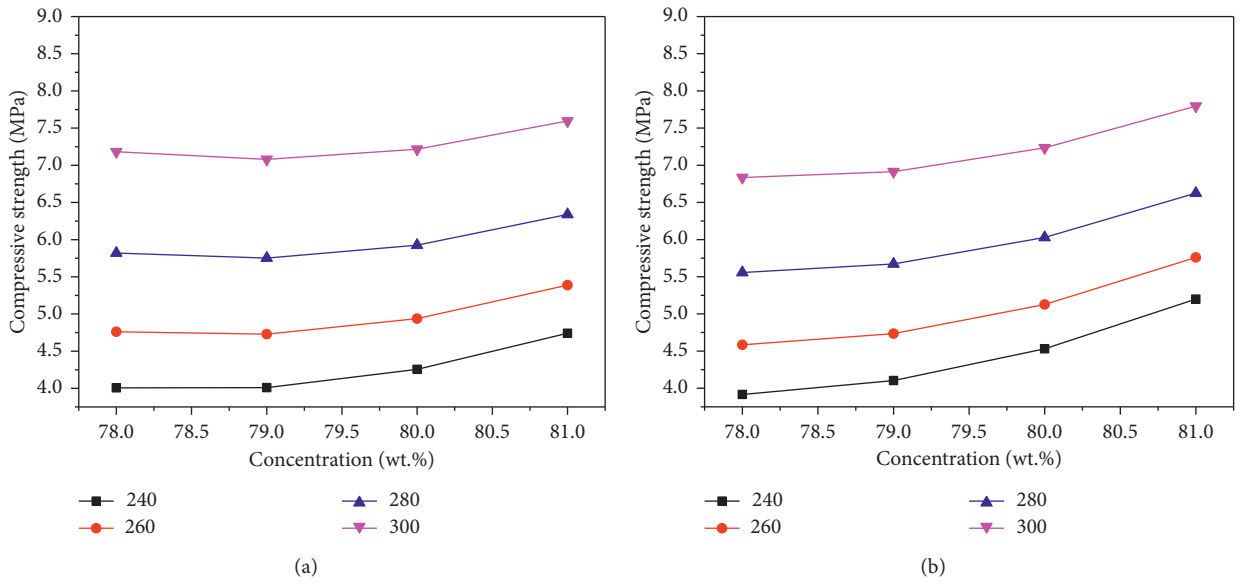

Figure 3: Change in normalized *UCS* with weight concentration for all CPB samples. (a) Tailings-waste ratio 3 : 7. (b) Tailings-waste ratio 4 : 6.

basically like an exponential growth. In contrast n, Figure 5(b) shows that under the same tailings-waste ratio but different concentrations, the *UCS* also have a significant exponential growth with the increase in the binder content.

3.4. Relationship between UCS and the Packing Density. In the tests, different proportions of unclassified tailings and waste rock were mixed to obtain a series of aggregate densities (Figure 6(a)). The packing density was 0.66, when the aggregate was totally waste rock, while it gradually increased with the rising of the amount of unclassified tailings, and finally reached a maximum value of around 0.69 when the waste to tailings ratio was nearly 3 : 7. Figure 6(b) shows the change law of *UCS* at the 28th day to the tailings-waste ratio, with the paste concentration being 79 wt.% and the amount of cement being 280 kg/m^3. When the tailings-waste ratio is 7 : 3, the 28-day *UCS* was the maximum while it was the minimum when there was only tailings in the CPB samples. From the analysis results of the relationship between the packing density and *UCS*, we found a typical function relationship between them, as shown in Figure 6(c). The packing density not only reflects the porosity of the materials, but also has a certain relationship with the particle size of the aggregates. The higher the packing density, the better the proportioning of coarse and fine particles. The stable structure was formed by coarse and fine grain mosaic, which forms the foundation of strength.

3.5. Relationship between UCS and the Curing Time. Figure 7(a) shows the changes of the *UCS* with the curing time when the cement content was 260 kg/m^3 and the tailings-waste ratio was 4 : 6. The *UCS* value increased rapidly during the initial 3~7 days. During this period, the cement involved in an early hardening stage, and by the end of this stage, the hardening reaction completed almost about 38%~55%. In the following curing stage, the hardening reaction continued, but the growth rate of the *UCS* gradually slowed down, and by the end of the 28th day, the hardening process reached about 70%~80%, so the 28-day strength represents the long-term strength in actual production. In contrast, when the concentration was 79 wt.% and the tailings-waste ratio was 3 : 7, the changes of the *UCS* to the curing time is shown in Figure 7(b). The growth rate, from

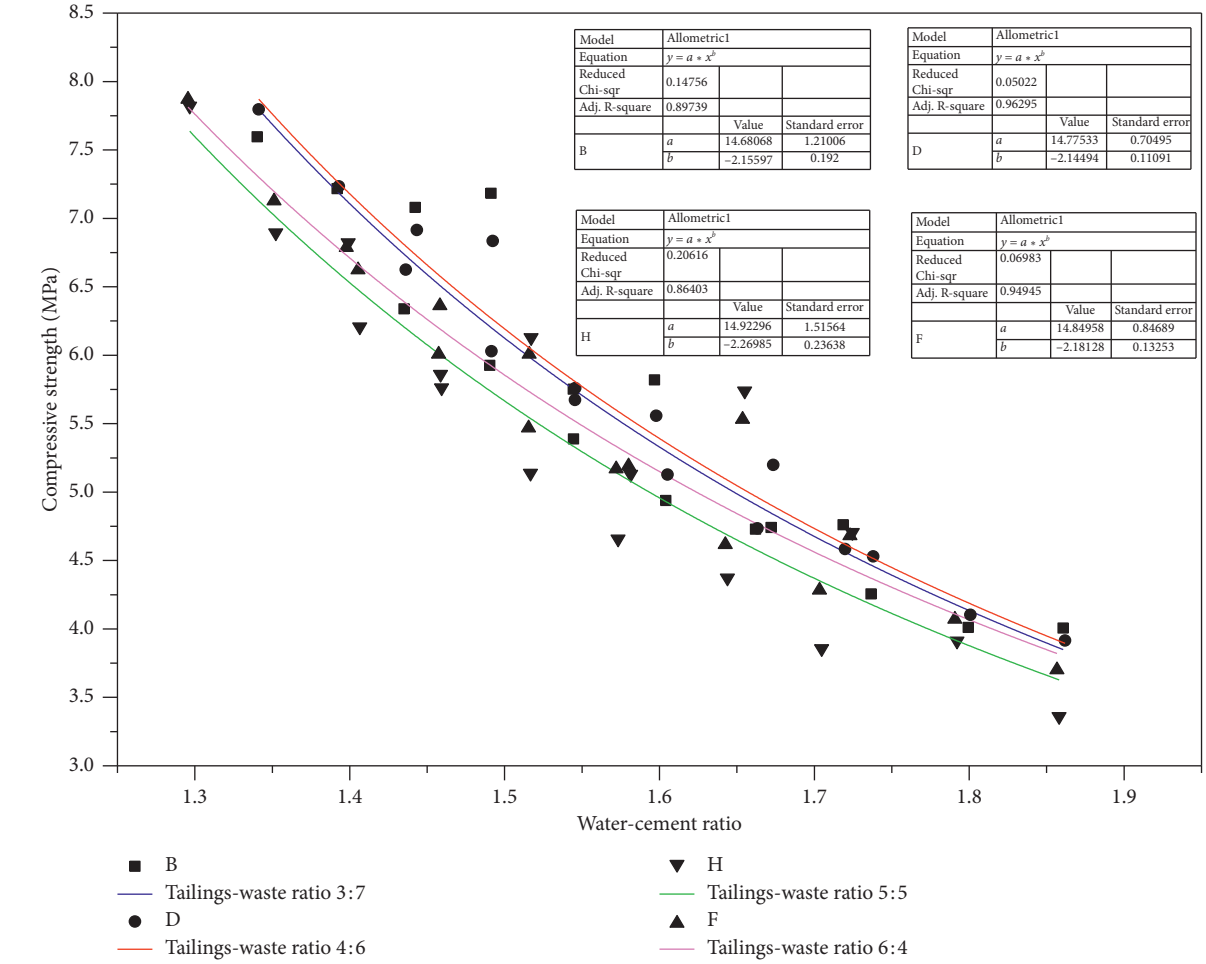

Figure 4: Relationship between normalized *UCS* and water-cement ratio.

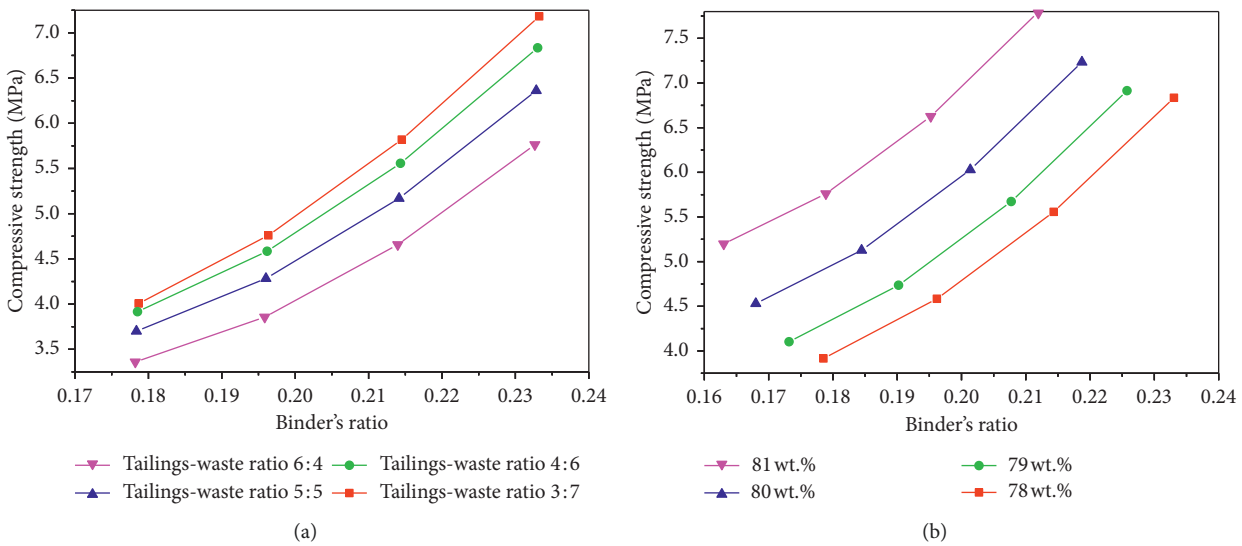

Figure 5: Relationship between *UCS* and binder content for CPB samples. (a) Concentration 78 wt.%. (b) Tailings-waste ratio 4 : 6.

27% at the 7th day to 76% at the 28th day, was significant. It was found from the regression analysis that the *UCS* of the paste backfill samples had a logarithmic increase to the curing time, and this feature was generally discovered when the CPB samples are at different concentrations and cement contents.

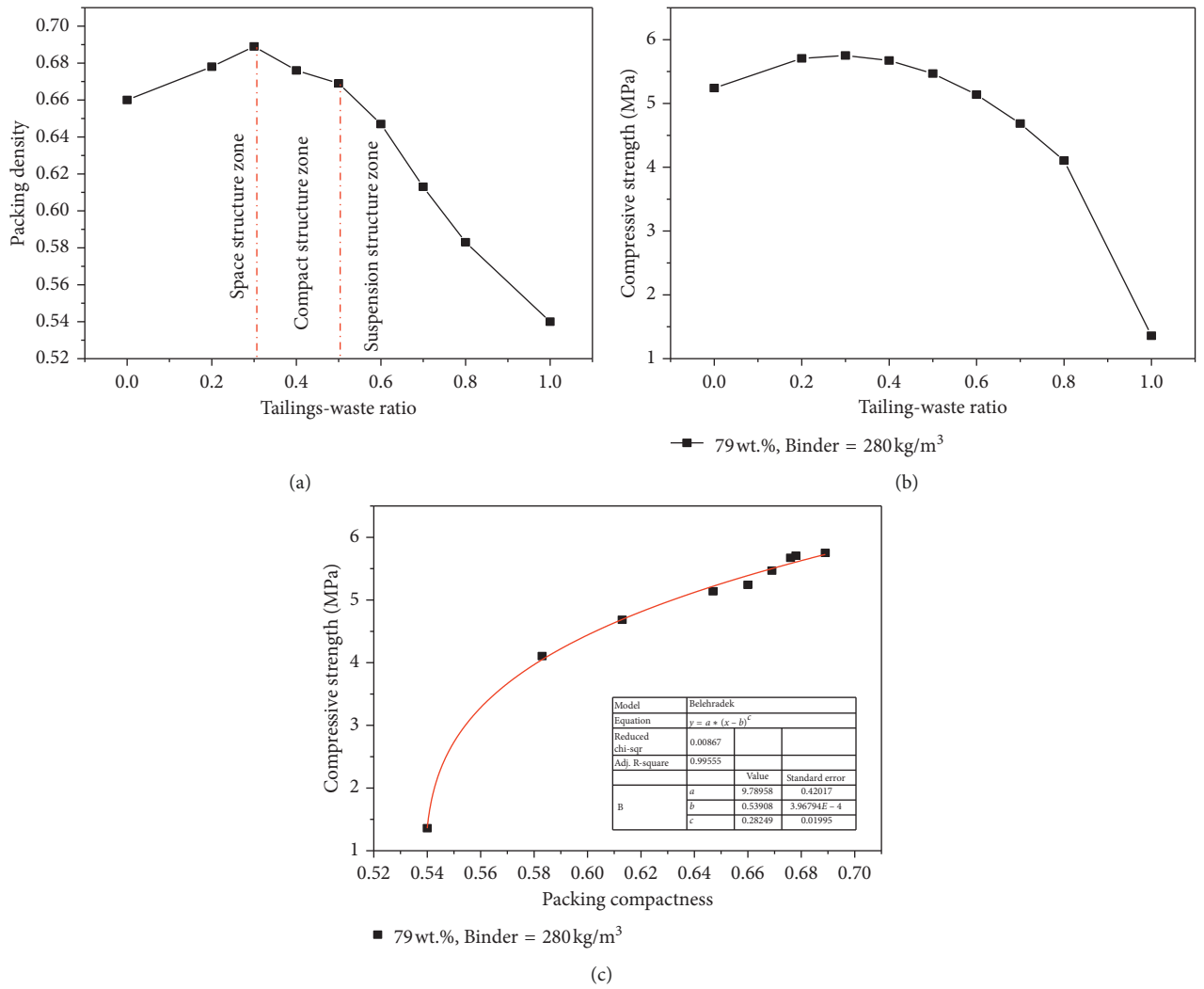

FIGURE 6: Packing-density analysis. (a) Relationship between tailings-waste ratio and packing density. (b) Tailings-waste ratio and the strength in the 28th day. (c) Relationship between density and strength.

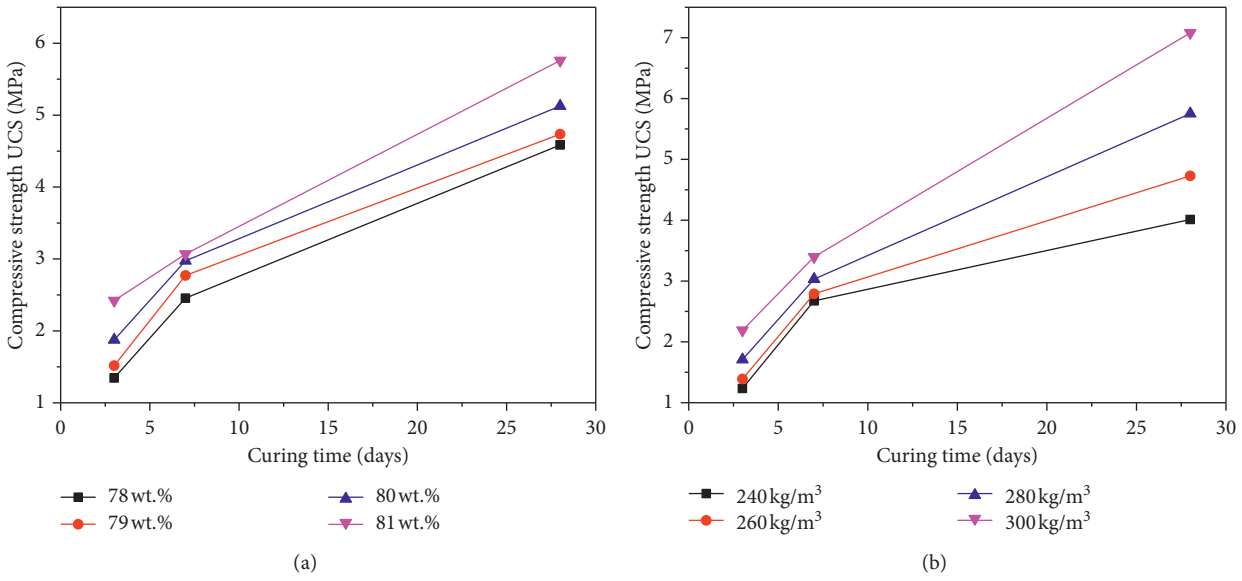

FIGURE 7: The relationship between uniaxial compressive strength and curing time. (a) Cement content was 260 kg/m^3 and the tailings-waste ratio was 4 : 6. (b) Concentration 79 wt.% and the tailings-waste ratio was 3 : 7.

Based on the comprehensive analysis of various factors affecting the strength development of backfill, it is concluded that the cement content has the most significant influence on the early strength and long-term strength, the concentration secondary, and then the tailings-waste ratio has a certain influence on the strength development. The analysis of strength influencing factors and their relation, as well as the study of strength model, are instructive.

4. Strength Prediction Model

4.1. Analysis of the Present Prediction Model. The filling body is a product that is prepared artificially from different proportions of materials, and naturally the strength development is influenced not only by the preparation proportions but also by the intrinsic properties of the materials [35, 36]. In other words, it reflects that there is some inevitable correlation between the strength development and the two factors mentioned above. In the past many years of research in backfilling technology, some scholars have already discussed the strength prediction model of the filling body [37].

From the results of experimental study, Mitchell considered that there was a power function correlation between the compressive strength of the filling body and the water-cement ratio as well as the porosity. And it was also related to the proportion of the cementing agent, as shown in the formula below [38]:

$$R_{UCS} = aC^m\left(N^{-n}W^{-k} + b\right), \tag{1}$$

where R_{UCS} is the unconfined compressive strength, MPa; C is the content of the cementing agent, t/m^3; N is the porosity, %; W is the water-cement ratio; and a and b are experimental constants.

Swan thought the unconfined compressive strength of the filling body was related to the content of the cementing agent, where C_y was used to represent the volume content of cementing agent. At the same time, a certain relation existed between the *UCS* of the filling body and the specific surface area of tailings a_p and the free distance of particles in slurry d_{avg}. It can be shown in the following formula:

$$R_{UCS} = 0.283\left(\frac{C_v}{d_{avg}a_p}\right)^{2.36}. \tag{2}$$

How to measure the distance between particles is essential for this model, but it is of operational difficulty for the calculation of this kind of parameters. Arioglu proposed a formula to predict the *UCS* by studying the cohesive force and water-cement ratio of the backfill slurry:

$$\begin{aligned} R_{UCS} &= a \times \alpha^{-n}, \\ C &= bR_{UCS} + c, \end{aligned} \tag{3}$$

where α is the water-cement ratio; C is the cohesive force; and a, b, and c are experimental constants. Traditionally, the studies on prediction model of strength were mainly focused on the effect of water-cement ratio on the strength development or the effects of cement content or porosity. Therefore, those empirical formulas were mostly based on the unclassified tailings and cement, without considering the effect of waste rock and other large particles. Besides, the curing time and some other important factors were not involved in those models. Different mining technology determines different exposure period of the filling body [39]. For instance, the layering mining method emphasizes the short-term strength of 3 to 7 days, while the subsequently fill mining method pays more attention to the strength of 28 days or longer periods. If the effect of curing time on the strength could be definitely understood and the function of the curing time to the *UCS* could be given, then it will be of significant importance for a well-coordinated schedule of both backfilling and mining.

4.2. Development of a New Prediction Model. By analyzing the effects of multifactors on the strength of CPB samples, it could be concluded that with the water-cement ratio increasing, the *UCS* of CPB samples presented a power-exponential growth. The same growth trend also occurred when the influence factor was binder' ratio. The packing density of aggregates consisting of different proportions of unclassified tailings and waste rock, to some extent, reflects their effects on the strength of paste samples. Through analysis, we could see that the *UCS* of the paste basically presented a logarithmic growth with curing days increasing. At the same time, the content of cementing agent had a positive correlation with the *UCS*. According to the researches and analyses mentioned above, the prediction model of the strength of CPB prepared from waste-unclassified tailings was presented in this paper:

$$R_{UCS} = \alpha \times B \times Ln\,D \times \Phi^m \times \left(\frac{W}{C}\right)^n \times \left(\frac{C}{A}\right)^k, \tag{4}$$

where B is the content of cement, t/m^3; D is the curing time; Φ is the aggregate packing density; W/C is the water-cement ratio; C/A is the binder's ratio; and α, n, and k are experimental constant. Model parameters need to be regressed according to the material properties and experimental conditions. The model is suitable for the prediction of paste strength from the combination of unclassified tailings and waste of which the five factors are taken into account.

In order to obtain the experimental constants of this model, the parameters used in the experiments were carried into this model to conduct some fitting analysis. The results were shown as follows:

$$R_{UCS} = 4.8614 \times B \times Ln\,D \times \Phi^{0.5894} \times \left(\frac{W}{C}\right)^{-1.7519} \times \left(\frac{C}{A}\right)^{-0.7645}. \tag{5}$$

Adj. R-square = 0.93, $F = 3371.0383 > F_{0.01}(4, 188) = 3.42$.

From formula (5), it can be seen that several influence factors are already involved in this prediction model, and the test parameters also have good adaptability. This new strength model is more applicable for predicting the *UCS* of CPB samples consisting of waste-unclassified tailings.

Table 4: Proportions of materials and strength results.

No.	Binder (t/m^3)	Curing time (days)	Packing density	W/C	$B/(T+S)$	Observed UCS (MPa)	Calculated UCS (MPa)	Error (%)
1	0.28	7	0.703	2.450	0.167	1.676	1.759	−4.94
2	0.25	7	0.689	2.250	0.125	2.235	2.249	−0.60
3	0.15	7	0.654	3.463	0.100	0.763	0.727	4.66
4	0.28	14	0.703	2.450	0.167	2.289	2.385	−4.21
5	0.25	14	0.689	2.250	0.125	3.009	3.049	−1.34
6	0.15	14	0.654	3.463	0.100	1.021	0.987	3.37
7	0.28	28	0.703	2.450	0.167	2.959	3.012	−1.78
8	0.25	28	0.689	2.250	0.125	3.901	3.850	1.30
9	0.15	28	0.654	3.463	0.100	1.309	1.246	4.83

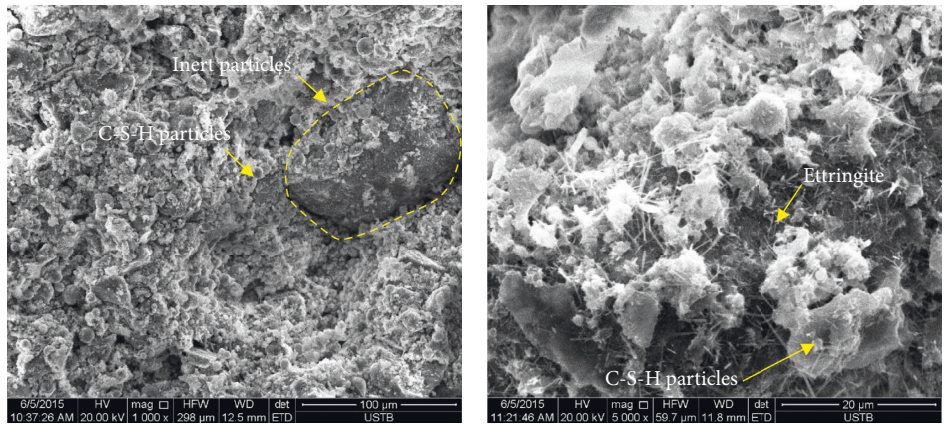

(a) (b)

Figure 8: Microstructural images of waste-unclassified tailings paste. (a) Microcosmic image 1000x. (b) Microcosmic image 5000x.

Meanwhile, the relationship between the influence factors and the strength is basically explained, where the strength presents a positive power exponential function with and packing density Φ, which represents the contents of tailings and waste rock, while a negative exponential relationship with the water-cement ratio W/C and cement-tailings ratio C/A, and a typical logarithmic relationship with the curing days D, and a linear relationship with the cement proportion B. This paper also tested the applicability of this model to some other different materials by sampling from several different mines. Model parameters are obtained based on limited experiments, and the strength range of 3–28 days can be predicted accurately. The development rule of paste strength using complex materials still needs further verification. When applied in specific mines, the model parameters can be adjusted through several sets of additional experiments.

4.3. Examination of the New Developed Model. The unclassified tailings and waste materials were derived from a copper mine in Xinjiang, China, where the density of the unclassified tailings is 2.662 t/m^3, and the dense packing density is 0.603. The contents of −74 μm particles, −45 μm particles, and −20 μm fine particles in the unclassified tailings account for 64.32%, 43.1%, and 29.8%, respectively. The value of C_U ($C_U = d_{60}/d_{10}$) is 18.36, and C_C ($C_C = d_{30}^2/(d_{10} \times d_{60})$) is 1.62, from which it can be indicated that the unclassified tailings cover a wide range of particle size distribution and have a good continuous condition. The waste rocks were sampled and then broken into particles of about −10 mm before being transported to the laboratory. The rock density is 2.663 t/m^3 and the packing density is 0.699. The contents of −1 mm particles, −3 mm particles, and −5 mm particles account for 28.82%, 48.6%, and 74.09%, respectively. The value of C_U of waste rock is 17.05 and C_C is 1.47, showing a wide range of waste particle size distribution and a proper gradation. In order to verify the overall reliability of the strength prediction model, three groups of material proportions were designed for the verification of the predicted strength of 7 days, 14 days, and 28 days. The experimental and calculated results are shown in Table 4. In this table, it can be seen that the strength model is widely applied for predicting the strength of paste prepared from materials of different characteristics, with forecast errors being basically controlled within 5%.

4.4. Strength Formation Mechanism of Paste. A large number of C-S-H gels and CH crystals have been found in the microstructure through environmental scanning electron microscopy (ESEM), which covered the surface of inert particles such as tailings and waste rocks, as shown in Figure 8(a). It is observed that there is a large amount of fine fibrous ettringite between C-S-H gel particles and inert particles, as shown in

Figure 8(b), which made the connecting structure stronger. At the same time, ettringite [40, 41] can increase the solid volume of paste by more than 1.2 times, which can fill the void structure and increase the strength effectively.

5. Conclusions

This paper analyzed the properties of the unclassified tailings-waste paste materials and the influential factors of strength. Through the analysis on the existed strength models, combined with the experimental results, a prediction model of strength of waste rock-unclassified tailings was proposed. The applicability of the model was verified. The main results of the research are as follows:

(1) The strength value can increase by 4.7%~16.5% with 1% growth of concentration. At the same time, with a higher concentration, the effect of cement on the strength will be reduced to some extent. The relationship between strength and the water-cement ratio is negative exponent. The *UCS* and cement-tailings ratio also shows an exponential relationship.

(2) The growth of strength is nonlinear with the tailings-waste ratio but has a stable growth relationship with packing density. The power function of strength and density is obtained by single factor regression analysis. Through the analysis on the relationship between strength and curing time, it can be seen that the relationship between the strength and curing time is logarithmic.

(3) A strength prediction model of waste-unclassified tailings paste is proposed. Through validation, the predicted results of the model are stable, with high reliability. The error range is basically controlled within 5%.

Data Availability

All data, models, and code generated or used during the study appear in the submitted article.

Conflicts of Interest

The authors declare that they have no conflicts of interest.

Acknowledgments

This work was financially supported by the National Natural Science Foundation of China (Nos. 51934003 and 51774020), the National key Research and Development Plan (2017YFC0805300), the Key Laboratory of Ministry of Education of China for Efficient Mining and Safety of Metal Mines (No. ustbmslab201801), Program for Innovative Research Team (in Science and Technology) in University of Yunnan Province, and the Natural Science Research Fund of Kunming University of Science and Technology (KKSY201821024). The authors gratefully acknowledge the financial support of the above items.

References

[1] W. U. Ai-Xiang, Y. Yang, H. Y. Cheng, S. M. Chen, and Y. Han, "Status and prospects of paste technology in China," *Chinese Journal of Engineering*, vol. 40, no. 5, pp. 517–525, 2018.

[2] E. Yilmaz, T. Belem, B. Bussière, and M. Benzaazoua, "Relationships between microstructural properties and compressive strength of consolidated and unconsolidated cemented paste backfills," *Cement and Concrete Composites*, vol. 33, no. 6, pp. 702–715, 2011.

[3] Z.-X. Liu, M. Lan, S.-Y. Xiao, and H.-Q. Guo, "Damage failure of cemented backfill and its reasonable match with rock mass," *Transactions of Nonferrous Metals Society of China*, vol. 25, no. 3, pp. 954–959, 2015.

[4] I. Mehdipour and K. H. Khayat, "Effect of particle-size distribution and specific surface area of different binder systems on packing density and flow characteristics of cement paste," *Cement and Concrete Composites*, vol. 78, pp. 120–131, 2017.

[5] Y. Li and J. Li, "Relationship between fracture area and tensile strength of cement paste with supplementary cementitious materials," *Construction and Building Materials*, vol. 79, pp. 223–228, 2015.

[6] X. Ke, X. Zhou, X. Wang, T. Wang, H. Hou, and M. Zhou, "Effect of tailings fineness on the pore structure development of cemented paste backfill," *Construction and Building Materials*, vol. 126, pp. 345–350, 2016.

[7] H. Ma, B. Xu, J. Liu, H. Pei, and Z. Li, "Effects of water content, magnesia-to-phosphate molar ratio and age on pore structure, strength and permeability of magnesium potassium phosphate cement paste," *Materials & Design*, vol. 64, pp. 497–502, 2014.

[8] M. Fall and M. Benzaazoua, "Modeling the effect of sulphate on strength development of paste backfill and binder mixture optimization," *Cement and Concrete Research*, vol. 35, no. 2, pp. 301–314, 2005.

[9] M. Fall, M. Benzaazoua, and S. Ouellet, "Experimental characterization of the influence of tailings fineness and density on the quality of cemented paste backfill," *Minerals Engineering*, vol. 18, no. 1, pp. 41–44, 2005.

[10] S. Bahafid, S. Ghabezloo, P. Faure, M. Duc, and J. Sulem, "Effect of the hydration temperature on the pore structure of cement paste: experimental investigation and micromechanical modelling," *Cement and Concrete Research*, vol. 111, pp. 1–14, 2018.

[11] C. Qi and A. Fourie, "Cemented paste backfill for mineral tailings management: review and future perspectives," *Minerals Engineering*, vol. 144, p. 106025, 2019.

[12] C. Qi, A. Fourie, Q. Chen, and Q. Zhang, "A strength prediction model using artificial intelligence for recycling waste tailings as cemented paste backfill," *Journal of Cleaner Production*, vol. 183, pp. 566–578, 2018.

[13] C. Qi, X. Tang, X. Dong, Q. Chen, A. Fourie, and E. Liu, "Towards intelligent mining for Backfill: a genetic programming-based method for strength forecasting of cemented paste backfill," *Minerals Engineering*, vol. 133, pp. 69–79, 2019.

[14] C. Qi, A. Fourie, and Q. Chen, "Neural network and particle swarm optimization for predicting the unconfined compressive strength of cemented paste backfill," *Construction and Building Materials*, vol. 159, pp. 473–478, 2018.

[15] C. Qi, Q. Chen, A. Fourie, and Q. Zhang, "An intelligent modelling framework for mechanical properties of cemented paste backfill," *Minerals Engineering*, vol. 123, pp. 16–27, 2018.

[16] L. Orejarena and M. Fall, "Artificial neural network based modeling of the coupled effect of sulphate and temperature on the strength of cemented paste backfill," *Canadian Journal of Civil Engineering*, vol. 38, no. 1, pp. 100–109, 2011.

[17] L. Orejarena and M. Fall, "The use of artificial neural networks to predict the effect of sulphate attack on the strength of cemented paste backfill," *Bulletin of Engineering Geology and the Environment*, vol. 69, no. 4, pp. 659–670, 2010.

[18] X. Lu, W. Zhou, X. Ding, X. Shi, B. Luan, and M. Li, "Ensemble learning regression for estimating unconfined compressive strength of cemented paste backfill," *IEEE Access*, vol. 7, pp. 72125–72133, 2019.

[19] D. Wu, S.-J. Cai, and G. Huang, "Coupled effect of cement hydration and temperature on rheological properties of fresh cemented tailings backfill slurry," *Transactions of Nonferrous Metals Society of China*, vol. 24, no. 9, pp. 2954–2963, 2014.

[20] W. Piasta and B. Zarzycki, "The effect of cement paste volume and w/c ratio on shrinkage strain, water absorption and compressive strength of high performance concrete," *Construction and Building Materials*, vol. 140, pp. 395–402, 2017.

[21] T. Belem and M. Benzaazoua, "Design and application of underground mine paste backfill technology," *Geotechnical and Geological Engineering*, vol. 26, no. 2, p. 175, 2008.

[22] A. M. Rashad and S. R. Zeedan, "The effect of activator concentration on the residual strength of alkali-activated fly ash pastes subjected to thermal load," *Construction and Building Materials*, vol. 25, no. 7, pp. 3098–3107, 2011.

[23] X. Li, S. J. Wang, T. Y. Liu, and F. S. Ma, "Engineering geology, ground surface movement and fissures induced by underground mining in the Jinchuan Nickel Mine," *Engineering Geology*, vol. 76, no. 1-2, pp. 93–107, 2004.

[24] M.-H. Zhang, K. Sisomphon, T. S. Ng, and D. J. Sun, "Effect of superplasticizers on workability retention and initial setting time of cement pastes," *Construction and Building Materials*, vol. 24, no. 9, pp. 1700–1707, 2010.

[25] W. Sun, H. Wang, and K. Hou, "Control of waste rock-tailings paste backfill for active mining subsidence areas," *Journal of Cleaner Production*, vol. 171, pp. 567–579, 2018.

[26] D. Wu, M. Fall, and S. J. Cai, "Coupling temperature, cement hydration and rheological behaviour of fresh cemented paste backfill," *Minerals Engineering*, vol. 42, pp. 76–87, 2013.

[27] Y. He, Q. S. Chen, C. C. Qi, Q. L. Zhang, and C. C. Xiao, "Lithium slag and fly ash-based binder for cemented fine tailings backfill," *Journal of Environmental Management*, vol. 248, Article ID 109282, 2019.

[28] L. G. Li, C. J. Lin, G. M. Chen, A. K. H. Kwan, and T. Jiang, "Effects of packing on compressive behaviour of recycled aggregate concrete," *Construction and Building Materials*, vol. 157, pp. 757–777, 2017.

[29] M. Nili and A. Ehsani, "Investigating the effect of the cement paste and transition zone on strength development of concrete containing nanosilica and silica fume," *Materials & Design*, vol. 75, pp. 174–183, 2015.

[30] J. J. Chen and A. K. H. Kwan, "Superfine cement for improving packing density, rheology and strength of cement paste," *Cement and Concrete Composites*, vol. 34, no. 1, pp. 1–10, 2012.

[31] I. Fischer, B. Pichler, E. Lach, C. Terner, E. Barraud, and F. Britz, "Compressive strength of cement paste as a function of loading rate: experiments and engineering mechanics analysis," *Cement and Concrete Research*, vol. 58, pp. 186–200, 2014.

[32] E. Yilmaz, T. Belem, and M. Benzaazoua, "Specimen size effect on strength behavior of cemented paste backfills subjected to different placement conditions," *Engineering Geology*, vol. 185, pp. 52–62, 2015.

[33] B. Kondraivendhan and B. Bhattacharjee, "Strength and w/c ratio relationship of cement based materials through pore features," *Materials Characterization*, vol. 122, pp. 124–129, 2016.

[34] W. P. Gonçalves, V. J. Silva, R. R. Menezes, G. A. Neves, H. L. Lira, and L. N. L. Santana, "Microstructural, physical and mechanical behavior of pastes containing clays and alumina waste," *Applied Clay Science*, vol. 137, pp. 259–265, 2017.

[35] A. Wu, Y. Wang, H. Wang, S. Yin, and X. Miao, "Coupled effects of cement type and water quality on the properties of cemented paste backfill," *International Journal of Mineral Processing*, vol. 143, pp. 65–71, 2015.

[36] Q.-S. Chen, Q.-L. Zhang, A. Fourie, X. Chen, and C.-C. Qi, "Experimental investigation on the strength characteristics of cement paste backfill in a similar stope model and its mechanism," *Construction and Building Materials*, vol. 154, pp. 34–43, 2017.

[37] V. Nežerka, V. Hrbek, Z. Prošek, M. Somr, P. Tesárek, and J. Fládr, "Micromechanical characterization and modeling of cement pastes containing waste marble powder," *Journal of Cleaner Production*, vol. 195, pp. 1081–1090, 2018.

[38] X. X. Zhang and D. P. Qiao, "Simulation and experiment of pipeline transportation of high density filling slurry with coarse aggregates," *Chinese Journal of Nonferrous Metals*, vol. 25, no. 1, pp. 258–267, 2015.

[39] A. Kesimal, E. Yilmaz, B. Ercikdi, I. Alp, and H. Deveci, "Effect of properties of tailings and binder on the short-and long-term strength and stability of cemented paste backfill," *Materials Letters*, vol. 59, no. 28, pp. 3703–3709, 2005.

[40] T. Tho-in, V. Sata, K. Boonserm, and P. Chindaprasirt, Compressive strength and microstructure analysis of geopolymer paste using waste glass powder and fly ash," *Journal of Cleaner Production*, vol. 172, pp. 2892–2898, 2018.

[41] H. Cheng, S. Wu, H. Li, and X. Zhang, Influence of time and temperature on rheology and flow performance of cemented paste backfill," *Construction and Building Materials*, vol. 231, Article ID 117117, In press.